# Anisotropic Films for Optical Applications Based on Liquid Crystal and Nanorods

Anisotrope dunne lagen
gebaseerd op vloeibare kristallen en nanorods voor optische toepassingen

Mohammad Mohammadimasoudi

Promotoren: prof. dr. ir. K. Neyts, prof. dr. ir. J. Beeckman
Proefschrift ingediend tot het behalen van de graad van
Doctor in de Ingenieurswetenschappen: Elektrotechniek

Vakgroep Elektronica en Informatiesystemen
Voorzitter: prof. dr. ir. R. Van de Walle
Faculteit Ingenieurswetenschappen en Architectuur
Academiejaar 2015 - 2016

UNIVERSITEIT
GENT

ISBN 978-90-8578-829-4
NUR 959, 924
Wettelijk depot: D/2015/10.500/73

Universiteit Gent
Faculteit Ingenieurswetenschappen en Architectuur
Vakgroep Elektronica en Informatiesystemen (ELIS)

Promotors:

| | |
|---|---|
| Prof. Kristiaan Neyts | Ghent University, Department of Electronics and Information Systems (ELIS) |
| Prof. Jeroen Beeckman | Ghent University, ELIS |

Other Members of the Examination Committee:

| | |
|---|---|
| Prof. Rik Van de Walle (Chairman) | Ghent University, ELIS |
| Prof. Patrick De Visschere | Ghent University, ELIS |
| Prof. Stephen Morris | University of Oxford, Department of Engineering Science |
| Prof. Ezeddin Mohajerani | Shahid Beheshti University, Laser and Plasma Research Institute |
| Prof. Zeger Hens | Ghent University, Department of Inorganic and Physical Chemistry |
| Prof. Dirk Poelman | Ghent University, Department of Solid-state Physics |

Universiteit Gent
Faculteit Ingenieurswetenschappen en Architectuur
Vakgroep Elektronica en Informatiesystemen (ELIS)
Sint-Pietersnieuwstraat 41, B-9000 Gent, België
T: (+32) (0)9 264 3366
F: (+32) (0)9 264 3594

This work was realised in the framework of the IAP, FWO project and SECONDOS

بسم الله الرحمن الرحیم


تقدیم به یك نگاهت

شاید که از در لطف

مهمان خوانده باشم

To the World's Best Father

# MAHDI

# Acknowledgements

بسم الله الرحمن الرحیم

الحمد لله رب العالمین و صلی الله علی سیدنا محمد و آله الطیبین الطاهرین سیما بقیه الله فی الارضین مولانا صاحب الزمان عج الله تعالی فرجه الشریف

الهی کفی بی عزاً اَنْ اَکونَ لَکَ عَبْداً و کفی بی فخراً اَنْ تَکون لی ربّاً

Whomever does not thank the creatures, has not thanked the creator.

This book contains the results of several years of work which I consider ready for publication. For me a PhD degree is important, since it may allow me to keep doing in the future what I have learned.

First of all, I truly thank God for the many blessings and guidance throughout my life especially during these 5 years of the PhD during which I was far from my hometown and family. God provided everything here for me such as promotors, friends and colleagues.

I have benefited immensely during the past few years of my PhD from set of friends, colleagues and promotors and I would like to describe those who I sincerely wish to acknowledge and thank.

I am deeply indebted to my parents. Their prayers, guidance, patience, relentless and unconditional love, compassion, support and encouragements allowed me to reach where I am today. Although impossible to express by words as it deserves, I would like to mention my deepest gratitude to them and I hope to be a reason of pride for them.

I would like to express my special appreciation and thanks to my supervisor, professor Kristiaan Neyts, he has been a tremendous mentor for me. I would like to thank him for encouraging my research and for guiding me to grow as a research scientist. I appreciate his humanity and morality as well as his ability to guide and teach students which is a nice model for my future work. It is truly a great privilege for me to be a student under his supervision.

I also would like to thank my co-supervisor professor Jeroen Beeckman for his support always with smile and patience. I really felt free with him due to his humility and I am very thankful how graciously he responded to me, how he is always willing to discuss ideas of mine (with great patience) no matter how silly it turned out to be. I hope keep my collaboration with Kristiaan and Jeroen in future.

I would also like to thank my committee members, prof. Patrick De Visschere, prof. Stephen Morris, prof. Dirk Poelman, prof. Ezeddin Mohajerani, Prof. Zeger Hens and prof. Rik Van de Walle (chairman of the committee and dean of the Faculty of Engineering and Architecture) for serving as my committee members even at hardship.

I would especially like to thank professor Zeger Hens and Dr. Tangi Aubert from the 'Physics and Chemistry of Nanostructures' group at the department of Inorganic and Physical Chemistry of Ghent University. They provided nanorod materials for me and helped me to understand what are the nanorods and quantum dots, especially during the nano- and bio photonics summer school. I can not forget serious discussion with Zeger about nanorod's results and I am happy that I learned a lot from him.

I have also been surrounded by good colleagues in the office. People of the physical electronics group, I really enjoy working with them. The group of professors provided continuity in an atmosphere that I found very stimulating, Patrick De Visschere, Alex De Vos, Marc Burgelman, Filip Beunis. Also I should mention Dr. Filip Strubbe who helped me for image processing, Dr. Wouter Woestenborghs for technical help, Dr. Lieven Penninck and Dr. Samira Khalifi for scientific discussions. Special thanks for lithography-people: Toon, Oliver and Stijn which provided a lot of samples for my works. I had a nice atmosphere with my office mates: John, Inge, Michiel, Tigran, Frederique, Serena and Joanne. I learned a lot from them. The summary part in this thesis is translated from English to Dutch by the help of Michiel. I should thank Glenn for providing Labview programs for my measurements. I would like to thank other friends in our group that helped me during my PhD career: Caspar, Aimi, Manoj, Oksana, Varsenik, Pavlo, Tomas and Masoumeh. Lastly I want to thank our secretaries Rita, Karen, Marnix and Jeroen O. I thank all of them and never forget them and hope to keep in touch with them as a friend.

I have also been blessed with great support from outside the university. I wish to express my deepest gratitude to the Ahlebaiyt foundation, Amiralmomenin foundation and union of Islamic student association for

being a second family for me. My special thanks to my fellow brothers and sisters and their family: Haj Ali Esmaielpour, Amir Fardis, Sasan, Seyed Mohsen Yazdanparast, Prof. Soleimani, Prof. Aghajan, Prof. Amir jahanshahi, Prof. Aliakbarian, Dr. Chavoshi, Dr. Reza Azarinia, Dr. Mosallanejad, Dr. Mahdikhanloo, Dr. Farrokhzad, Mahdi Hatami, Alireza Bagheri, Ali Diba, Dr. Enayati, Mohammad Mosallanejad, Dr. Bahari, Agha Ebrahim, Agha Reza, Hasan Agha, Agha Soleimani, Dr. Divsalar, Dr. Shamsi, Ihsan Izadi, Ihsan Ansari, Meisam, Hojjat, Mahdi Fathi, Amir tamaddon and Ihsan Darestani.

Also I would like to thank Prof. Amooabedini and Prof. Koohsorkhi from Tehran University for helping me during my PhD.

A special thanks to my family. Words cannot express how grateful I am to my mother-in law, father-in-law, my sisters and brother for all of the sacrifices that you've made on my behalf. Your prayer for me was what sustained me thus far.

Last but not least I specially thank my wife for her love, tolerance and understanding towards me. She always did, and does her best to provide an enjoyable calm environment. I can not forget to mention being the proud father of Zeinab and the new born baby (Narges).

BEDANKT

Mohammad, 25 September 2015

---

“Knowledge is better than wealth. Knowledge guards you, while you have to guard the wealth. Wealth decreases by spending, while knowledge multiplies by spending, and the results of wealth die as wealth decays.”

Ali ibn Abitaleb

---

# Table of contents

# Summary

Photonics is the name for the science that investigates all aspects of light. Light and technologies based on light are very important in our daily life: lighting, displays, solar panels, etc. But also a lot of less obvious technologies are based on light. A good example are the long distance telecommunication systems which are based on optical fiber communication. Nowadays photonics is becoming more and more important. In the European research plan, Horizon 2020, photonics is one of seven important technologies (Key Enabling Technologies) on which research efforts are focused. In a push to reduce global energy consumption, it is necessary to reduce the energy needed for optical devices. In addition, there are other important issues for optical devices such as fabrication cost and miniaturization. With this point of view, in this PhD work various optical devices based on liquid crystal (LC) and nanorods (NR) are investigated and fabricated.

Nowadays, liquid crystals (LCs) are extensively used in electronic displays. Liquid crystal displays (LCDs) have been widely used in cell phones, car navigations, laptop computers, desktop monitors, projectors and TVs. Due to their unique optical properties LCs may play an important role in photonic applications such as tunable filters, tunable laser cavities, tunable focus lenses, spatial light modulators, and diffraction gratings for various applications such as laser beam steering, adaptive optics, lasers and optical communications. In addition, LC as an organic material is promising due to versatility in molecular design: relative ease of synthesis, characterization and processing.

LC molecules are available in various types and phases. In this dissertation, nematic and chiral nematic LC (CLC) are both used. Another important classification for the LC materials used in this thesis is whether the LC molecules are reactive or non-reactive.

CLCs spontaneously arrange into a helical structure with periodicity of a few hundred nanometer up to several tens of micrometers. The periodic alignment also results in a modulation of the refractive index profile. CLCs have been widely used in bistable displays, flexible displays, reflectors etc.

On the other hand, reactive liquid crystals are a unique class of materials that provide the possibility to 'freeze' the liquid crystal orientation. When the materials are illuminated with UV light (and using an appropriate photoinitiator) they chemically react and polymerize. The polymerizable functional groups in the molecular structure offer the possibility for crosslinking and forming a long chain network while maintaining the order. Recently the tendency towards miniaturization and portability in emerging LC-based applications brings forward new research interests in reactive LC. An interesting feature is that the polymeric films can be delaminated from the glass substrate so that they become free standing polymer films with sufficient mechanical strength and elastic flexibility.

In this dissertation, fabrication of thin film polarizers and color filters based on photo-polymerization of reactive LC is demonstrated. The thin film polarizer is fabricated for applications which require very small thicknesses of the final device such as electro-active contact lenses. The thin film dye-doped polarizer has a broad absorption band between 400 nm and 650 nm and has a contrast ratio of 9 for a film of only 12 μm. On the other hand I also developed a technique to make a mono domain CLC thin film color filter. The photonic band gap of the color filter is around 80 nm with high reflectivity. Both thin films can be detached from the substrate. These films have thermal stability and chemical resistivity and are suitable to be processed in optical device manufacturing as additional films or as in-cell optical components.

The third fabricated device in this work is a widely tunable optical filter with microsecond switching time. A wavelength shift of the photonic band gap of 141 nm is obtained by electric switching of a Partly Polymerized Chiral Liquid Crystal (PPCLC). The devices feature high reflectivity in the photonic band gap without any noticeable degradation or disruption when applying voltages. They exhibit response times of 50 μs and 20 μs for switching on and off. The device consists of a mixture of photo-polymerizable liquid crystal, non-reactive nematic liquid crystal and a chiral dopant that has been polymerized with UV light. I investigate the influence of the amplitude of the applied voltage on the width and the depth of the reflection band. In addition, the influence of UV illumination on a partially polymerized chiral liquid crystal is investigated. A blue-wavelength shift of

the photonic band gap is obtained as a function of power, duration time of UV illumination and the thickness of the cells. Interestingly the width and the depth of the photonic band gap are unaffected by the change in UV curing conditions, which indicates that there is no degradation by the UV light.

A microsecond-range optical shutter for unpolarized light is demonstrated as a forth application using reactive LCs. The device works independently of the polarization state of the incoming light beam. Modulation between 3% transmission and 60% transmission is obtained within a wavelength range of 50 nm with a response time of 20 µs. The device consists of two PPCLC layers separated by a half wave plate. The shutter features high reflectivity in the photonic band gap. I investigate the influence of the amplitude of the applied voltage on the width and the depth of the reflection band.

Another interesting material system that I focus on for optical applications is based on nanorods. Semiconductor NRs have anisotropic light absorption and light emission properties. When these NRs can be collectively aligned, they may be applied in polarized emitters, polarized fluorescent sheets or polarization-selective detectors. In this dissertation, I demonstrate full alignment of colloidal NRs in suspension by an electric field. By comparing optical transmission measurements with theoretical simulations, the permanent and induced dipole moments of the NRs are determined. The correlation between theory and experiment indicates that the orientation is driven by the permanent dipole moment of the NRs. The required electric field, the values of the permanent dipole moment, relaxation time, absorption anisotropy and critical frequency of the CdSe/CdS dots in rods are determined. In addition, I experimentally verify the anisotropic absorption of the CdSe NR core for a wavelength of 560 nm.

The homogeneous deposition of aligned NRs on large substrates is interesting for large area applications such as solar cells and OLEDs. Moreover, semiconductor nanoparticles can be used to efficiently transform blue light from GaN-based LEDs into for example green and red light, which is needed for colour displays. The combination of blue, green and red light is desired for backlights in liquid crystal displays. As liquid crystal devices modulate the transmission of polarized light, it would be an advantage to start from a backlight that is able to emit polarized green and red light. In the rest of the dissertation, I present four methods for the homogeneous deposition and alignment of NRs from a colloidal suspension. The accumulation, orientation and polarized fluorescence of the NRs is verified

by AFM and polarized fluorescence microscopy. The 4 methods investigated in this work for aligning NRs from a solution into solid material are:

1- Dip coating and evaporation in the presence of an electric field
2- UV curable monomer in the presence of an applied electric field
3- Reactive LC in the presence of an applied electric field.
4- Electro spinning of aligned NRs in fiber.

# Samenvatting

Fotonica is de naam die gegeven is aan de studie van licht. Licht en op licht gebaseerde technologieën zijn uitermate belangrijk in ons dagelijks leven. Denk maar aan verlichting, beeldschermen, zonnecellen en zoveel meer. Een goed voorbeeld is langeafstandscommunicatie door middel van optische glasvezelcommunicatie. Vandaag de dag wordt fotonica steeds belangrijker. In het Europees onderzoeksplan, Horizon 2020, is fotonica één van de zeven sleuteltechnologieën (Key Enabling Technologies) waarop onderzoeksinspanningen gefocust worden. In een poging om het wereldwijde energieverbruik te verminderen is het noodzakelijk dat ook de optische technologieën energie-efficiënter worden. Daarenboven zijn er nog andere belangrijke kwesties, zoals de constante miniaturisatie van optische componenten. In dit proefschrift kijk ik naar de fabricage en karakterisatie van een aantal optische componenten die gebaseerd zijn op vloeibare kristallen en nanorods. Momenteel worden vloeibare kristallen in veel toepassingen gebruikt. Men kan ze vinden in LCD beeldschermen, in mobiele telefoons, projectoren, GPS navigatie, laptops, computerschermen en TVs. Door hun unieke eigenschappen spelen ze een belangrijke rol in fotonische elementen zoals afstembare filters, afstembare lasercaviteiten, afstembare lenzen, ruimtelijke fasemodulatoren en diffractieve roosters voor een waaier aan componenten zoals het sturen van licht, afstembare optische componenten, lasers en optische communicatie. Vloeibare kristallen zijn, doordat ze organisch zijn, eenvoudig te synthetiseren. Vloeibaar-kristalmoleculen zijn verkrijgbaar in verschillende variëteiten en fasen. In dit proefschrift worden zowel nematische als chirale nematische vloeibare kristallen gebruikt. Een andere manier van classificatie is het al dan niet reactief zijn van de vloeibare kristallen. Chirale vloeibare kristallen ordenen zich spontaan in een helix-structuur met een periodiciteit in de orde van 0.1 tot 10 micrometer. De periodieke ordening resulteert ook in een modulatie van het brekingsindexprofiel. Cholesterische vloeibare kristallen worden reeds vaak gebruikt in bi-stabiele displays, flexibele displays, reflectoren, enz. Reactieve vloeibare kristallen zijn een klasse van materialen die de

mogelijkheid bieden om de vloeibaar-kristaloriëntatie te ‘bevriezen’. Wanneer deze materialen belicht worden met UV licht gebeurt er een chemische reactie die leidt tot polymerisatie. Polymeriseerbare functionele groepen in de moleculaire structuur bieden de mogelijkheid voor crosslinking en vorming van een kettingnetwerk met behoud van de ordening. De recente trend naar miniaturisatie en draagbaarheid in vloeibaar-kristaltoepassingen wakkerde de interesse in deze reactieve vloeibare kristallen aan. Een uiterst interessante eigenschap van de gepolymeriseerde lagen is dat ze gedelamineerd kunnen van hun draagvlak en zo een vrijstaande polymeerlaag kunnen vormen met voldoende mechanische sterkte en flexibiliteit.

In dit proefschrift wordt de fabricage van dunne polarisatoren en kleurenfilters met behulp van foto-polymerisatie van reactieve vloeibare kristallen gedemonstreerd. De polarisator werd gefabriceerd voor toepassingen met een beperkte totale dikte, zoals bijvoorbeeld een elektro-actieve contactlens. De dunne polarisator heeft een brede absorptieband tussen 400 nm en 650 nm en heeft een contrastverhouding van 9 voor een film van slechts 12 µm. Ik ontwikkelde een techniek voor de fabricage van een mono-domein cholesterisch vloeibaar-kristalkleurfilter. De fotonische bandkloof voor dit kleurfilter is 80 nm breed en het filter heeft een hoge reflectiviteit. Beide lagen kunnen losgemaakt worden van het substraat. Deze films zijn thermisch stabiel en chemisch resistief en zijn zodoende toepasbaar voor integratie in optische componenten of voor integratie in optische componenten.

Een derde component die gefabriceerd werd is een optisch filter die moduleerbeer is over een wijd bereik met een schakeltijd in de orde van enkele microseconden.

Een golflengteverschuiving van de fotonische bandkloof van 141 nm werd gerealiseerd door middel van elektrisch schakelen van gedeeltelijk gepolymeriseerde chirale vloeibare kristallen. De componenten vertonen hoge reflectiviteit in de fotonische bandkloof zonder degradatie als gevolg van de aangelegde spanningen. Ze vertonen reactietijden van 50 µs en 20 µs voor aan- en afschakelen. De componenten bestaan uit een mengsel van polymeriseerbare vloeibare kristallen, niet-reactief nematisch vloeibaar kristal en een chirale dopant die gepolymeriseerd worden met UV belichting. Ik onderzoek de invloed van de amplitude van de aangelegd spanning op de breedte en de diepte van de reflectieve band. Ook werd de invloed van de UV belichting op gedeeltelijk gepolymeriseerde chirale vloeibare kristallen onderzocht. Een golflengteverschuiving van de fotonische bandkloof treedt

op in functie van de intensiteit en duur van de belichting en de dikte van de cellen. De UV belichting blijkt geen invloed te hebben op het eindresultaat waardoor ik kan concluderen dat er geen degradatie is door UV belichting.

Een optische sluiter voor ongepolariseerd licht in het microsecondengebeide werd gedemonstreerd als een vierde toepassing van reactieve vloeibare kristallen. De component werkt onafhankelijk van de polarisatie van het binnenkomende licht. Een modulatie tussen 3 % en 60 % transmissie wordt gedemonstreerd binnen een golflengtebereik van 50 nm met een reactietijd van 20 µs. De component bestaat uit twee gedeeltelijk gepolymeriseerde chirale vloeibaar-kristallagen, gescheiden door een halve golflengteplaat. De sluiter vertoont hoge reflectiviteit in de fotonische bandkloof. Ik onderzocht de invloed van de amplitude van het aangelegd veld op de breedte en diepte van de optische bandkloof.

Een ander interessant materiaalsysteem is gebaseerd op nanorods. Halfgeleidernanorods absorberen en emitteren licht op een anisotrope manier. Wanneer deze nanorods collectief gealigneerd worden kunnen ze gebruikt worden als gepolariseerde emitter, gepolariseerd fluorescent vlak of polarisatie-selectieve detector.

In dit proefschrift demonstreer ik de volledige alignering van colloïdale nanorods door middel van een elektrisch veld. Door vergelijking van experimenteel opgemeten transmissie- en absorptiespectra met theoretische simulaties kan ik het permanent en geïnduceerd dipoolmoment van de nanorods achterhalen. De correlatie tussen theorie en experiment leert ons dat de oriëntatie gedreven is door het permanent dipoolmoment van de nanorods. Het nodige elektrisch veld, de waarde van het permanent dipoolmoment, de relaxatietijd, de anisotrope absorptie en de kritische frequentie van de CdSe/CdS dots in rods worden opgemeten. Ik verifieer ook experimenteel de anisotrope absorptie van de CdSe dots in de nanorods voor een golflengte van 560 nm.

De homogene depositie van gealigneerde nanorods op grote substraten is interessant voor toepassingen zoals zonnecellen en OLEDs. Bovendien kunnen halfgeleidernanodeeltjes gebruikt worden voor de conversie van blauw licht van GaN gebaseerde LEDs naar bijvoorbeeld groen en rood licht. De combinatie van blauw, groen en rood licht met een smalle spectrale breedte is nodig voor een goed kleurenbereik van LCD schermen. Doordat vele vloeibaar-kristaltoepassingen enkel gepolariseerd licht moduleren zou het voordelig zijn om te kunnen starten van groen en rood licht dat reeds gepolariseerd is. Op die manier verliest men geen licht in de polarisator. In

de rest van het proefschrift stel ik vier methodes voor die kunnen gebruikt worden voor de depositie en alignering van nanorods, startend van een colloïdale oplossing van nanodeeltjes.

De accumulatie, oriëntatie en gepolariseerde fluorescentie van de nanorods werd geverifieerd met AFM en gepolariseerde fluorescentiemicroscopie. De vier methodes, gebruikt voor alignering van nanorods vanuit een colloidale suspensie zijn:

1. Dip-coating in de aanwezigheid van een elektrisch veld
2. Het gebruik van een UV-hardend monomeer in de aanwezigheid van een elektrisch veld
3. Het gebruik van reactieve vloeibare kristallen in de aanwezigheid van een elektrisch veld
4. Electro-spinnen van gealigneerde nanorods in vezels.

# List of Figures

# List of tables

# List of symbols

| Symbols | description | Units |
|---|---|---|
| $A$ | Absorbance | - |
| $a$ | Long semi-axis of the prolate ellipsoid | m |
| $b$ | Short semi-axis of the prolate ellipsoid | m |
| $c$ | Short semi-axis of the prolate ellipsoid | m |
| $\boldsymbol{c}$ | Optical axis of a uniaxial medium | - |
| $a'$, $b'$ | semi-axes of the prolate ellipsoid NR, which include the length of the ligands | m |
| $\alpha$ | polarizability | $m^3$ |
| $d$ | Thickness | m |
| $\Delta\boldsymbol{p}$ | Induced dipole moment | Debye |
| $E_{ext}$ | External electric field | V/m |
| $E_g$ | Band gap energy | eV |
| $\varepsilon_h$ | Dielectric constant of host | F/m |
| $\varepsilon_0$ | Dielectric constant of vacuum | F/m |
| $\varepsilon_{NR}$ | Dielectric constant of nanorod | F/m |
| $\eta$ | dynamic viscosity of the medium | Pa.s |
| $f$ | fraction | - |
| $f$ | Frequency | Hz |
| $\boldsymbol{\varphi}$ | Azimuth angle of the nanorod | rad |
| $\gamma_r$ | rotational viscosity | g/cm·s |
| $I$ | Imaginary part of complex number | - |
| $k_B$ | Boltzmann constant | $8.617*10^5$eV/K |

| | | |
|---|---|---|
| $\mathbf{k}$ | Wave vector of a plane wave | $m^{-1}$ |
| $\chi$ | ellipticity angle | rad |
| $\measuredangle$ | Director of liquid crystal | - |
| $L$ | Depolarization factor | - |
| $\mu$ | Absorption coefficients | $cm^{-1}$ |
| $\mathbf{1}_a$ | Unit vector along the long axis of the prolate ellipsoid | - |
| $\mathbf{1}_b$ | Unit vector perpendicular to both $\mathbf{1}_a$ and $\mathbf{1}_c$ | - |
| $\mathbf{1}_c$ | Unit vector perpendicular to both $\mathbf{1}_a$ and the external field | - |
| $\lambda$ | Wavelength | nm |
| $n_o$ | Ordinary refractive index | - |
| $n_e$ | Extra ordinary refractive index | - |
| $\Delta n$ | Birefringence | - |
| $\boldsymbol{p}$ | Permanent dipole moment | Debye |
| $\boldsymbol{P}$ | Pitch | nm |
| $\wp$ | Degree of polarization | - |
| $\parallel$ | Parallel | - |
| $\perp$ | Perpendicular | - |
| $R$ | Real part of complex number | - |
| $S$ | Stokes parameter | - |
| $\mathcal{S}$ | Order parameter | - |
| $t$ | Time | s |
| $\tau_{relaxation}$ | Rotational relaxation time | s |
| $T$ | Torque | N.m |
| $\boldsymbol{\theta}$ | inclination angle of the nanorod | ° |
| $U_{el}$ | Electrostatic energy | Joule |
| $V$ | Voltage | V |
| $\Pi$ | Polarization ratio | - |

# List of abbreviations

| Abbreviations | Description |
|---|---|
| AC | Alternating Current |
| CdS | Cadmium Sulfide |
| CdSe | Cadmium Selenide |
| CLC | Chiral nematic Liquid Crystal |
| Cv | Coefficient of Variation |
| EHDI | Electro-HydroDynamic Instabilities |
| FLC | ferroelectric liquid crystal |
| ITO | Indium Tin Oxide |
| IR | Infra-Red |
| LC | Liquid Crystal |
| LCD | Liquid Crystal Display |
| LH | Left Handed |
| NC | Nano Crystal |
| NR | Nanorod |
| OLED | Organic Light Emitting Diode |
| PBG | Photonic Band Gap |
| PPCLC | Partially Polymerized Chiral nematic Liquid Crystal |
| QD | Quantum dot |
| R | Reflection |
| RH | Right Handed |
| T | Transmission |
| UV | Ultra Violet |

# List of Publications

**Patent**

[1] Mohammad MohammadiMassoudi, Jeroen Beeckman, Jungsoon Shin, Jaehyuk Choi, Kristiaan Neyts, '*Polarization independent optical shutter based on the switching of the transmission bandgap of cholesteric films with liquid crystal nanopores*', US14/687445, April 15th 2015. ( KOREA Patent: 10-2014-0045496, May 2014 )

[2] Mohammad MohammadiMassoudi, Jeroen Beeckman,, Kristiaan Neyts, '*Planar aligned nanorods and liquid crystal assemblies*', May 30th 2015, EP15170004.4

**International Journals (ISI)**

[3] Mohammad MohammadiMassoudi, Jeroen Beeckman, Zeger Hens, Kristiaan Neyts "Anisotropic light emitters based on aligned NRs" Advanced functional materials, (submitted), 2015.

[4] Mohammad MohammadiMassoudi, Zeger Hens, Kristiaan Neyts "Full Alignment of Dispersed Colloidal NRs by Alternating Electric Fields" Nanoscale (submitted), 2015.

[5] Mohammad Mohammadimasoudi, Jeroen Beeckman, Jungsoon Shin, Keechang Lee and Kristiaan Neyts Microsecond-range optical shutter for unpolarized light with chiral nematic liquid crystal, *AIP advances*,**5** 047122, 2015.

[6] Tangi Aubert; Palangetic, Ljiljana; Mohammad MohammadiMassoudi, Kristiaan Neyts Jeroen Beeckman Zeger Hens," Large scale and

electro-switchable polarized emission from semiconductor NRs aligned in polymeric nanofibers", *ACS Photonics*, 2015.

[7] Mohammad Mohammadimasoudi, Jeroen Beeckman, Jungsoon Shin, Keechang Lee and Kristiaan Neyts, 'Widely tunable chiral nematic liquid crystal optical filter with microsecond switching time', *Optics Express*, Vol. **22**(16), pp. 19098-19107, 2014.

[8] Mohammad Mohammadimasoudi, Lieven Penninck, Tangi Aubert, Raquel Filipa Gomes Pinto Fernandes, Zeger Hens, Filip Strubbe and Kristiaan Neyts, 'Fast and versatile deposition of aligned semiconductor NRs by dip-coating on a substrate with interdigitated electrodes', *Optical Materials Express*, Vol. **3**(12), pp. 2045-2054, 2013.

**Conference proceeding which index in web of Science (P1)**

[9] Mohammad MohammadiMassoudi, Jeroen Beeckman, Kristiaan Neyts, "Thin film polariser and color filter based on photo-polymerizable nematic liquid crystal", SPIE conference , February 2015.

[10] Mohammad MohammadiMassoudi, Jeroen Beeckman, Kristiaan Neyts, "Effect of UV curing conditions on polymerized tunable chiral nematic liquid crystals", SPIE conference, August 2014.

[11] Mohammad Mohammadimasoudi, Lieven Penninck, Tangi Aubert, Raquel Filipa Gomes Pinto Fernandes, Zeger Hens, Filip Strubbe and Kristiaan Neyts "Polarized light emission by deposition of aligned semiconductor nano rods", SPIE conference, August 2014.

**International Conferences (C3)**

[12] Mohammad Mohammadimasoudi, Jeroen Beeckman, Kristiaan Neyts,

"Thin film polarized liquid crystal backlight", Euro Display, Gent, 2015.

[13] Mohammad Mohammadimasoudi, Jungsoon Shin, Keechang Lee, Kristiaan Neyts, Jeroen Beeckman, "Polarization independent microsecond electro-optic switch", 18th Annual Workshop of the IEEE Photonics Benelux Chapter, Mons, 2015

[14] Mohammad Mohammadimasoudi, Jeroen Beeckman, Kristiaan Neyts, "Thin and flexible mirrorless laser film with spatially tunable emission", Optics of Liquid Crystals, Sopot, 2015.

[15] Kristiaan Neyts, Yi Xie, Tigran Dadalyan, Inge Nys, Mohammad Mohammadimasoudi, Caspar Schreuer, Krassimir Panajotov, Jeroen Beeckman, " Lasers with nematic and chiral nematic liquid crystal" ,Optics of Liquid Crystals, Sopot, 2015.

[16] Kristiaan Neyts, Yi Xie, Mohammad Mohammadimasoudi, Jeroen Beeckman, "Voltage-tunable liquid-crystal-based filters, resonators, and lasers" SPIE conference, San Francisco, 2015.

[17] Tangi Aubert, Palangetic Ljiljana, Mohammad Mohammadimasoudi, Kristiaan Neyts, Jeroen Beeckman, Zeger Hens, "Large scale and electro-switchable polarized emission from semiconductor nanorods aligned in polymeric nanofibers", Euro Display, Gent, 2015.

[18] Mohammad Mohammadimasoudi, Jeroen Beeckman, Kristiaan Neyts, "Fast widely tunable chiral nematic liquid crystal filter", 25th International Liquid Crystal Conference, Ireland, 2014.

[19] Jeroen Beeckman, Mohammad Mohammadimasoudi, Yi Xie, Kristiaan Neyts "Nematic liquid crystal devices with sub-millisecond response time" SID Mid Europe Meeting, Stuttgart, 2014.

[20] Kristiaan Neyts, Oliver Willekens, Inge Nys, Yi Xie, Mohammad Mohammadimasoudi, Jeroen Beeckman, "Liquid crystal patterns originating from structured alignment" International Conference on Photoalignment and Photopatterning in Soft Materials, Hong Kong, 2014.

[21] Mohammad Mohammadimasoudi, Jeroen Beeckman, Kristiaan Neyts and Lieven Penninck “Polymerized tunable chiral nematic liquid crystals” XX Conference on Liquid Crystals: Chemistry, Physics and Applications, Poland, 2013.

[22] Kristiaan Neyts, Lieven Penninck, Yi Xie, Caspar Schreuer, Mohammad Mohammadimasoudi, Jeroen Beeckman, “Light emission and lasing with anisotropic materials”, XX Conference on Liquid Crystals: Chemistry, Physics and Applications, Poland, 2013.

# Scientific Award

The SID-ME Chapter Student Award for an outstanding scientific or technical achievement in, or contribution to, research on information display. The title of work is **'Thin film polarized liquid crystal backlight'**.

The prize amounts to 1500 euro and the award ceremony is held during the EuroDisplay 2015 conference.

# Chapter 1

# Introduction

In the 21st century, the rate at which new technologies are developed and brought to the market is higher than ever. Many scientists work hard to provide technologies that could bring a better life for the future. In particular, photonics technology is one of seven important technologies for future life according to the Horizon 2020 work program of the European Commission. On the other hand, due to the growing use of different technologies, the consumption of energy also increases. The increasing use of energy and the associated problems such as $CO_2$ emission and climate change is one of the important issues for humanity. In a push to reduce global energy consumption, it is necessary to reduce the energy needed for optical devices as well. In addition, quite a lot other important factors are important when considering future photonic devices: fabrication cost, miniaturization, the use of scarce materials (such as Eu or In), toxicity of materials (e.g. the Cd in today's most successful quantum dots), etc. With these issues in mind, in this work I try to investigate and fabricate various optical devices based on liquid crystal (LC) and nanorods (NR).

## 1.1 Liquid crystals

Liquid crystal is a phase of matter apart from the conventional solid, liquid and gaseous phases. In the LC phase, the constituent molecules have some freedom to move around in the material just like in a liquid. But at the same time, the molecules are subjected to long range ordering in their orientation or position, just as in a solid. The fact that the properties of this phase lies in between solids and liquids has led to the term mesophase. The mix of properties on the microscopic scale leads to very interesting macroscopic properties, combining anisotropy with low viscosity.

The type of mesophase of the liquid crystal is determined by the type of ordering (formation of layers, orientation, etc.). It is strongly influenced by the shape of the molecules. Common shapes of liquid crystal molecules are rod-like, disc-like or banana-shaped. When the appearance of different mesophases is temperature-dependent, it is called a thermotropic liquid crystal. If the molecules arrange themselves in ordered structures in a solvent and if the appearance of the mesophases is concentration dependent, then it is called a lyotropic liquid crystal.

The LC molecules should be chemically stable and not bind with each other. Typically, the building blocks of liquid crystals are organic molecules with a size of a few nm. In thermotropic liquid crystals the interaction between the molecules is in competition with the thermal motion of the molecules. The material becomes an isotropic liquid at a sufficiently high temperature and a crystalline solid at a sufficiently low temperature. The liquid crystal phase was discovered because of the two different transitions (solid - liquid crystal and liquid crystal - liquid) occurring at different temperatures. Friederich Reinitzer noticed in 1888 that cholesteryl benzoate melts at 145°C into a cloudy fluid (the liquid crystal phase) and that a second transition into a clear liquid takes place at 178°C [1]. Nowadays, liquid crystal materials have been extensively used in both display and photonic devices. In our daily life, liquid crystal displays (LCDs) are currently widely used in cell phones, car navigations, laptop computers, desktop monitors, projectors and TVs (Figure 1.1). For photonic applications, due to the unique optical properties, LC plays (or may play) an important role to realize tunable wavelength filters, tunable laser cavities, lenses with tunable focal distance, spatial light modulators and diffraction gratings for various applications such as laser beam steering, adaptive optics and optical communications. In addition, LC as an organic material is promising for photonics because it does not contain

any scarce materials and because of the versatility in molecular design: relative ease of synthesis, characterization and processing.

**Figure 1.1:** Different applications using liquid crystal displays

Depending on the molecular structure of the LC molecules and the composition of the LC mixture, different mesophases can be present. Not all LC materials possess all mesophases. In this work, the focus is on rod-like molecules. Figure 1.2 displays the thermotropic transition of a liquid crystal based on rod-like molecules from solid phase crystal to an isotropic liquid. In between these two extremes, different liquid crystal mesophases can be present. Three of the common mesophases are smectic C, smectic A and nematic. The first two exhibit also spatial ordering of the molecules as the molecules arrange themselves in planes, while the nematic phase only exhibits orientational ordering and no spatial ordering. I will not go into detail about the smectic C and smectic A phase because these phases are not used in this work. In the nematic phase, the formation of layers is lost. The order that still remains is that on average the molecules point into the same direction.

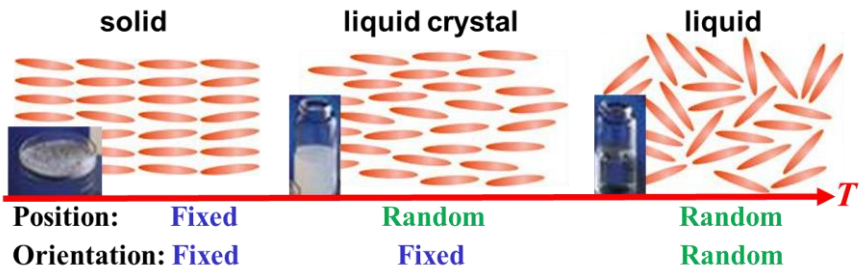


**Figure 1.2**: Schematic presentation of the solid, liquid crystal and liquid phase.

### 1.1.1 Nematic liquid crystal

Nematic LC usually consist of organic molecules with a chain structure, containing one or more aromatic rings. Typically, there is a side chain, two phenyl rings connected by a linkage group and a terminal group on the other side. Figure 1.3 shows 5CB (pentylcyanobiphenyl) as one of the well-known molecules that exhibit a nematic LC phase. 5CB is an example of a single compound that can be used. In practice, all of the nematic liquid crystals used are mixtures of different components. E7 for example is a mixture of 5CB and 7CB, 80CB and 5CT.

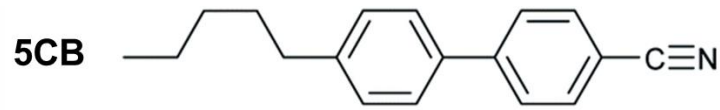


**Figure 1.3:** Chemical structure of 5CB (pentylcyanobiphenyl). An example of an organic molecule with a nematic phase.

The physical properties (dielectric, magnetic, optical and mechanical) of the liquid crystals are determined by the different groups in these molecules. The electronic polarizability is usually large in the plane of the rings and smaller perpendicular to the rings due to the extended electron wave functions in the phenyl ring. Phenyl rings also tend to yield a larger polarizability than saturated rings (with two hydrogen atoms per carbon atom in the ring). Many nematic LCs have a permanent dipole moment *p*, due to groups with different electronegativity.

Nematic LCs can absorb light in the UV or visible range by making a transition from the ground state to some excited state of the electron wave function.

In the isotropic phase, nematic LC molecules move around with random orientation as in a normal liquid and behave like an isotropic medium. There are local interactions between molecules, but there is no ordering on a macroscopic scale. If the temperature is decreased, the interaction between molecules increases in relative importance (compared to the thermal energy) and the local order increases.

Nematic LCs are able to rotate, and switch head and tail. They are often represented by cylinders or prolate ellipsoids as shown in Figure 1.4. The average direction of the long axis is often represented by a vector, the director $\vec{\ell}$ . The nematic LC molecules are free to rotate around their long axis, so the phase has full rotational symmetry. This symmetry is compatible with uniaxiality, so all macroscopic properties will have the uniaxial symmetry.

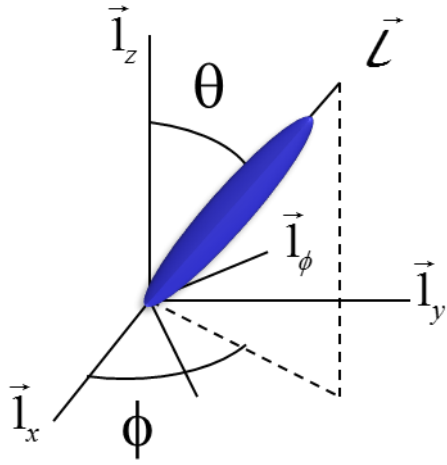


**Figure 1.4:** Illustration of the director orientation with respect to the *xyz* axis and definition of the azimuth $\Phi$ and inclination angle $\theta$.

If the director of the liquid crystal is along the z-axis, the dielectric tensor of a uniaxial material becomes:

$$\overline{\overline{\varepsilon}} = \begin{pmatrix} \varepsilon_{\perp} & 0 & 0 \\ 0 & \varepsilon_{\perp} & 0 \\ 0 & 0 & \varepsilon_{\parallel} \end{pmatrix} \tag{1.1}$$

If $\theta$ is the angle between the director and the *z*-axis and $\Phi$ the azimuthal angle between the projection of the director on the *xy* plane and the *x*-axis, then the director $\vec{\mathcal{L}}$ has coordinates:

$$\vec{\mathcal{L}} = \begin{pmatrix} \cos\phi\sin\theta \\ \sin\phi\sin\theta \\ \cos\theta \end{pmatrix} \tag{1.2}$$

Using the tensor transformation in a similar way as for the polarizability of nematic LC, the dielectric tensor can be found:

$$\overline{\overline{\varepsilon}} = \begin{pmatrix} \varepsilon_{\perp} + (\varepsilon_{\parallel} - \varepsilon_{\perp})\cos^2\phi\sin^2\theta & (\varepsilon_{\parallel} - \varepsilon_{\perp})\sin\phi\cos\phi\sin^2\theta & (\varepsilon_{\parallel} - \varepsilon_{\perp})\cos\phi\sin\theta\cos\theta \\ (\varepsilon_{\parallel} - \varepsilon_{\perp})\sin\phi\cos\phi\sin^2\theta & \varepsilon_{\perp} + (\varepsilon_{\parallel} - \varepsilon_{\perp})\sin^2\phi\sin^2\theta & (\varepsilon_{\parallel} - \varepsilon_{\perp})\sin\phi\sin\theta\cos\theta \\ (\varepsilon_{\parallel} - \varepsilon_{\perp})\cos\phi\sin\theta\cos\theta & (\varepsilon_{\parallel} - \varepsilon_{\perp})\sin\phi\sin\theta\cos\theta & \varepsilon_{\perp} + (\varepsilon_{\parallel} - \varepsilon_{\perp})\cos^2\theta \end{pmatrix} \tag{1.3}$$

The dielectric constants are temperature-dependent due to the temperature dependence of the order parameter. If the light is polarized along the director, the light experiences the extra-ordinary index:

$$n_e = \sqrt{\frac{\varepsilon_{\parallel}}{\varepsilon_0}} \tag{1.4}$$

If the light is polarized perpendicularly to the director, then the light experiences the ordinary refractive index:

$$n_o = \sqrt{\frac{\varepsilon_{\perp}}{\varepsilon_0}} \tag{1.5}$$

For most nematic liquid crystals, the dielectric constants at optical frequencies and corresponding values for the refractive indices are in the range:

$$\begin{matrix} 2\varepsilon_0 < \varepsilon_{\|}, \varepsilon_{\perp} < 4\varepsilon_0 \\ 0 < \varepsilon_{\|} - \varepsilon_{\perp} < \varepsilon_0 \end{matrix} \quad , \quad \begin{matrix} 1.4 < n_e, n_o < 2 \\ -0.2 < n_e - n_o < 0.4 \end{matrix} \qquad 1.6$$

The dielectric constant at low frequencies is also very important, because it determines how the liquid crystal will respond to an applied electric field. Typical values are in the range:

$$\begin{matrix} 5\varepsilon_0 < \varepsilon_{\|}, \varepsilon_{\perp} < 40\varepsilon_0 \\ -5\varepsilon_0 < \varepsilon_{\|} - \varepsilon_{\perp} < 20\varepsilon_0 \end{matrix} \qquad 1.7$$

Because of important contributions of orientation polarization, the dielectric constants at low frequencies are much larger. This is because most LC molecules have permanent dipole moments which partly align when a field is applied.

In applications, the surfaces containing the liquid crystal material play an important role in determining the director orientation. For most materials, the LC prefers to orient the director parallel with the surface without any azimuthal preference. This is called planar alignment. For some materials with specific chemical properties, the LC director prefers to be perpendicular to the surface. This is called homeotropic alignment. Polymer layers like Nylon 66 prepared in a particular way, by rubbing the surface with a soft textile with appropriate pressure lead to a preferential azimuthal alignment, usually in combination with a small deviation from the horizontal orientation (pre-tilt) as shown in Figure 1.5. The preferential orientation can be due to structural or chemical modification of the surface.

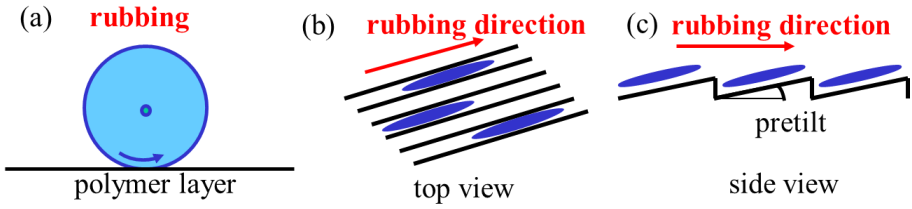


**Figure 1.5:** Illustration of the principle of an alignment layer based on a rubbed polymer layer: a) rubbing the polymer layer with a soft textile b) azimuthal alignment along the rubbing direction c) pre-tilt with the plane of the substrate.

If an electric field is applied to the liquid crystal, the electric torque experienced by a single LC is given by [1]:

$$\left|\vec{T}_e\right| = pE_{local}\sin\theta \qquad 1.8$$

With $E$ the local field related to the macroscopic field. If the permanent dipole moment is parallel to the long axis, the resulting torque tries to orient the molecule along the electric field direction (positive or negative) as shown in Figure 1.6.

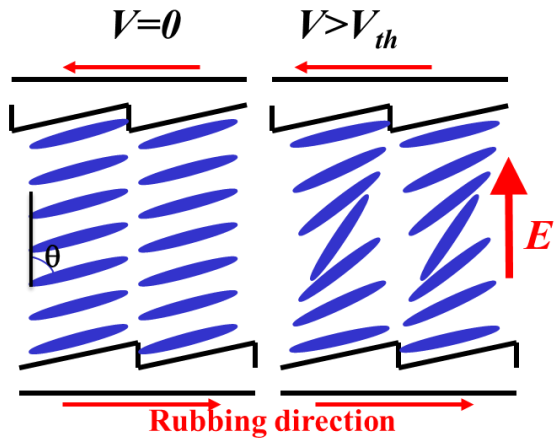


**Figure 1.6:** electrically controlled birefringence of LC medium

### 1.1.2 Chiral nematic liquid crystal

Chiral nematic Liquid Crystals (CLCs) arrange in a helical structure and form a regular and periodic structure. The refractive index is periodically modulated along the helical axis because of the particular arrangement of the director as shown in

Figure **1.7**a. The result is that the propagation of light is suppressed for a particular range of wavelengths. The wavelength region in which the light cannot propagate is the stop band. In this region, the light is selectively reflected due to the one-dimensional photonic band gap (PBG). Such colorful Bragg reflections can be observed from a CLC slab while the helix axis is perpendicular to the observation plane. Deviation from the perpendicular direction leads to a color shift in the reflection.

These materials are interesting because they exhibit self-ordering into periodic structures. Additionally, due to the soft matter nature of these materials and their response to external stimuli, it is possible to tune their behavior for wavelengths ranging from the near ultraviolet through the visible and up to the near infrared. The broad wavelength tuning range of CLC reflectors, coupled with their microscopic size could open up new possibilities for use in lab-on-a-chip devices, medical diagnostics, dermatology, spectrum analysis, laser arrays, displays [2-7], holography, optical rotators, notch filters, polarizers and reflectors [8].

The theory explaining the optical properties of CLC will be handled in section 2.1. From that theory I find that the width of the photonic band gap is $\Delta\lambda = \Delta nP$ with $\Delta n = n_e\text{-}n_o$ the LC birefringence and $P$ the pitch, which is equal to the distance to reach 360° rotation of the director. The long-wavelength band-edge, $\lambda_L$, and short- wavelength band-edge, $\lambda_S$ are given by $n_eP$ and $n_oP$, respectively. When an unpolarized light beam is incident on the planar CLC cell along the helical axis, the circularly polarized light of the same handedness as the chiral helix is reflected while the opposite handedness can propagate unhindered as shown in

Figure **1.7**a [9, 10]. Thus, a CLC cannot reflect more than 50% of normally incident unpolarized light. Most CLCs have a right handed helical structure like the scheme in

Figure **1.7**a. But there are also left handed helical CLCs in nature.

Figure **1.7**b shows photographs of beetles under right (R) and left (L) circular polarizers. The beetle with a single helical structure reflects only

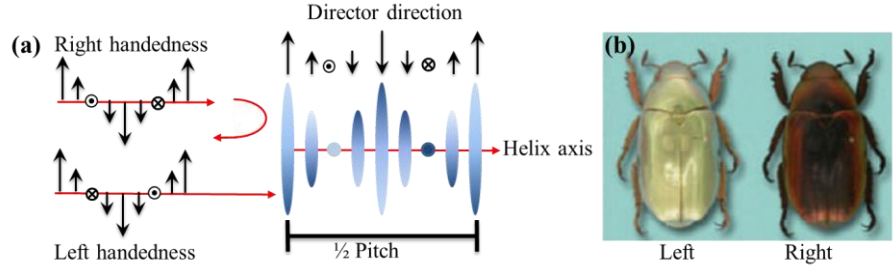


left circularly polarized light due to left handed CLC [11].

**Figure 1.7:** a) Configuration of the local director for chiral nematic LC. Circular polarized light with the same handedness is reflected. b) Photographs of a beetle which has a form of CLC on the outside. The reflection of right and left circular polarized light gives a completely different image [11].

### 1.1.3 Reactive liquid crystal

Reactive liquid crystals are a unique class of LCs that provide the additional benefit that the LC structure can be ‘frozen’ by means of polymerization. After polymerization, their mechanical properties are similar to other polymers and the structure is thermally stable. The polymerizable functional groups in the molecular structure offer the possibility for crosslinking and forming a long chain network while maintaining the order. In this work the functional groups are based on acrylate end groups. A reactive mesogenic monomer can be polymerized under certain conditions by UV or electron beam irradiation or temperature treatment.

Figure **1.8** shows a scheme of a planar LC network. Reactive LC can be coated onto flexible plastic substrates by a roll-to-roll coating process.

A few typical applications of reactive LCs are quarter and half wave retarders in consumer electronics, selective polarizer in goggles for 3D TVs and anti-reflection circular-polarizers for OLED displays [12]. Reactive LC can be used inside the display to form in-cell optical elements such as retarder foils for viewing angle enhancement in LCDs [13].

Polymeric films can be delaminated from the glass substrate so that they become free standing polymer films with sufficient mechanical strength and elastic flexibility [14]. Different types of reactive LC exist for various applications. In this project mono acrylate and di acrylate monomer are used including photo initiator and inhibitor. By UV irradiation, the photo initiator initiates a chain-addition polymerization of the reactive groups and the monomer orientation is frozen into a densely cross-linked network.

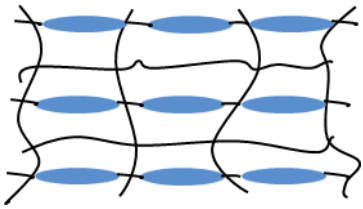

**Figure 1.8:** Scheme of planar LC polymer

## 1.2 Nanorods

A nanorod is a nanocrystal (NC) consisting of several thousands of atoms that may exhibit size quantization effects. When the size of a material reduces to the nanoscale, the percentage of atoms at the surface becomes considerable to the total number of atoms. Hence, the material exhibits size-dependent properties. Quantum confinement in semiconductors leads to discrete electron energies [15, 16] and superparamagnetism in magnetic crystals [17]. In some metallic crystals, the resulting effect is the appearance of a surface plasmon resonance [18, 19].

When a semiconductor absorbs a photon, this creates an electron-hole pair (exciton) with a characteristic distance. However, creating an exciton in a nanocrystal that is smaller than the bulk exciton radius requires more energy compared to bulk material. This translates into an increase of the effective band gap, illustrating the size-dependent properties which differ from the bulk material as shown in Figure 1.9a. Due to these discrete energy levels and the size-dependent energy difference between the first levels of the conduction and valence band (band gap), these semiconductor NCs exhibit quantum confinement [20].

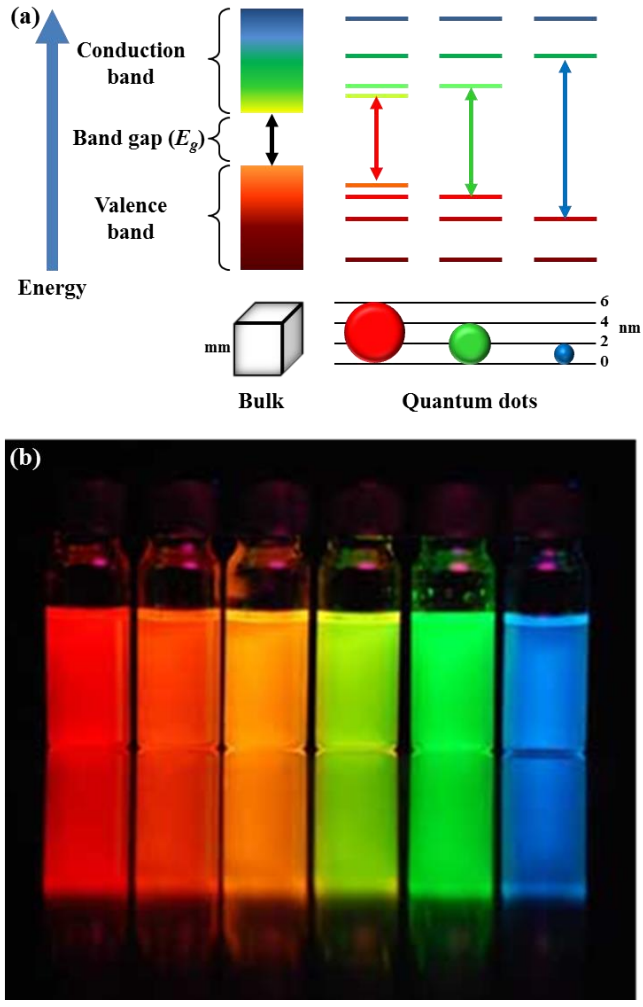


**Figure 1.9:** a) Semiconductor energy levels of bulk and nanocrystals b) Luminescence of CdSe particles with diameters between 2 and 6 nm under UV light, showing quantum confinement in action. Photo taken by I. Moreels, Physics and Chemistry of Nanostructures group, UGent.

Semiconductor crystals in which the exciton is confined in all three dimensions are called quantum dots (QDs). Crystals with confinement in two or one dimensions are called quantum wires (nanorods) and quantum wells, respectively.

A correct model for QDs must include the Coulomb attraction between electron and hole. In most cases, a sphere is a good approximation for the

particle shape. The Schrodinger equation for such a 'particle in a sphere' system was first solved by Louis E. Brus in 1986[21], leading to the Brus equation:

$$E_g = E_{g,Bulk} + \frac{\hbar^2 \pi^2}{2\mu_{ex} R^2} - \frac{1.8e^2}{\varepsilon R} \qquad 1.9$$

Where $\varepsilon$ is the dielectric constant, $R$ the particle radius, $\hbar$ the reduced Planck constant and $\mu_{ex}$ the effective mass of the exciton. This equation shows that the band gap energy $E_g$ of a QD is larger (blue shifted) than the bulk band gap $E_{g,Bulk}$. Also the equation shows that by tuning the size of the QDs the bandgap can be engineered to have optical properties from UV to IR. Hence, size confinement is the basis of the exceptional optical properties in colloidal QDs. This is illustrated by the suspensions of luminescent colloidal CdSe particles in Figure 1.9b, where reducing the particle diameter from 6 to 2 nm results in a shift of the luminescence from red (6 nm particles) to blue (2 nm particles).

Whereas size is the key parameter underlying quantization in semiconductor NCs [16], shape often adds unique possibilities to further adjust NCs properties [22]. In this respect, shapes such as nanorods and platelets stand out since their shape anisotropy results in an anisotropic interaction – absorption, emission or scattering – with light [23]. Metallic NRs, for example, exhibit a splitting of the localized surface plasmon resonance into a longitudinal and transversal mode that most strongly interacts with light polarized perpendicular or parallel to the long axis of the rod, respectively [18]. Rod-like colloidal semiconductor nanocrystals on the other hand, absorb more strongly and emit light polarized parallel to their long axis [24, 25].

Although use can be made of the anisotropic properties of single NRs [18, 26, 27], applications such as polarized light emitting diodes [28], photovoltaic energy conversion, optical sensors or switches [29-32] require layers or volumes with large ensembles of aligned NRs.

In this work, CdSe/CdS dot-in-rod is used as a heterostructure system. It consists of a CdSe QD core encapsulated in a rod shaped CdS shell [33]. The quantum yield observed in these systems can be up to 75% which makes them attractive for applications such as LED, bio-imaging etc. Literature reveals that these systems exhibit highly polarized emission from the first exciton transition, which is an interesting attribute to this system [24]. These systems also exhibit polarized absorption at the first exciton transition. In

this work, the CdSe/CdS NRs with two different sizes are synthesized by Dr. Tangi Aubert at the 'Physics and Chemistry of Nanostructures' research group at Gent University under the supervision of professor Zeger Hens.

Transmission electron microscopy (TEM) analysis is an indispensable tool for the characterization of nanocrystals. It gives valuable information on the size, morphology, crystal structure and chemical composition of the synthesized nanocrystals. Figure 1.10 shows a TEM image of the synthesized CdSe/CdS NRs.

More detail about the synthesis of these NRs are in appendix A, paragraph 1.

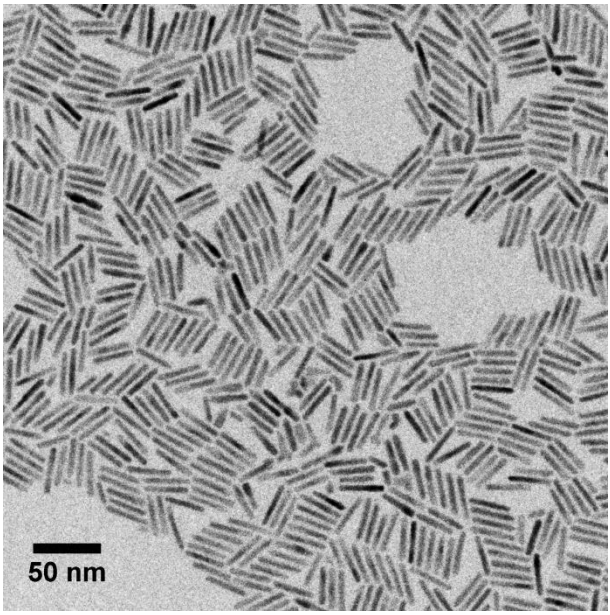


**Figure 1.10:** TEM image of the CdSe/CdS dot-in-rods on a copper grid coated with a carbon film.

## 1.3 Thesis overview

The research in this dissertation mainly focuses on the fabrication of thin films for optical devices based on reactive and non-reactive LCs and NRs such as: thin film polarizers, thin film reflectors, microsecond tunable shutters and thin film polarized emitter. The lab process can be modified to roll to roll process for industrial application. QDs are commercially used in TVs by companies like Sony, Samsung and LG. The cost of the materials

will probably go down in the future. As the fabricated layers are thin, the industrial fabrication should not be expensive.

The thesis is organized as follows:

In chapter 2 the formula of light propagation in CLCs is given and simulations of the PBG are shown with varying parameters of the CLC film. The employed reactive LCs in this project are introduced in section 2.2. Then the fabrication of a thin film polarizer and color filter based on photo-polymerization reactive LC is demonstrated. Thin film polarizers are fabricated for applications which require very small thicknesses of the final device. One example are electro-active contact lenses [34] [35].

A technique to make a mono domain CLC thin film color filter is demonstrated in section 2.3.2. These films are suitable to be processed in optical device manufacturing as additional films or as in-cell optical components.

In chapter 3, a tunable chiral nematic liquid crystal optical filter with microsecond switching time based on a mixture of reactive and non-reactive CLC is demonstrated. The blue shift of the PBG with applied voltage is demonstrated in section 3.2. The influence of the amplitude of the applied voltage on the location of the PBG is investigated in section 3.3. Further analysis deals with the measurement of the Stokes parameters of the transmission of linearly polarized light as well as response time of the filter. UV curing conditions are investigated in section 3.5. A microsecond-range optical shutter for unpolarized light is demonstrated in section 3.6.

In the rest of this dissertation I focus on techniques for aligning NRs.

In chapter 4, the aim is to understand the electro optic behavior and the alignment of the colloidal CdSe/CdS NRs that are dispersed in a non-polar solvent by applying a sufficiently strong electric field. I review and extend the theory for dynamic orientation of NRs. Important parameters in this theory are the viscosity of the liquid, the rotational diffusion, the torque due to the permanent dipole moment and the (induced) dielectric torque. The degree of alignment is monitored by measuring the transmission as a function of time during the application of a time-dependent voltage. By studying the voltage dependence of the alignment and comparing this with the theory, I am able to evaluate the magnitude of the permanent dipole moment of the NRs. From the measurements I can also estimate the absorption anisotropy, the threshold voltage and the critical frequencies for alignment of the NRs.

I propose four novel techniques to homogeneously align CdSe/CdS NRs and to obtain a thin film polarized emitter in chapter 5. Aligning NRs with the dip coating method assisted by an electric field is demonstrated in section 5.2. Moreover, the alignment of NRs in reactive LC and polymer is investigated. In section 5.5, I demonstrate aligned NR films made of aligned polyvinylpyrrolidone (PVP) nanofibers assisted by electrospinning.

A conclusion and some final remarks are given in chapter 6, together with some suggestions for further development of the fabricated devices.

The details of the synthesis of the NRs and Characterization techniques are explained in appendix A. The details of nanofiber fabrication are described in appendix B. Figure 1.11 illustrates a number of fabricated optical films based on the use of reactive & non-reactive LC and NRs.

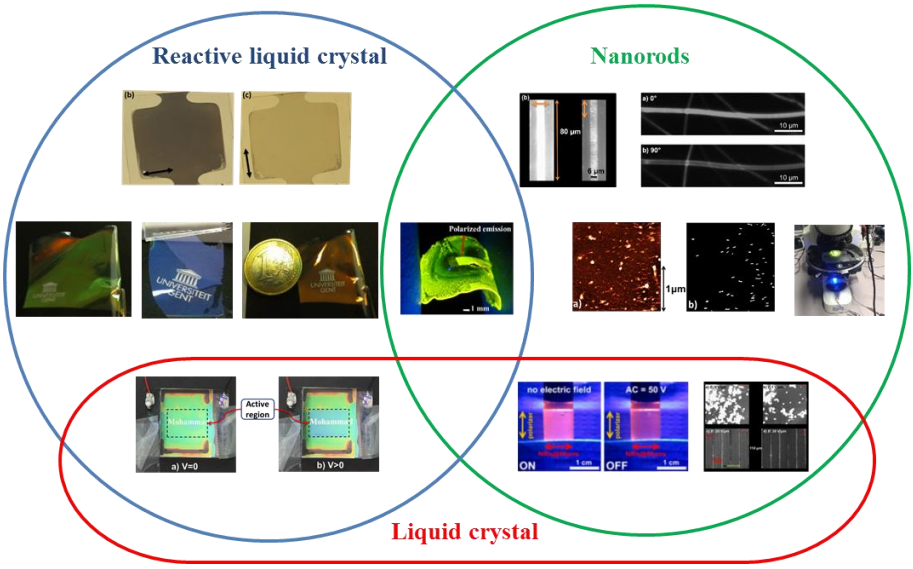


**Figure 1.11:** An overview of the fabricated optical films based NRs and reactive and non-reactive LC.

# Chapter 2

# Thin film polarizer and color filter

In this chapter, the formula of reflection near the PBG of CLC is given and simulated. In addition, I present a method to fabricate a thin film color filter and polarizer based on a mixture of photo-polymerizable liquid crystal. The thin film color filter is based on reflection and fabricated using chiral dopant. The thin film polarizer is based on absorption and developed by using a color-neutral (black/gray) dye. Main results of this chapter are already published in [7] and [9].

## 2.1 Theory of light propagation in CLC and simulation

The theory of light propagation in CLC can be found in different books [36]. A positive uniaxial liquid crystal material with $n_o$ and $n_e$ is assumed. Also is assumed that the optical axis of the molecule in CLC remains in the *x–y*-plane but its orientation depends on the z-position with a periodicity of the pitch *P*. For illustration, the case of normal incidence light with the same handedness as the CLC is investigated.

Eq. 2.1 gives the reflectance for a CLC layer with thickness *d* for normal incidence when absorption and partial reflections at the interface with the substrate can be neglected:

$$R = \frac{|\kappa|^2 \sinh^2 sd}{s^2 \cosh^2 sd + (\frac{\Delta k}{2})^2 \sinh^2 sd} \qquad 2.1$$

Where:

$$\kappa = \frac{\pi(n_e^2 - n_o^2)}{\lambda\sqrt{2(n_e^2 + n_o^2)}} \qquad 2.2$$

$$k = \frac{2\pi}{\lambda}\sqrt{\frac{n_e^2 + n_o^2}{2}} \qquad 2.3$$

$$\Delta k = 2k - \frac{4\pi}{P} \qquad 2.4$$

$$s^2 = \kappa^2 - (\frac{\Delta k}{2})^2 \qquad 2.5$$

$n_e$ and $n_o$ are the extra-ordinary and ordinary refractive indices of the liquid crystal and *P* is the pitch. The transmission is simply $T = 1 - R$. At the center of the PBG, $\Delta k = 0$ and the reflectance is maximum:

$$R = \tanh^2 \kappa d \qquad 2.6$$

The typical shape of such reflectors is rectangular-like with so-called sidelobes. The reflected spectrum depends on material properties of the CLC: $n_o$ and $n_e$, thickness and pitch. The high reflectivity band starts at the wavelength $\lambda = P n_o$ and ends at $\lambda = P n_e$. The bandwidth is defined as $\Delta\lambda = P(n_e - n_o)$. Equation 2.6 reveals that high reflectivity can be obtained by increasing the anisotropy and the thickness of the CLC. Figure 2.1a shows the simulated transmission for samples with 4 µm thickness and different birefringence values. The difference between regular dielectric reflector and CLC are different forms of the Bragg condition and the value of the propagation constant $\kappa$. Figure 2.1b shows the simulated transmission of samples with $\Delta n = 0.163$ and different thicknesses. The bandwidth of the PBG increases with increasing the birefringence and decreases with increasing the thickness. The reflectivity within the PBG increases and the sides are more rectangular with increasing thickness or increasing birefringence. A fit of the measurement results with the theoretical curves reveals that the polymerized mixture has a birefringence of 0.16.

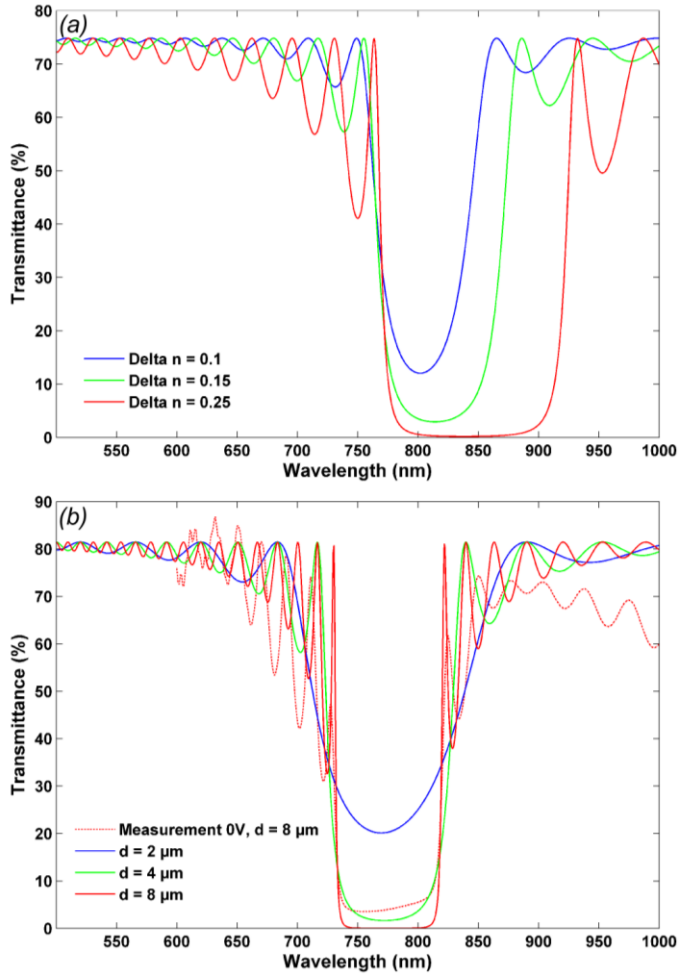


**Figure 2.1:** Simulated transmission spectra for right handed polarized light for a) cells with 4 µm thickness and 3 different values of the birefringence; b) cells with Δn=0.163 and different thicknesses (the dotted line is a measured transmission spectrum).

## 2.3 Photo-polymerization of reactive liquid crystal

Photo-polymerization of aligned liquid crystalline mono(di)acrylate monomers is an elegant and versatile method to form oriented and structured liquid crystal (LC) polymers. The liquid crystalline mono(di)acrylates can be aligned easily, similar to non-reactive nematic LCs. The photo-polymerization process freezes the orientation of the liquid crystals and keeps the anisotropic optical properties of the films. Homogeneous and

birefringent optical films based on liquid crystalline mono(di)acrylate monomer can be applied to improve the performance and properties of optical devices such as displays, lasers, color filters, retarders and polarizers. The optical function can be optimized by tuning the anisotropic properties and by controlling the orientation and order of these compounds before photo-polymerization. The optimized optical functions are stabilized by the formation of a cross-linked network through photo-polymerization of these compounds.

### 2.3.1 Thin film color filter

The thin film color filter in our project is based on chiral nematic liquid crystals. I was able to make thin films of these color filters using the photo-polymerization method and by adding appropriate chiral dopant to the liquid crystalline mono(di)acrylate monomers.

### 2.3.2 Thin film polarizer

A second possibility is to use non-chiral LC and instead of using reflection of light, absorb the light. To achieve selective light absorption, absorbing dye molecules are mixed with the LC. The fabricated thin film polarizer absorbs light that is polarized parallel to the *c* axis of the LC.

## 2.4 Device structure and fabrication

The photo polymerizable mixture is prepared by mixing 30 wt% liquid crystalline monoacrylate monomers (RM105, Merck) and two liquid crystalline diacrylate monomers (RM257, 43 wt% and RM82, 20 wt%,Merck). The physical properties of the liquid crystalline diacrylate monomer (RM257) given by the material supplier, indicate that the refractive indices for ordinary and extraordinary light are $n_o$ = 1,508, $n_e$ = 1,687 and the melting and clearing points are 66°C and 127°C, respectively. To increase the nematic range down to room temperature, other liquid crystalline monomers (RM82-RM105) are added to the mixture. The photo initiator (Irgacure 819, 3 wt%, BASF) is added to the mixture and an inhibitor (tert-Butylhydroquinone, 4 wt%, Sigma-Aldrich) is added to inhibit thermal polymerization reactions. To obtain color filter material, the right handed chiral dopant (BDH1305, Merck) is added to the mixture. The photonic band gap of the color filter is tunable by selecting the appropriate chiral dopant concentration. The chemical structure of the above materials is

shown in Figure 2.2. For the thin film polarizer, a black dichroic dye is added to the mixture instead of chiral dopant.

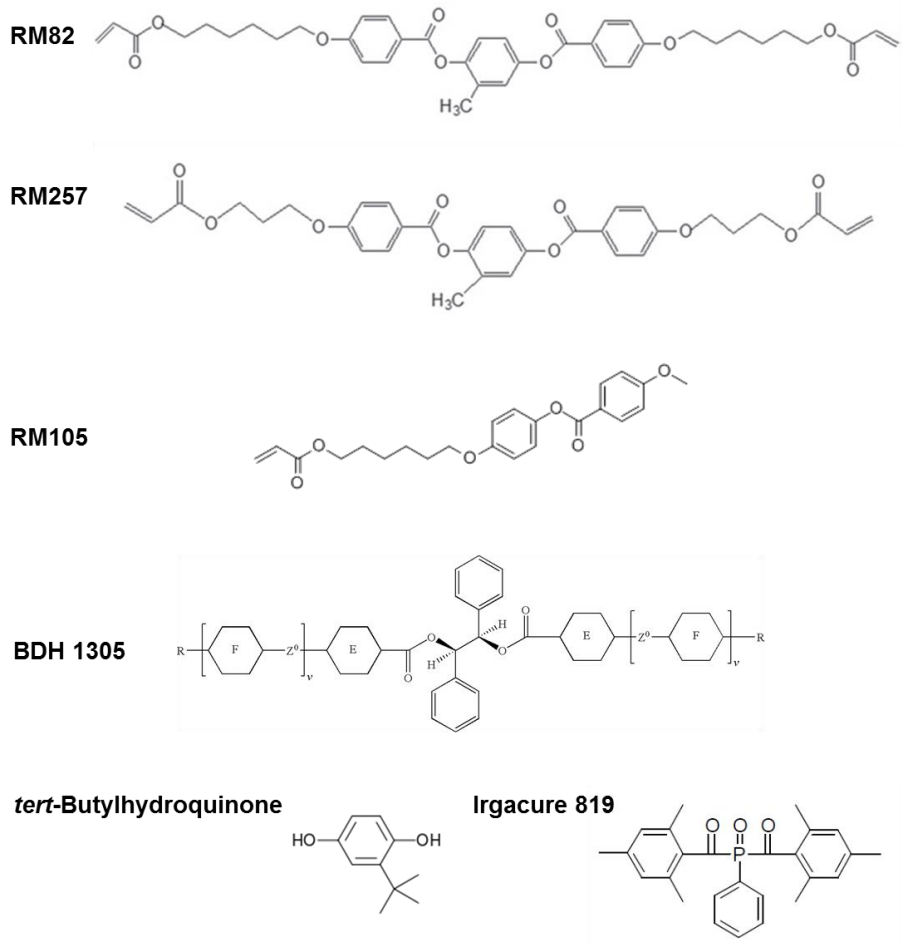


**Figure 2.2:** Chemical structure of two liquid crystalline diacrylate monomers having side groups of different lengths (6-carbon spacers for RM82 and 3- carbon spacers for RM-257), liquid crystalline monoacrylate monomer (RM105), chiral dopant (BDH 1305), inhibitor (tert-Butylhydroquinone) and initiator (Irgacure 819).

The mixture is mixed with a magnetic stirrer. The cells are fabricated with two glass substrates with a 30 nm thick conductive Indium-Tin-Oxide (ITO) electrode coating. The ITO layer is not necessary in the initial devices that are made but will be crucial for later devices. The substrates are coated with a layer of nylon 66 (thickness approximately 300 nm) and rubbed anti-parallel in order to stabilize the CLC in the planar texture with the helical

axis perpendicular to the glass substrates. The gap in the empty cell is determined by spacers balls (Sekisui chemical) mixed inside the glue. In this work different spacers (4-12µm) are used. The composite mixtures are injected into the empty cells using the capillary effect in vacuum on a hot stage in the isotropic phase (92°C) of the polymerizable LC mixture. The cells are cooled down such that the liquid crystal can orient itself into a helical structure (planar structure in case of polarizer) as a uniform film without domains. The cooling rate is 0.3 °C/min and has an important role for the uniformity of the film. Figure 2.3 a,b show images of a color filter which is not treated and Figure 2.3 c,d show images of a treated color filter. Figures a,c are with a smaller magnification than figures b,d. These figures clearly indicate the significant role of the cooling rate treatment. The dye molecules also align to the direction of LCs in the cell. Then the cell is exposed to UV light (30 mW/cm) from a mercury lamp (with the main power at 365 nm and a blocking filter for short and long wavelengths) for 1 minute to polymerize the CLC mixture and polarizer mixture. In order to have a stand free film, the top glass of the cell can be delaminated by using a cutter. In the second step, the thin film can be detached from substrate elegantly by a cutter or tape.

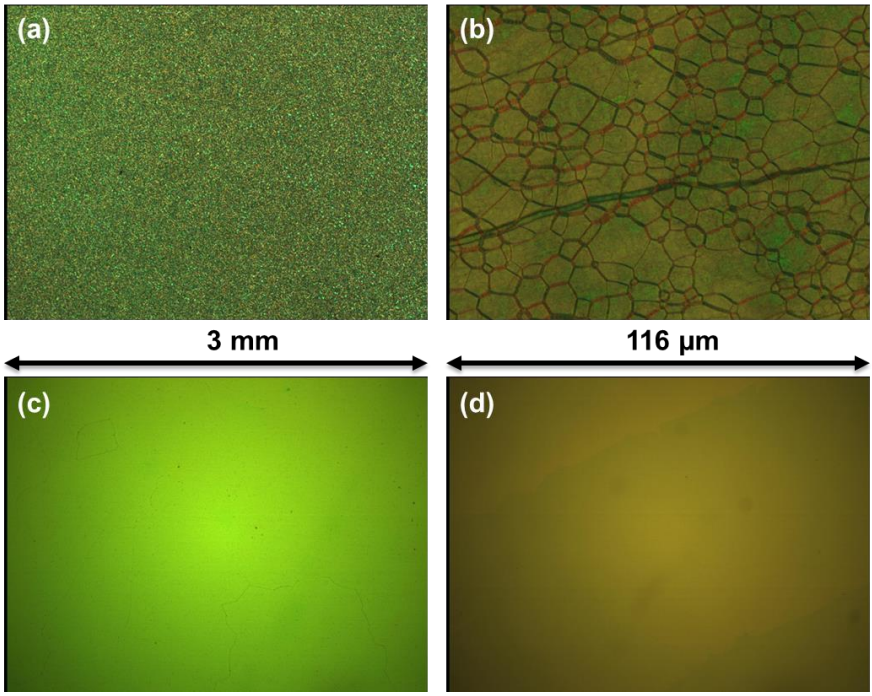


**Figure 2.3:** Photographs of the color filters a, b) without and c, d) with cooling rate treatment for two dimensions.

## 2.5 Measurements and Results

### 2.5.1 Dye doped thin film polarizer

A 6 µm polarizer is formed with mono-domain uniform planar orientation of the LC. The structure of the dye-doped polarizer is schematically shown in Figure 2.4a. The dye-doped polarizer is placed onto a conventional polarizer with the LC director either perpendicular (Figure 2.4b) or parallel (Figure 2.4c) to the conventional polarizer direction. The micrograph in Figure 2.4d indicates mono-domain uniformity of the thin film polarizer.

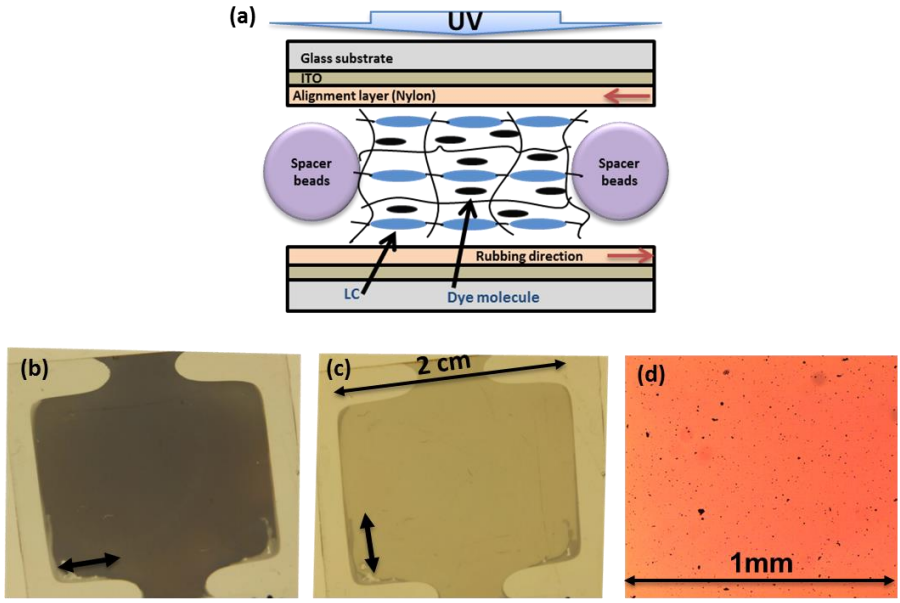


**Figure 2.4:** a) Structure of a polymerized dye-doped polarizer. b) A photograph of a 6 µm thin film dye-doped polarizer with a 2×2 cm2 region placed on another polarizer with b) perpendicular and c) parallel orientation.d) micrograph of the texture with mono-domain uniformity.

To quantify the optical properties of the dye-doped polarizer, the transmittance of the polarizer is measured by using a spectrophotometer (Perkin Elmer). The cell is placed in the photospectrometer such that the LC director is either parallel ($T_{//}$) or perpendicular ($T_{\perp}$) to the incident polarized light. The resulting graphs are shown in Figure 2.5. The films show a broad absorption ranging from 400 nm to 650 nm. The contrast of the polarizer is defined as the ratio of $T_{//}$ and $T_{\perp}$. The maximum contrast of 9 is obtained at a wavelength of 550-600 nm. These results confirm the fact that the long axis of the dyes are oriented along the LC direction. Its anisotropic orientation is maintained after the photo-polymerization process. The contrast ratio is rather low compared to commercial film polarizers which easily reach contrasts of 5000. These commercial polarizers however are typically several tens or hundreds of micrometer thick. The application of such thin film polarizers can be interesting when very small thicknesses of the final device is required. One example are electro-active contact lenses [34] [35].

It is known that the nematic phase results in a rather low dichroic dye order parameter and a low dichroic ratio. Using smectic phases, the dichroic ratio and hence the contrast of the film can be improved drastically [37, 38].

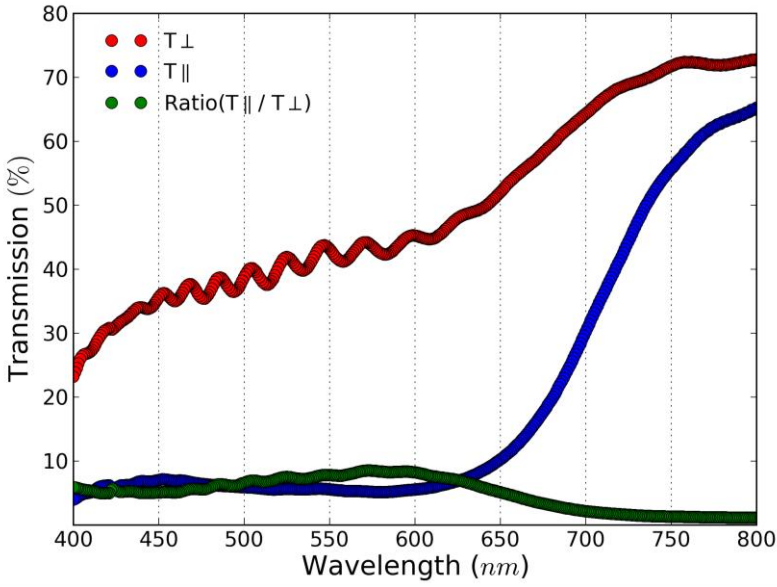


**Figure 2.5:** Optical properties of a 12 µm thin film dye-doped polarizer. T// (T⊥) is the transmittance when the aligned LC direction is parallel (perpendicular) to the polarization of incident light.

### 2.5.2 Thin film color filter

A CLC polymer film is formed exhibiting selective reflection of right handed circularly polarized light. The color filter film is otherwise transparent without observable scattering. The schematic structure of the CLC polymerized color filter are demonstrated in Figure 2.6a. A number of CLC color filters are made by using mixtures with different chiral dopant concentrations. The photographs of the CLC polymerized color filters are depicted in Figure 2.6b. The color filters are placed on a black background on which the UGent logo is printed in white. The image clearly indicates that the cell does not scatter light thanks to the mono domain structure. Obtaining a monodomain CLC layer is technologically quite challenging. Controlling the cooling rate of the oven is crucial for a good CLC layer. If the cooling rate is too fast or too slow, the CLC layer would have a lot of domains. Also a uniform layer thickness is required. For this approach, spacers with uniform size distribution (coefficient of Variation, Cv < 7%) are used to ensure monodomain CLC layer.

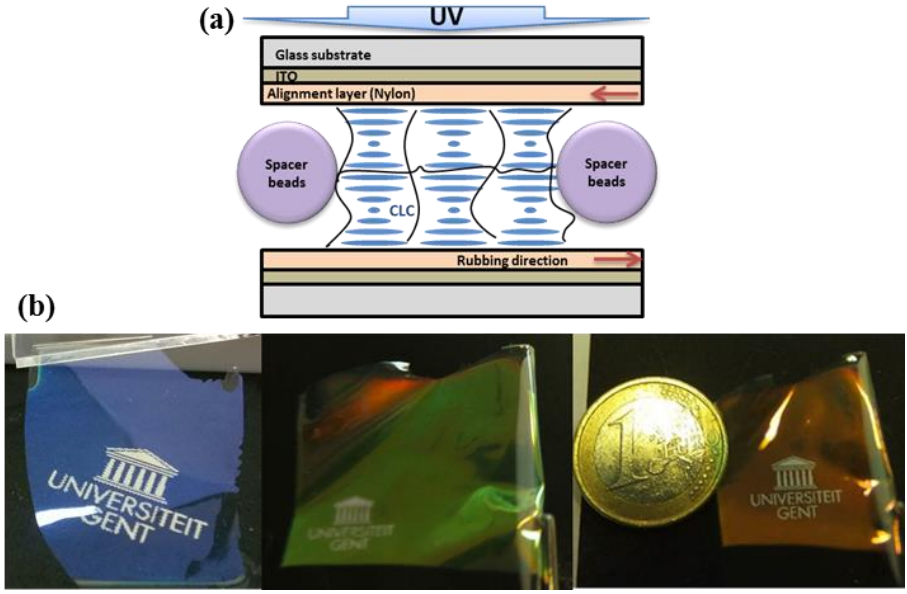


**Figure 2.6:** a) Structure of a polymerized CLC color filter. b) Photographs of 8 µm thin film polymerized CLC color filters placed on a black background on which the UGent logo is printed in white to illustrate the lack of scattering.

To investigate the quality of the photonic band gap, the transmission spectra of the cells for unpolarized light are measured by a spectrophotometer. The fabricated CLC films exhibit a broad PBG with a total bandwidth of approximately 80 nm and good reflectivity (almost 50%) in the PBG region as shown in Figure 2.7. The photonic band gap of the devices shifts to the blue by increasing the concentration of the chiral dopant. The reflected light shows strong color saturation because of the sharp band edges.

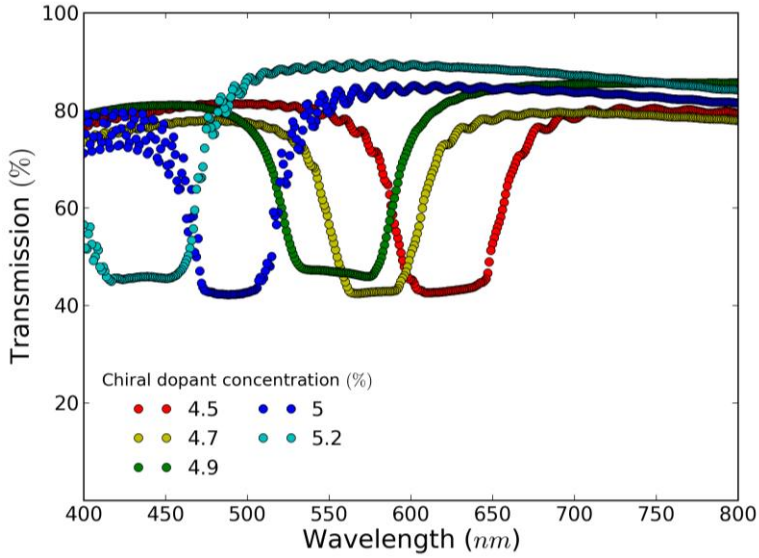


**Figure 2.7:** Transmission spectra (for unpolarized light) for 8 µm thin color filters with various concentrations of chiral dopant. Almost 50% of the incident light is reflected in the photonic band gap.

### 2.5.3 Features

The thin film polarizer and color filter feature good resistance for polar protic solvents e.g. formic acid, isopropanol, ethanol and water and are thermally stable up to 100°C. The films can be detached from the substrate and applied inside a cell or they can be used in flexible optical devices such as flexible displays or electro-active contact lenses. It is also possible to photopattern the color filter and polarizer by using selective photo irradiation through a photomask, which is required for the realization of 3D displays. Compared to previously reported polymerized thin films [8, 39, 40], the new method provides a mono domain thin film. Hence the incident light does not scatter.

## 2.6 Conclusion

In this chapter I have explained the basic theory of reflection near the PBG of CLCs. The transmission of a CLC layer as a function of wavelength is simulated for various thicknesses and birefringences. I have demonstrated a CLC thin film color filter and dye-doped polarizer with photo-polymerization of liquid crystalline mono(di)acrylate monomers. The PBG

of the color filter is around 80 nm with strong color saturation without absorption because of the sharp band edges. The thin color filter is interesting for polarizer-free reflective displays and smart switchable reflective windows to control solar light and heat.

The thin film dye-doped polarizer has a broad absorption band between 400 nm and 650 nm and has a contrast ratio of 9 for a film of only 12 µm thick. Both thin films feature excellent film characteristics without domains and can be detached from the substrate which is useful for e.g. flexible substrates. These films have thermal stability up to 100°C and chemical resistivity for polar protic solvent and are suitable to be processed in optical device manufacturing as additional films or as in-cell optical components.

---

"Sitting with the intelligent is a sign of successfulness. A sign of a scholar is his self-criticism of his sayings and his acquaintance with the various hypotheses".

"The true stingy is that who refrains from greeting".

Hossein ibn Ali

---

# Chapter 3

# Widely tunable optical filter and shutter with microsecond switching time

In the previous chapter I have fabricated devices which cannot be switched with an applied voltage because the liquid crystal mixture consists mostly of reactive components (except for the chiral dopant). In this chapter I will use a considerable amount of non-reactive liquid crystal in the mixture which will form small islands in the polymer film that can react to an applied electric field. Using this technique CLC layers are formed with very small droplets that react to the voltage and make it possible to change the optical properties of the CLC film. To make the difference clear with the films from the previous chapter I call the films developed in this chapter Partly Polymerized CLC (PPCLC). As already mentioned, this PPCLC film consists of a mixture of photo-polymerizable liquid crystal, non-reactive nematic liquid crystal and a chiral dopant that has been polymerized with UV light. In order to obtain films with high transmission and low scattering, it is necessary that the non-reactive LC forms very small droplets. The size

of these droplets should be much smaller than the wavelengths for which the device should operate. If I consider a wavelength of 500 nm, then ideally a factor 10 in size would require droplets of 50 nm or smaller. As will be shown in this chapter, the key factor to obtain such small droplet sizes is the concentration of non-reactive LC. Additionally, a blue-wavelength shift of the photonic band gap is obtained as a function of power, duration time of UV illumination and thickness of the cells. I investigate a number of other parameters such as the influence of the amplitude of the applied voltage on the width and the depth of the reflection band.

Finally a fast electro-optic shutter is fabricated and demonstrated that works independently of the polarization state of the incoming light beam. This is exceptional because, most of the commercial and reported liquid crystal shutters only work for linearly polarized light [41, 42]. The device consists of two PPCLCs separated by a half wave plate. I will demonstrate further in this chapter that high contrast and high transmission in the bright state can be obtained with microsecond switching times. The transmission modulation is due to a 50 nm wavelength shift of the photonic band gap of the chiral liquid crystal realized by applying an electric field over both PPCLCs. Main results of this chapter are already published in [5][7] and [10].

## 3.1 Introduction

Similar to a distributed Bragg reflector (DBR), as already introduced in section 2.1, the periodicity of a CLC acts as a 1D Photonic Band Gap. Direct control and tuning of the PBG are of crucial importance for several emerging applications: photonic information technology, lab-on-a-chip devices, and switchable optical devices such as sensors [43], reflectors, diffraction gratings, polarizers, shutters, notch- and band-pass filters, reflective displays, mirror-less and ultralow threshold tunable lasers and modulators [31, 44]. Significant efforts have been devoted to tuning of the PBG using external stimuli such as heat [45-48], light [49-51], elasticity [52] and electricity [44, 53-63]. Up to this point, almost all CLC devices have relatively slow switching characteristics in the order of several ms or a small tuning range which encumbers the use in practical applications. The most common technique for tuning is changing the pitch $P$ [43, 45-56]. Direct electronic control of the PBG is difficult because the periodic structure may deform non-uniformly and the Bragg reflection may be disrupted under the application of an electric field [9, 60, 63]. When an electric field is applied parallel to the helical axis, the CLC molecules (with positive dielectric

anisotropy) tend to align parallel to the direction of electric field and the homogeneity of the structure is distorted [64, 65]. Helfrich has shown that the orientation pattern of cholesteric liquid crystals can be unstable in electric and magnetic fields and proposed a model for the so-called Helfrich deformation [66, 67]. In addition there can be a deterioration of the helical structure due to the presence of electro-hydrodynamic instabilities (EHDIs) at low frequencies [10, 47, 68]. The so-called focal conic structure is highly scattering and is used in certain devices such as eReader LCDs from Kent Displays. Some researchers have used polymer-stabilized CLC to tune the PBG [58, 69-76]. Yet the deterioration of the structure has remained a significant problem. Choi *et al*. [56] controlled the PBG by using ferroelectric liquid crystal (FLC) in CLC with a relatively large tuning range of ~101 nm but a slow response time of ~280 s. A further limitation of this method is the fact that the liquid crystalline mixtures possess negative dielectric anisotropy and therefore have a small birefringence and narrow PBG.

Choi *et al*.[57] have demonstrated wavelength tuning of the PBG from a hybrid structure consisting of an achiral nematic liquid crystal and a periodic polymer template. The resulting wavelength tuning is relatively fast and broadband with a response time of ~43 µs and a bandgap of ~100 nm. However only the long wavelength photonic band edge shifts to the blue, while the short band edge is fixed. In this method there is a reduction of the reflectivity in the reflection band, which makes them less suitable for some applications such as liquid crystal lasers. Recently Inoue *et al*. [59] fabricated a CLC laser that can be tuned continuously with a response time of less than 1 ms with a 30 nm blue shift, based on the modulation of the refractive index to control the selective reflection band. It is desirable to have a switchable PBG with fast response to electrical addressing and tuning over a broad wavelength range with high reproducibility without deformation and degradation.

In this work, a shift of the photonic band gap of up to 141 nm and response times of 50 µs (switching ON) and 20 µs (switching OFF) are reported. The resulting CLC layers are stable when applying high voltage. Additionally, the amount of reflection in the PBG remains at the same level when shifting the PBG.

## 3.2 Fabrication

Chiral liquid crystal mixtures are made by dissolving reactive LC monomers (different mono- and diacrylate compounds from Merck), non-reactive nematic LC (MDA-00-3536, Merck, further referred to as 'MDA'), photo initiator (Irgacure 819, BASF), inhibitor (tert-Butylhydroquinone, Sigma-Aldrich) and right-handed chiral dopant (BDH1305, Merck) in chloroform after stirring for 20 minutes. The relative ratio of reactive and non-reactive LC is varied and different mixtures are prepared with non-reactive LC ranging from 40 to 60 wt%. It is possible to make devices for different operation wavelengths by selecting the appropriate chiral dopant concentration.

The clearing point is close to 102°C for all mixtures. The composite mixture is injected into an empty cell using the capillary effect in vacuum on a hot plate in the isotropic phase. The cell consists of two glass substrates with 30 nm thick conductive Indium-Tin-Oxide (ITO) electrodes, coated with a nylon layer which is rubbed in an anti-parallel way. In this way the CLC is stabilized in the planar texture with the helical axis perpendicular to the glass substrates. The empty cell is sealed with different spacers of 4, 6.75 or 8 µm. The cell is cooled down to room temperature with a rate of 0.3 °C/min to form a homogeneous film without domains. Then the cell is exposed from one side to 30 mW/cm$^2$ UV light (365 nm) from a mercury lamp with appropriate band pass filter for 1 minute to polymerize the CLC mixture.

After polymerization, a chiral LC polymer is formed with selective reflection of right circularly polarized light. For the compositions and UV intensities I observed that the cell remains transparent without observable scattering. This indicates that the droplets of nonreactive LC that have formed in the cross-linked network are smaller than 50 nm. To control the behavior of the CLC films, the concentration of nematic LC and the UV dose for curing are controlled.

## 3.3 Measurements

To investigate the influence of the concentration of nonreactive LC inside the network, mixtures with 40, 50 and 60 wt% of MDA concentration are used in cells with 4 µm thickness. After fabrication, the transmission spectra of the samples are measured by a photospectrometer (Perkin Elmer) while applying a sinusoidal voltage signal of 1 kHz with RMS electric field between 0 and 247 V/µm. The fabricated CLC films exhibit a broad PBG centered between 800 and 900 nm with a total bandwidth of approximately

100 nm. The blue shifts of the PBG for devices with 40, 50 and 60 wt% MDA concentrations are shown in Figure 3.1a-c respectively. The devices with 40 wt% nematic LC show the strongest blue shift, equal to 141 nm. Unfortunately this mixture exhibits the highest threshold voltage (90 V/µm) and suffers from electric breakdown before saturation of the wavelength shift is observed. The sample with 50 wt% MDA shows a 114 nm blue shift, with a 65 V/µm threshold. The cell with 60 wt% MDA shows a low threshold voltage of 35 V/µm but breakdown occurs after a 48 nm shift. Apparently the non-reactive LC exhibits a lower breakdown electric field than the polymerized components. In principle other liquid crystal materials with a higher breakdown voltage may be used, based on fluorinated compounds which typically exhibit a lower ionic content. In principle a higher concentration of nematic LC causes more and larger voids inside the polymer network which facilitates the reorientation of the nematic LC. This leads to the lower threshold in the device with 60 wt% MDA. The shift of the long band edge wavelength of the PBG as a function of the applied electric field for devices with 40, 50 and 60 wt% MDA concentration is shown in Figure 3.1d. It illustrates that the shift is continuous and the degree of modulation of the device with 40 wt% MDA concentration is larger than the others. By decreasing the MDA concentration to 20 wt%, the threshold voltage increases and the blue shift is only a few nanometer. Note that the IR absorption in Figure 3.1a and c is slightly higher due to thicker ITO electrodes (200 nm), compared to Figure 3.1b (30 nm ITO thickness). The concentration of photo initiator is a key factor to obtain small droplet sizes and to speed up the photo-polymerization process, such that the reactive and non-reactive LC do not get the time to separate. If the concentration of photo initiator is not high enough, the droplets of LC will be big and cause scattering. If the concentration of photo initiator is too high, it causes domains in the layer. Another crucial parameter is the concentration of inhibitor. If the concentration of inhibitor is not enough, the mixture starts to polymerization before UV curing due to uncontrollable stimuli such as thermal stimulation. Also if the concentration is too high, it causes domains in the layer.

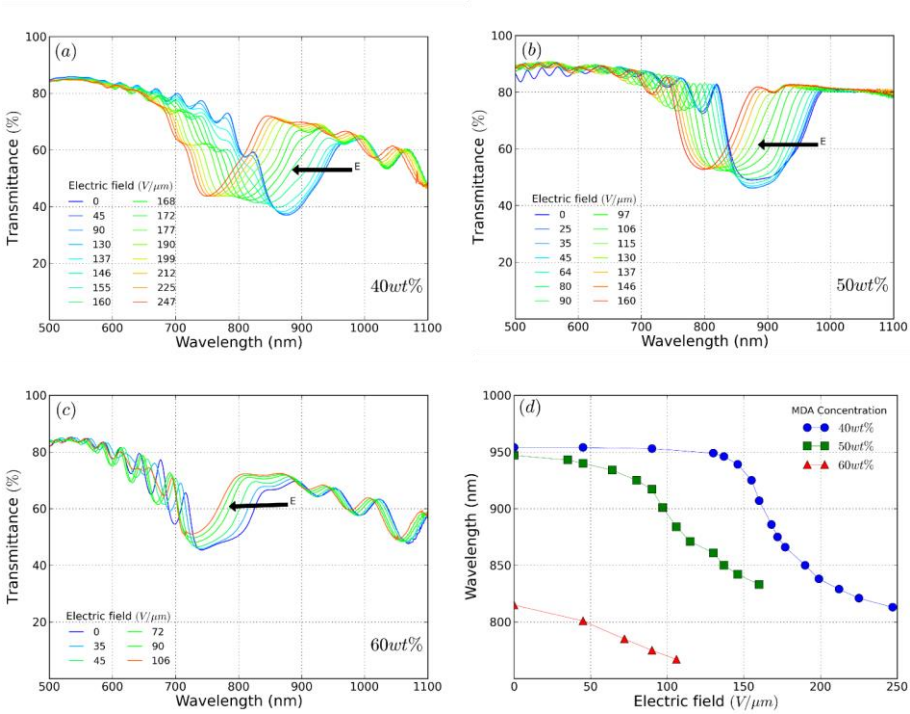


**Figure 3.1:** Transmission spectra for unpolarized light, a) 40 wt%, b) 50 wt% and c) 60 wt% MDA concentration for different applied electrical fields. d) Shift of the long band edge position of the photonic band gap as a function of the applied electric field for mixtures with 40, 50 and 60 wt% MDA concentration.

In order to rule out polarization dependencies of the spectrometer, the transmission measurements have been performed for right handed circularly polarized light, that is produced with a linear polarizer and a zero order quarter wave plate at 850 nm. The transmission spectra of 4 samples with 50 wt% MDA and 4 µm thickness in Figure 3.2 illustrate the reproducibility of the procedure.

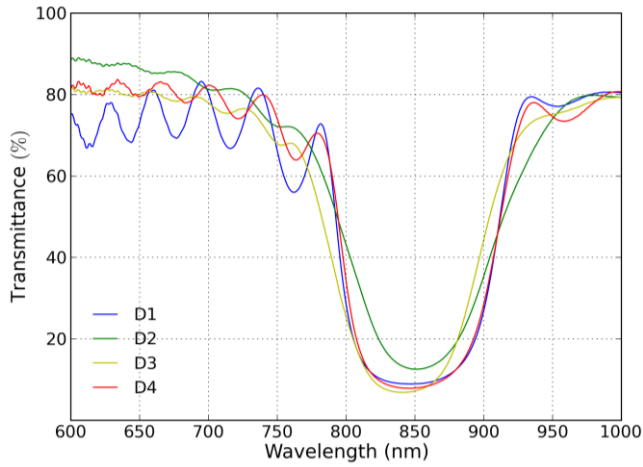


**Figure 3.2:** Transmission spectra of 4 devices with 50 wt% MDA and 4 µm thickness, for right handed circularly polarized light.

Obtaining high reflectivity and low transmittance in the bandgap is essential for an effective distributed Bragg reflector. To avoid electric breakdown for strong electric fields and to achieve low transmission in the reflection band (See section 2.1 for theoretical background), the thickness of the cells is increased to 6.75 and 8 µm. Figure 3.3 shows the transmission spectra for a thickness of 6.75 and 8 µm for right handed circularly polarized light. As a figure of merit I define the contrast ratio as the ratio between the transmission for zero Volt and for a high voltage for a certain wavelength. The contrast ratio is 16.5 and 21.5 respectively for 6.75 and 8 µm thick devices. This value is larger than the contrast ratio of 9 for the device with 4 µm thickness.

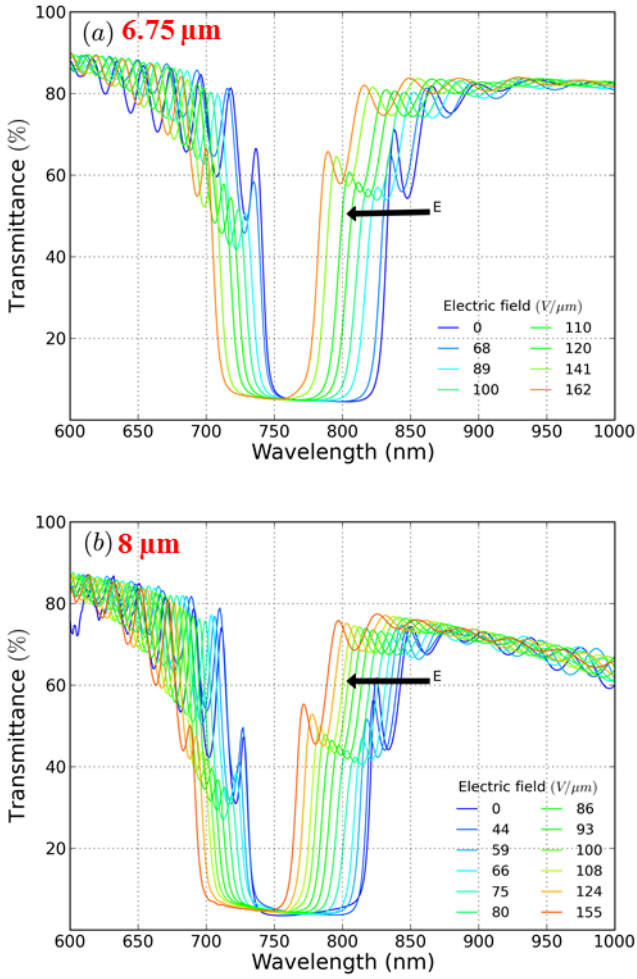


**Figure 3.3:** Transmission spectra for right handed polarized light for devices with 50 wt% MDA and and a) 6.75 µm b) 8 µm thickness, for different applied electrical fields.

The transmission in the center of the PBG is practically independent of the applied electric field and the width of the photonic band gap is only slightly reduced. This proves that the uniform helical order is maintained. The transmission in the PBG of samples with 8 µm thickness is reduced with respect to the 4 µm samples, but not as much as expected from the theoretical calculations shown in Figure 2.1b: the measured transmission in the middle of the PBG is 3.55 %, while the theoretical estimation is below 0.01%. To understand this mismatch, the Stokes parameters of the

transmitted light for linearly polarized incident light (equal amounts of RH and LH polarization) are measured for a wavelength near the center of the bandgap [77]. The Stokes parameters for samples with 4 µm and 8 µm thicknesses are shown in 0Table 3.1. $S_0$ represents the total intensity and is normalized to 1. The Stokes parameters $S_1$, $S_2$ and $S_3$ are obtained using the method described by Xie *et al*. [77]. For this approach, an optical setup (Figure 3.4) is designed to characterize the optical properties of the transmitted light from the PPCLC cell. A linearly polarized beam propagates along the *z* direction. The zero order quarter wave plate ( for a wavelength of 850 nm) with azimuth $\alpha$ and the linear polarizer with azimuth $\varphi$ are parallel to the *x-y* plane with reference 0° parallel to the x axis, which is chosen to be parallel with the first linear polarizer. Two convex lenses are used to transform the transmitted beam of the PPCLC into a parallel beam and to focus the beam onto a photo-detector. The detector is connected to a calibrated power meter.

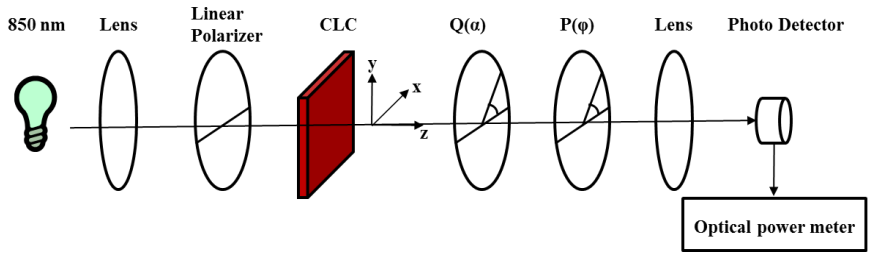


**Figure 3.4:** Optical setup to measure the Stokes parameters light passing through the PPCLC cell. Q: quarter wave plate with azimuth $\alpha$. P: linear polarizer with azimuth $\varphi$.

The transmitted intensity $P(\alpha, \varphi)$ is measured for different values of the azimuth of the quarter wave plate ($\alpha$) and the azimuth of the linear polarizer ($\varphi$). The Stokes parameter are obtained using the methods described in [78]:

$$S_1 = \frac{P(0,0) - P(90,90)}{P(0,0) + P(90,90)}$$
$$S_2 = \frac{P(45,45) - P(135,135)}{P(0,0) + P(90,90)} \qquad 3.1$$
$$S_3 = \frac{P(0,45) - P(0,135)}{P(0,0) + P(90,90)}$$

Also $S_0$ representing the total intensity is normalized to 1. The degree of polarization $\bar{p}$ follows from $\bar{p}^2 = S_1^2 + S_2^2 + S_3^2$. The ellipticity angle $\chi$ is determined from $sin2\chi = S_3/p$ and the result is 33.2° and 42.9° for the samples with 4 µm and 8 µm thickness respectively. The transmitted light for the thinner (4 µm) sample has a high degree of polarization (0.988) but the ellipticity angle deviates strongly from 45º, indicating that there is also an important transmission of right handed circularly polarized light. This is in agreement with the experiments of Figure 3.2 and the simulation of Figure 2.1b. For the thicker sample (8 µm) the transmitted light is mainly circularly polarized ($|S_3|$~p), but the degree of polarization is decreased to 0.958 which means there is an important contribution from unpolarized scattered light.

**Table 3.1:** Stokes parameters of the transmission of linearly polarized light with a wavelength near the band center.

| Thickness | 4 µm | 8 µm |
|---|---|---|
| $S_0$ | 1 | 1 |
| $S_1$ | 0.194 | 0.035 |
| $S_2$ | -0.344 | 0.045 |
| $S_3$ | -0.906 | -0.956 |
| $\bar{p}$ | 0.988 | 0.958 |
| Ellipticity angle ($\chi$) | 33.2º | 42.9º |
| Transmission minimum (%) | 6.89 | 3.55 |

Two CLC reflectors with an active region with band gap in the visible region are placed on a black sheet of paper with the word ‘Mohammad’ in white letters. Figure 3.5 shows the photographs of the devices with and without applied electric field which illustrates a blue shift of the devices. This shows that the field-tuning of the PBG keeps a high transmission for white light without scattering in the visible region which is usually not the case for polymer-CLC composites [58].

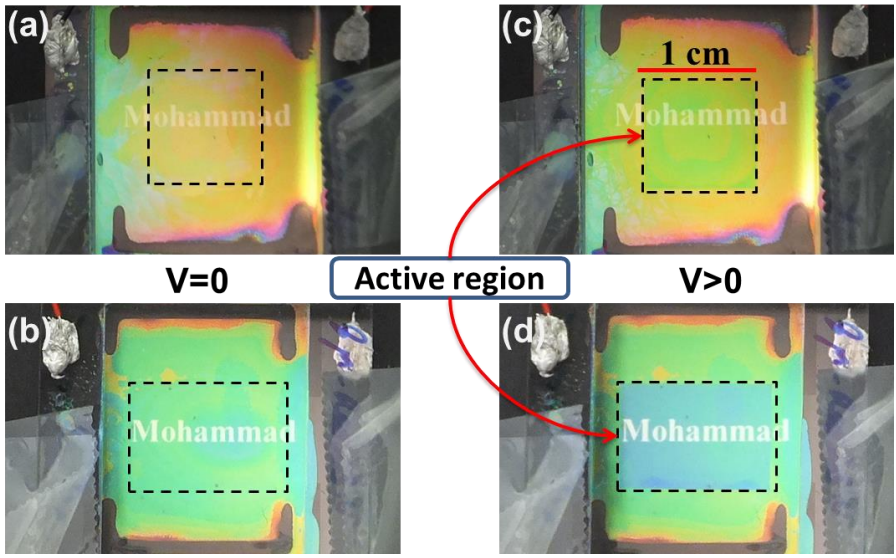


**Figure 3.5:** A macroscopic photograph of two CLC a) orange and b) green reflectors placed on a black sheet on which the word Mohammad is printed, without and c,d) with applied electric field.

To explain the blue-shift of both the right and the left band edge one has to consider the fact that light at the right band edge is traveling through the medium with an electric field vector aligned along the director of the helix. Light with a wavelength at the left band edge is traveling with an electric field vector perpendicular to the director. This explains why the right and left band edges are located at $n_eP$ and $n_oP$ respectively. The blue shift means that the refractive indices $n_e$ and $n_o$ both decrease with increasing applied voltage. Because I observe no scattering when applying voltage and because the structure is polymerized, I assume that the helix does not deform or tilt. The only possible explanation for a complete blue shift of the PBG without tilting of the helix is that the orientation of the nematic LC inside the voids is initially random as shown in Figure 3.6 a, contributing with the average refractive index $n_{avgLC}$ to the $n_e$ and the $n_o$ of the mixture. By applying an electric field, the nematic LC inside the voids becomes oriented and aligned parallel to the electric field due to the positive dielectric anisotropy of the material (Figure 3.6 b). In this case only the ordinary refractive index of the liquid crystal $n_{oLC}$ contributes and both refractive indices of the mixture decrease. As the pitch is fixed by the polymer template, and the refractive index decreases, the photonic band edges both shift to the blue and the

reflected color changes. By removing the electric field, everything returns to the original state.

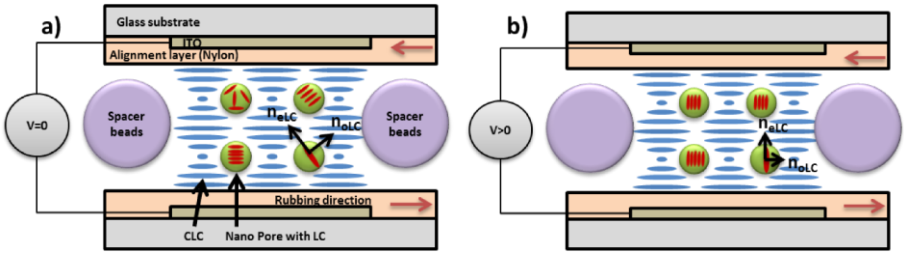


**Figure 3.6:** Scheme of the pattern with a polymerized CLC network and dispersed nano droplets with nematic LC a) without b) with applying electric field.

The response time of the device with 50 wt% MDA, 8 µm thickness and long band edge of 870 nm is measured with a microscope (Nikon, eclipse, E400 POL), 850 nm light emitting diodes for the illumination and a silicon photodiode for the detection. Figure 3.7 illustrates the switching of the liquid crystal under influence of an electric field. When the voltage is off, the transmission is low because the wavelength is inside the PBG. When applying a voltage, the nematic LC orients perpendicular to the substrates and the photonic band gap shifts to smaller wavelengths. The wavelength of 850 nm is now above the PBG and right circularly polarized light is strongly reflected. The 10–90% response times are 50 µs and 20 µs for respectively turning on and off, when switching between zero Volt and a block wave voltage signal with amplitude 150 V/µm and frequency 1 kHz. These switching times are drastically shorter than in previously reported work [56, 57, 59].

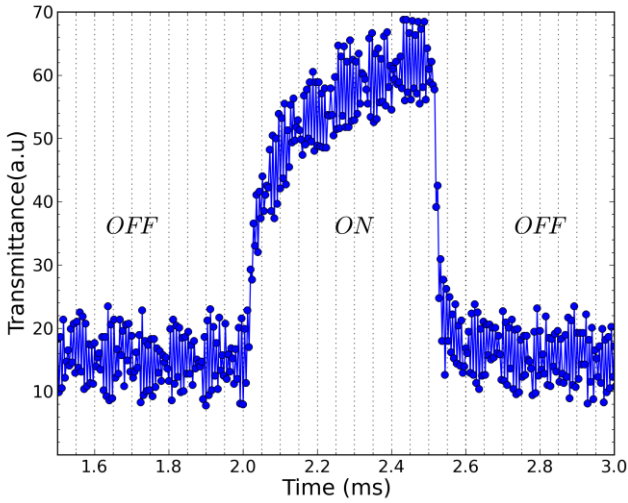


**Figure 3.7:** Electrical response of the 50 wt% MDA device with 8 µm thickness for a block wave electric field with amplitude 150 V/µm and frequency 1 kHz.

It should be noted that the device does not switch anymore for frequencies larger than 10 kHz. It is found that this is due to speed limitations of the voltage amplifier. The slew rate of the amplifier (Trek model 50/750) is 125 V/µs which limits the driving frequency. The slew rate of the amplifier also explains the fact that the switching off time is shorter than the switching on time. Considering a slew rate of 125 V/µs and an amplitude of 150V/µm for a device with 8 µm thickness, the delay time due to the amplifier is around 10 µs.

## 3.4 Effect of UV curing conditions

In this section I investigate the effects of UV illumination on the mixture that has been discussed in the previous sections. To investigate the influence of the UV power on the network structure and the photonic band gap, the mixture is infiltrated in cells with 8 µm thickness. Then the cells are exposed to various powers of UV light for 1 minute to polymerize the CLC mixture. The power of the UV light is measured by a photo detector with an active area of 1 $cm^2$. Figure 3.8 shows a scheme of the structure of the nematic LC inside a polymerized CLC network.

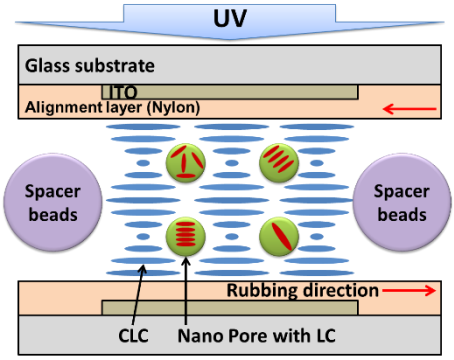


**Figure 3.8:** Scheme of the structure of a polymerized CLC network with dispersed nematic LC droplets.

After fabrication, the transmission spectra of the cells are measured by a photo spectrometer (Perkin Elmer). In order to rule out the polarization dependencies of the spectrometer, the transmission measurements have been performed for right-handed circularly-polarized light produced with a linear polarizer and a zeroth-order quarter-wave plate at 850 nm. The fabricated CLC films exhibit a broad PBG with a total bandwidth of approximately 100 nm. The PBG of the devices shift to the blue by increasing the UV power as shown in Figure 3.9a for devices illuminated from one side. Various powers of UV light are used to illuminate the cells from both sides for a duration of 1 minute. The blue shift of the PBG of the devices is shown in Figure 3.9b with increasing UV power. The strongest blue shift is 110 nm.

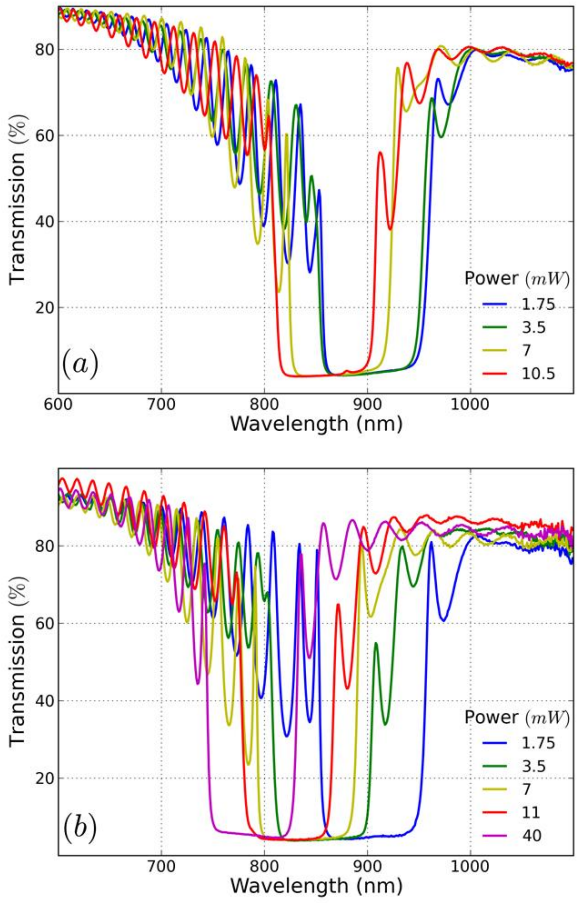


**Figure 3.9:** Transmission spectra (for right-handed circularly-polarized light) for devices exposed to various powers of UV light (365 nm) from a) one side and b) two sides

To understand the reason for the shift, the refractive indices of the cells (without chiral dopant) are estimated for 2 powers of the UV light (11 and 40 mW). The cells are illuminated from two sides for 1 minute. The spectra of the cells are measured by photo spectrometer while the c-axis of the LCs are parallel ($n_e$) and perpendicular ($n_o$) to the linear polarizer. The refractive indices around 850 nm can be estimated by using the Fabry Perot interferometer equation:

$$n \approx \frac{\lambda_1 \lambda_2}{2d(\lambda_1 - \lambda_2)} \qquad 3.1$$

Where $d$ is the thickness of the cavity and $\lambda_1$ and $\lambda_2$ are the wavelengths of the transmission maxima close to 850 nm.

The blue shift corresponds to a decrease of the refractive indices as shown in Figure 3.10.

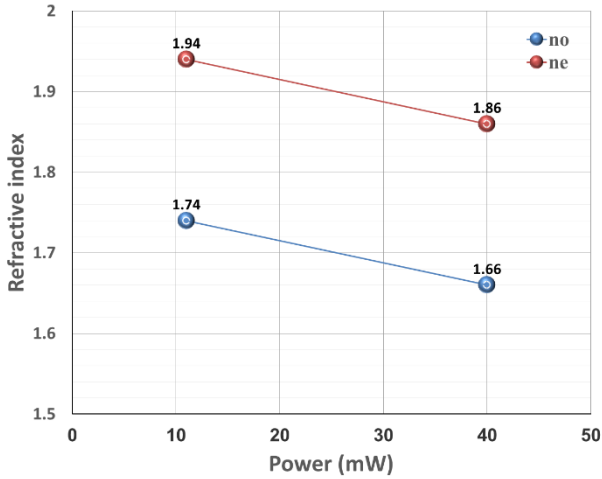


**Figure 3.10:** Ordinary and extra-ordinary refractive indices of devices exposed to two powers of UV light.

It is known that the use of photoresponsive chiral dopants results in a shift of the bandgap to longer wavelengths [3, 71]. This is due to the fact that the chiral dopant loses its chiral twisting power after absorption of UV light. In this work I use a chiral dopant which does not react to UV light. In this case the bandgap shifts to shorter wavelengths with increasing UV power, which is opposite to what would be expected from UV degradation of the chiral dopant.

To investigate the effect of duration time of UV illumination on the network structure and photonic band gap, the cells with 8 µm thickness are exposed to UV light with a power of 30 mW for 1 and 2 minutes. Figure 3.11 shows the blue shift of the PBG by applying UV light for these two durations.

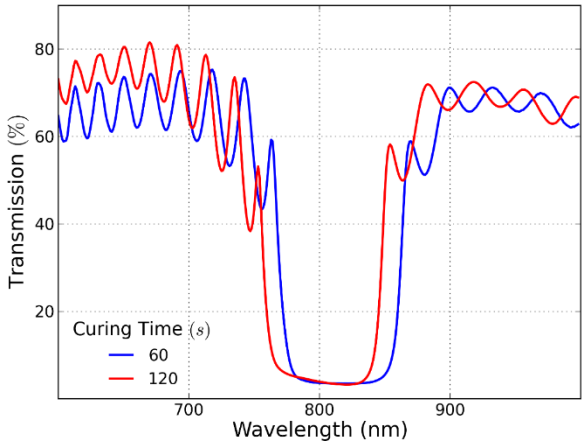


**Figure 3.11:** Transmission spectra (right handed circularly polarized light) for devices which are cured with 30 mW/cm$^2$ UV light (365 nm) during 1 and 2 minutes.

Finally I have investigated the influence of the device thickness on the network structure and photonic band gap by injecting the mixture into the cells with 4, 8 and 10 µm thicknesses. After being filled with the mixture, the cells are exposed to 30 mW/cm$^2$ UV light for 1 minute. The transmission spectra for these devices shown in Figure 3.12 demonstrate that the PBG shifts to the red in thicker devices, or equivalently that the pitch increases in thicker cells. The fact that the PBG shifts to the red with increasing thickness is most likely related to the fact that the average UV power over the thickness of the LC layer is smaller due to UV absorption. It is obvious that the transmission within the PBG decreases by increasing the thickness of the mixture [79].

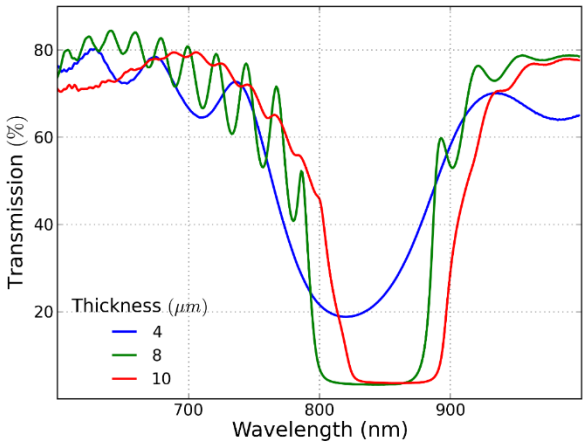


**Figure 3.12:** Transmission spectra (right-handed circularly-polarized light) for devices with various thicknesses which are illuminated by a 30 mW/cm$^2$ UV light (365 nm) for 1 minute.

## 3.5 Microsecond-range optical shutter for unpolarized light

In 3.3 I have demonstrated wavelength-tuning of the PBG of a CLC layer using an applied voltage. For many applications however it is unacceptable that the device only reflects about half of the unpolarized light. It is desirable to have a switchable photonic band gap with fast response irrespective of the polarization state of the incoming light beam.

In order to obtain switching from full reflection to full transmission in a certain wavelength range, I have used the method which is depicted in Figure 3.13. The set up includes two PPCLCs and one half wave plate. RCP light with wavelength in the PBG is reflected by PPCLC1 and the LCP light is transmitted. LCP light is converted to RCP by the zero order half wave plate centered at 850 nm. Due to the fact that this is not a broadband half wave plate, LCP light at other wavelengths will be converted into slightly elliptically polarized light. The relative retardation error for 800 nm for example is about 6% when using a 850 nm zero order waveplate. Then the RCP light is reflected by PPCLC2. This reflected light travels through the first PPCLC as it is converted to LCP. The photonic band gap is tuned by applying the same voltage signal over both PPCLCs.

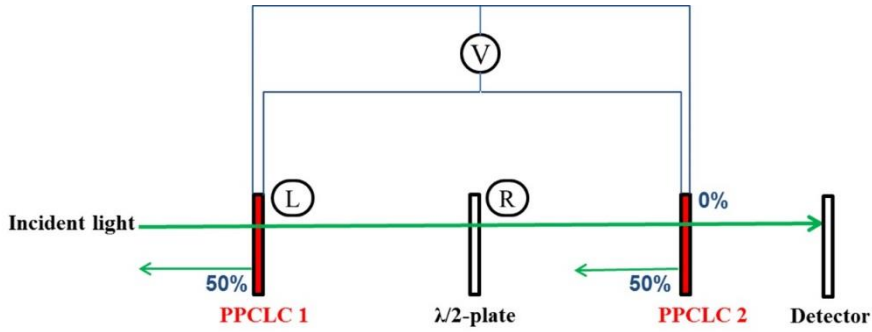


**Figure 3.13**: Schematic drawing of the device operation to modulate unpolarized incident light.

Two PPCLCs with 4 µm thickness and a central wavelength $\lambda_0$ of 850 nm are implemented separately in the setup of Figure 3.13. The cells are driven by a function generator and amplifier with a sine wave voltage (0 to 132 V/µm, 1 kHz). By applying an electric field, the nematic LC inside the voids is oriented and aligned parallel to the electric field due to the positive dielectric anisotropy of the LC. As reported in 3.3 for a single PPCLC cell, the application of a voltage results in a blue shift of the PBG. The pitch is fixed by the CLC polymer template, which means that the average refractive index seen by RCP light decreases.

The transmission spectra of the samples are measured by a dual-beam spectrophotometer (Perkin Elmer) as a function of the electric field. To avoid problems with the polarization dependency of the spectrophotometer, the measurements are performed with a linear polarizer before the device under test. Measurements are performed for different orientations of the linear polarizer. No noticeable difference is measured in the transmission spectrum when varying the angle of the linear polarizer, which means that the device works for unpolarized light. The blue shift of the PBG is shown in Figure 3.14. The device shows a blue shift of 50 nm. Instead of using the device as a wavelength tunable reflector, I believe that the most interesting application is a fast shutter for a particular wavelength. For this device I select the wavelength of 850 nm to switch between NIR and visible light and I obtain a contrast ratio (the ratio between the transmissions of a full PPCLC-λ/2-PPCLC device for zero and high electric field for specific wavelength) of 5.

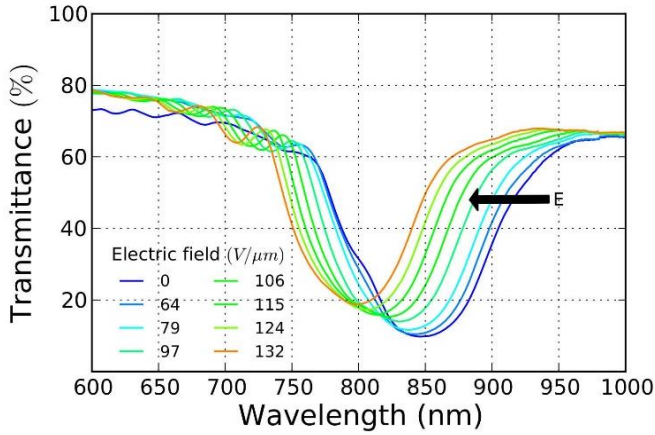


**Figure 3.14:** Transmission spectra for unpolarized light for a full PPCLC-λ/2-PPCLC device with two 4 µm thick PPCLCs for eight applied electrical fields.

To reach higher contrasts it is essential to achieve high reflectivity and low transmittance in the PBG of the PPCLC. One option is to increase the thickness of the PPCLC layers to 8 µm. Figure 3.15 shows the transmission spectra of the thicker device for unpolarized light. The contrast ratio for λ=820 nm increases to 20 while the transmission in the center of the PBG is practically independent of the applied electric field and less than 3%. The transmission in the PBG of samples with 8 µm thickness is not zero which means that there is a contribution from scattered light (See 3.3). These measurements confirm that the field-tuning of the PBG keeps the uniform helical order which is usually not the case for polymer-based CLC switches[58]. The applied electric field can be generated by commercially available amplifiers. Due to the very limited current, the power consumption is low.

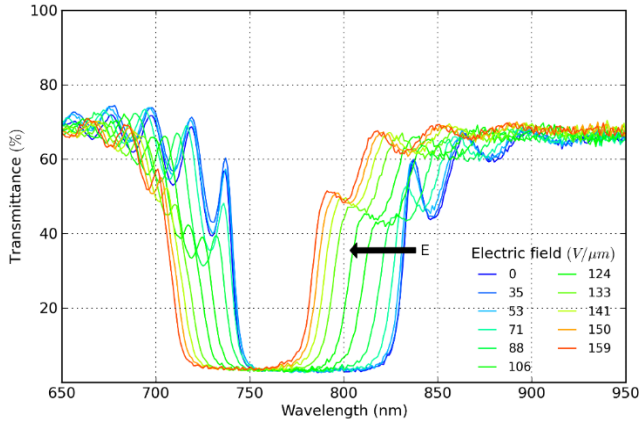


**Figure 3.15:** Transmission spectra for unpolarized light for a full PPCLC-λ/2-PPCLC device with two 8 µm thick PPCLCs for eight applied electrical fields.

The response time of the device with PPCLCs of 8 µm thickness and right band edge at 875 nm is measured with a set of light emitting diodes (850 nm wavelength, FWHM 35 nm) and a silicon photodiode for the detection. When the voltage is off, the wavelength of the light emitting diodes is inside the photonic band gap and the incident unpolarized light is strongly reflected by the device as shown in Figure 3.16. By applying an electric field, the PBG shifts to smaller wavelengths. In this state the wavelength of the light emitting diodes (850 nm) is above the PBG and the light can propagate through the device. The obtained response time is the same as for a single PPCLC. The 10–90% response time is 20 µs for switching between zero and a block wave electric field signal with amplitude 150 V/µm and frequency 2 kHz. These switching times are much shorter than in previously reported work [56, 57, 59]. The fact that the switching off time is shorter than the switching on time is due to speed limitations of the voltage amplifier. The slew rate of the amplifier (Trek model 50/750) is 125 V/µs which limits the driving frequency and response time.

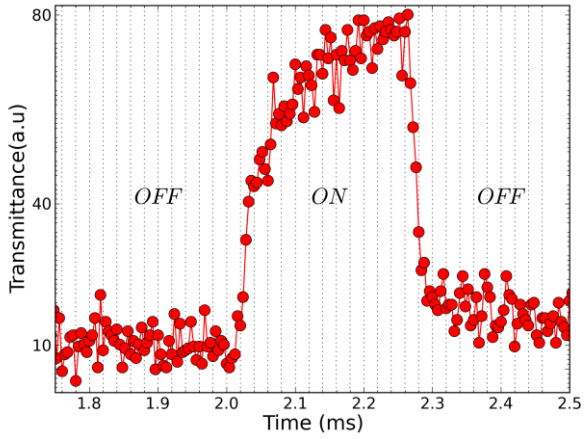


**Figure 3.16:** Switching of the transmission for light with 850 nm wavelength for a device with two PPCLCs of 8 µm thickness for a block wave electric field with amplitude 150 V/µm and frequency 2 kHz.

## Conclusion

In this chapter I have demonstrated a wide and fast shift of the photonic band gap of a mixture of photo-polymerizable LC and nematic LC including a chiral dopant assisted by applying an alternating electric field. The wavelength tuning is shown to be maximum 141 nm with relatively high stability and reflectivity and without any noticeable degradation and disruption. The response time is 50 µs and 20 µs for turning on and off an electric field, respectively.

Also I have demonstrated a wide shift of the photonic band gap for the mixture by changing the power and time duration of the UV illumination and the thickness of the cell. There is no degradation or deformation by the change in UV curing conditions. I can conclude that UV illumination plays an important role in controlling the photonic band gap of the CLC mixture. The shift is due to a decrease in the refractive indices, but the physical mechanism for this decrease is not yet clear. Further experiments are required to find out the underlying mechanism.

Finally a fast polarization-independent optical shutter with a 50 nm shift of the photonic band gap has been demonstrated. The shutter consists of two partly polymerized chiral nematic liquid crystal layers and is driven by applying an electric field. The optical response time is 20 µs and the wavelength range of the switching is 50 nm. The device shows contrast

ratios up to 20. Due to the self-assembly of chiral liquid crystal with the pitch determined by the dopant concentration, the fabrication of the switch is inexpensive and the working wavelength can be chosen.

---

"Value of a man depends upon his courage; his veracity depends upon his self-respect and his chastity depends upon his sense of honour.

Generosity is to help a deserving person without his request, and if you help him after his request, then it is either out of self-respect or to avoid rebuke".

Ali ibn Abitalib

---

# Chapter 4

# Full Alignment of Dispersed Colloidal NRs by Alternating Electric Fields

Semiconductor NRs exhibit anisotropic light absorption and light emission properties. When these NRs can be collectively aligned, they may be applied in polarized emitters, polarized fluorescent sheets or polarization-selective detectors. In this work, I demonstrate full alignment of colloidal NRs in suspension by an electric field. The absorption anisotropy of the CdSe/CdS NRs is determined for 470 nm. By comparing optical transmission measurements as a function of the electric field with theoretical simulations, the permanent and induced dipole moments of the NRs are determined. The values of the permanent dipole moment, relaxation time, absorption anisotropy and critical frequency of the CdSe/CdS dots in rods are determined. In addition, I show that the regime of full alignment enables the direct determination of the anisotropic absorption of CdSe/CdS QRs. I find that the anisotropy in absorption for the CdSe dot is similar to that of the CdS rod, which I attribute to the similarity in dielectric constant and electric field in both materials.

## 4.1 Introduction

Over the last 30 years, colloidal nanocrystals have attracted wide scientific and technological interest since their opto-electronic properties can be tuned by means of their size and shape. In particular, rod-like colloidal semiconductor nanocrystals such as CdSe quantum rods or CdSe/CdS dot-in-rods, more strongly absorb and emit light polarized parallel to their long axis [24, 25]. The ability to control the position and orientation of NRs in a device is important from scientific and technologic point of view [80-84] . Especially, as NRs exhibit anisotropic absorption, and spontaneous and stimulated emission [24, 85-87] aligning individual NRs to a preferred axis is attractive for applications in photovoltaic energy conversion, light-emitting devices ( in particular back light of LCDs), optical sensors, switches, etc. [28-32] .

Although use can be made of the anisotropic properties of single NRs [18, 26, 27], applications such as polarized light emitting diodes [28], photovoltaic energy conversion, optical sensors or switches [29-32] require layers or volumes with large ensembles of aligned NRs. In this context, various methods for the collective alignment of colloidal NRs have been explored. Focusing on colloidal quantum rods, these either exploit the tendency of NRs to self-assemble by aligning their long axes upon drying or dispersion destabilization or involve the use of external forces to impose rod alignment. Depending on the actual conditions, slow solvent evaporation on a solid substrate or a liquid subphase results in NR films aligned with their long axis parallel or perpendicular to the substrates [83, 88-92]. Alternatively, alignment by external forces has been demonstrated using mechanical rubbing of a pre-deposited film of randomly oriented quantum rods [93] or by means of electric fields applied either during solvent drying [94-96] or to achieve electrophoretic deposition [97].

Besides the alignment of NRs during deposition, a number of studies have addressed the alignment of quantum rods in solution. Various reports describe the organization of NRs in two-dimensional sheets of a single layer of parallel quantum rods by depletion attraction [98], specific surface functionalization schemes [99] or a reduction of the dispersion stability [100, 101]. Although it proved possible to orient such 2D sheets in solution by magnetic fields [102], the size of the sheets leads to considerable scattering of light and results in patchy deposits upon solvent drying. Opposite to this alignment-by-aggregation, the collective orientation or alignment of non-aggregated NRs is possible by means of an electric field. Although electrical

alignment has mainly been used to characterize NR properties such as the dipole moment [103] or the absorption anisotropy [104], it can be regarded as a technical solution to produce functional solid films with strong anisotropy in optical absorption, emission or scattering. Depending on the electrode configuration the alignment can be homogenous or follow a pattern. Alignment by an electric field is also possible for low concentrations where interactions between NRs can be avoided.

Despite the potential of in-situ alignment of NRs by electric fields, both its theoretical and experimental aspects have only been studied partially in the literature. Ruda *et al*. gave a theoretical description of the alignment of gold NRs based on the anisotropy of the induced dipole moment [105]. In the case of semiconductor NRs on the other hand, alignment by alternating electric fields is typically attributed to a permanent dipole along their long axis [94, 103, 104], although the presence of a permanent dipole could not be confirmed by electrostatic force microscopy [106]. More importantly however is that the regime of full rod alignment has not yet been reached. Using the available combination of applied fields and quantum rod dipoles, Kamal *et al*. only obtained partial orientation, as the electrostatic energy gained by orienting the rods was at best about equal to the thermal energy [104], while an even weaker orientation can be deduced from the figures provided by Li *et al*. [103].

In this chapter, I demonstrate that colloidal CdSe/CdS NRs that are dispersed in a non-polar solvent can be quasi fully aligned by applying a sufficiently strong electric field. The degree of alignment is monitored by measuring the transmission [104] as a function of time during the application of a time-dependent voltage. I review the theory for dynamic orientation of NRs, which is described by the viscosity of the liquid, the rotational diffusion, the torque due to the permanent dipole moment and the (induced) dielectric torque. In the past there have been several attempts to estimate the permanent dipole moment of CdSe NRs [103, 104]. By studying the voltage dependence of the alignment and comparing this with the theory, I am able to evaluate the magnitude of the permanent dipole moment of the NRs. From the measurements I can also estimate the absorption anisotropy, the threshold voltage and the critical frequency for alignment of the NRs.

## 4.2 Synthesis and experimental set up

### 4.2.1 Synthesis of CdSe/CdS NRs

The CdSe/CdS dot-in-rods have been synthesized by Tangi Aubert from the FCN group at Ghent University according to a procedure described in the literature (see Appendix A, paragraph 1 for synthesis details) [87].

First, CdSe quantum dots (QDs) with a wurtzite structure and an average diameter of 2.3 nm are synthesized. On these core QDs, an anisotropic CdS shell is grown using phosphonic acids as the ligands to obtain CdSe/CdS dot-in-rods with an average diameter of 4.8 nm and an average length of 51.5 nm. Finally the CdSe/CdS NRs are dispersed after purification in dodecane (1 and 10 µMolar). Figure 4.1a shows a transmission-electron-microscopy (TEM) image of the used NRs and Figure 4.1b shows a sketch of the NR structure. These particular anisotropic structures are preferred to other types of quantum rods due to their high photoluminescence quantum yield which is reported to be up to 75% [87]. The absorption spectrum of the CdSe/CdS NRs (Figure 4.1c) is taken using a Perking Elmer Lambda 950 spectrometer. Steady-state photoluminescence measurements are performed with an Edinburgh Instruments FLSP920 setup. The emission spectrum (Figure 4.1d) is recorded for an excitation wavelength of 365 nm and is corrected for the sensitivity of the detector (see Appendix A, paragraph 2 for Characterization techniques).

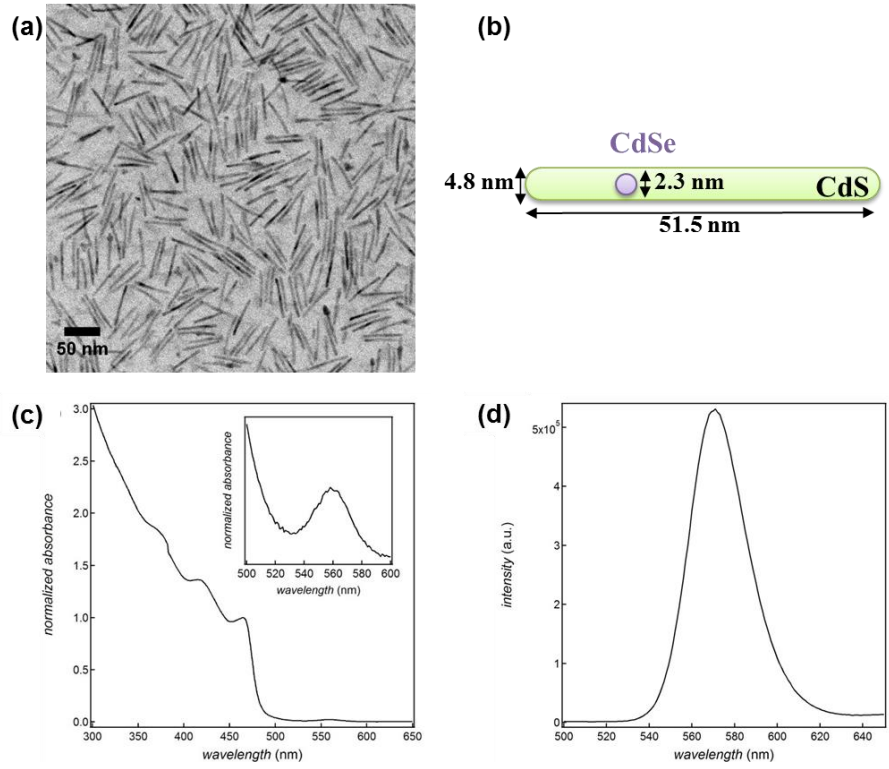


**Figure 4.1:** a) TEM micrograph of the CdSe/CdS NRs b) Sketch of the CdSe/CdS NR structure c) Absorption spectrum of the CdSe/CdS (inset: magnification for the range 500 nm to 600 nm highlighting the absorption feature of the CdSe cores) d) Emission spectrum of the CdSe/CdS NRs (excitation wavelength of 365 nm).

The optical constant (bulk value) of the CdS and CdSe with wurtzite structure at 300 *K* and the optical constant of the dodecane are listed in Table 4.1.

**Table 4.1:** Optical constant of wurtzite CdS and CdSe at 300 *K[107]*.

| Material \ Wavelength | | Static value | | 470 nm | | 560 nm | |
|---|---|---|---|---|---|---|---|
| | | $E \perp c$ | $E \parallel c$ | $E \perp c$ | $E \parallel c$ | $E \perp c$ | $E \parallel c$ |
| CdS | $n$ | 3 | 3.2 | 2.61 + 0.37i | 2.70 + 0.39i | 2.58 | 2.59 |
| | $\varepsilon$ | 8.99 | 10.21 | 6.69 + 1.95i | 7.12 + 2.18i | 6.66 | 6.72 |
| CdSe | $n$ | 3.05 | 3.19 | 2.72 + 0.45i | 2.75 + 0.48i | 2.74 + 0.39i | 2.79 + 0.39i |
| | $\varepsilon$ | 9.29 | 10.16 | 7.20 + 2.47i | 7.36 + 2.64i | 7.38 + 2.12i | 7.62 + 2.20i |
| Dodecane | $n$ | 1.42 | | | | | |
| | $\varepsilon$ | 2.01 | | | | | |

### 4.2.2 Quantum rod alignment by electric fields

Two glass substrates with 1 $cm^2$ ITO electrodes are used to make cells with 20 μm and 50 μm spacing $d$ between the electrodes. The electric field in the gap can be approximated by assuming a homogeneous field $E = V/d$, with $V$ the applied voltage. The NR suspension is filled inside the cell by capillary force. The sketch of the cell with random orientation of NRs in the off-state and aligned NRs along the electric field direction, is shown in Figure 4.2a and b respectively. The connection of the electrodes is illustrated in Figure 4.2d. A function generator (TTi-TG315) and a voltage amplifier are used to apply a high AC voltage with a frequency between 50 Hz and 40 kHz on the electrodes, resulting in electric fields up to 40 V/μm. The transmission for blue light (470 nm) and green light (580 nm) from a single color LED is measured by a photo detector (FLC electronics-PIN20) which is mounted

onto the microscope (Nikon-eclipse E400). Figure 4.2e shows part of the setup including the cell and the blue LED (The cell is shown in Figure A.2, Appendix A, paragraph 3).

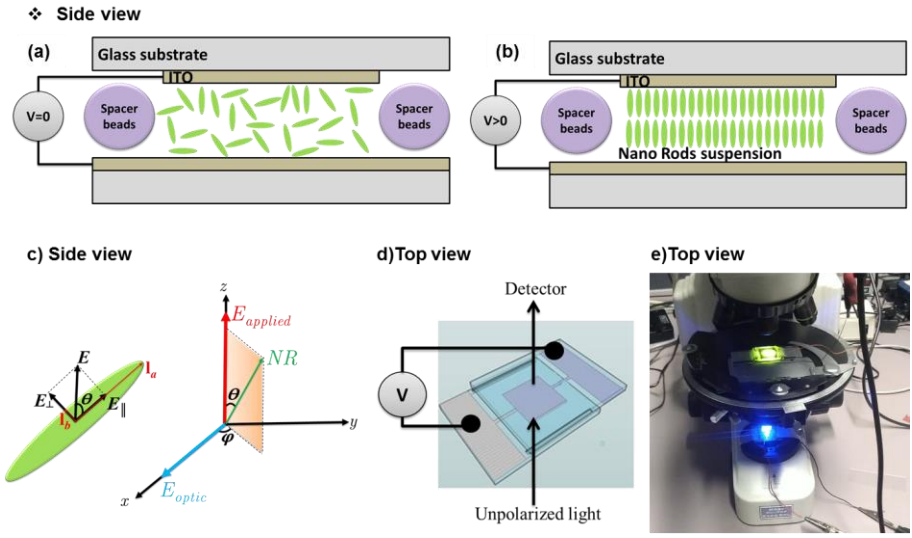


**Figure 4.2:** Orientation of NRs in suspension in dodecane: a) without and b) with applied voltage. c) The electric field is perpendicular to the ITO electrodes and $\theta$ is the angle between the electric field and the NR long axis. The components of the electric field parallel and perpendicular to the long axis $l_a$ are called $E_{\parallel}$ and $E_{\perp}$ respectively. d) Schematic view of the device and e) image of the microscope transmission setup.

## 4.3 Theoretical Background

### 4.3.1 Orientation of spheroids in an electric field

For the alignment of NRs dispersed in an apolar liquid in the presence of an electric field, the permanent and the induced (dielectric) dipole moments are considered. Semiconductor NRs have typically a higher dielectric constant than the apolar liquid and this results in an induced dipole moment that is proportional to the applied electric field. Moreover, NRs have a permanent dipole moment that is related to the non-centro-symmetric wurtzite crystal structure of semiconductors like CdSe/CdS. To derive the dynamic equation of motion for this alignment, I take into account dielectric and dipolar

torques, thermal fluctuations and rotational viscosity of the NRs suspended in the solvent.

When a NR or a spheroidal particle is placed in a host medium with dielectric constant $\varepsilon_h$ in which a homogeneous external field $E_{\text{ext}}$ is present, the induced dipole moment (with respect to the host medium) amounts to:

$$\Delta\mathbf{p} = \alpha_a \varepsilon_0 E_{ext,||} \mathbf{1}_a + \alpha_b \varepsilon_0 E_{ext,\perp} \mathbf{1}_b \tag{4.1}$$

The unit vectors ($\mathbf{1}_a$, $\mathbf{1}_b$, $\mathbf{1}_c$) are mutually orthogonal with $\mathbf{1}_a$ along the long axis of the spheroid and $\mathbf{1}_c$ perpendicular to both $\mathbf{1}_a$ and the external field. The field components $E_{||}$, $E_{\perp}$ are the projections on the unit vectors $\mathbf{1}_a$ and $\mathbf{1}_b$ as shown in Figure 4.2c. For an anisotropic spheroidal particle with dielectric constants $\varepsilon_{nr||}$, $\varepsilon_{nr\perp}$, the polarizabilities along the long and short axis are given by [108]:

$$\begin{aligned} \alpha_a &= \frac{\left(\varepsilon_{nr||} - \varepsilon_h\right)}{\varepsilon_h + L_a\left(\varepsilon_{nr||} - \varepsilon_h\right)} V \\ \alpha_b &= \frac{\left(\varepsilon_{nr\perp} - \varepsilon_h\right)}{\varepsilon_h + L_b\left(\varepsilon_{nr\perp} - \varepsilon_h\right)} V \end{aligned} \tag{4.2}$$

With $V$ the volume of the particle and $L_a$ and $L_b$ the depolarization factors for a spheroidal particle [109]:

$$\begin{aligned} L_a &= \frac{b^2}{a^2 - b^2}\left[\frac{a}{2\sqrt{a^2 - b^2}} \ln\frac{a + \sqrt{a^2 - b^2}}{a - \sqrt{a^2 - b^2}} - 1\right] \\ L_b &= \frac{1 - L_a}{2} \end{aligned} \tag{4.3}$$

With $a$ and $b$ the length of the corresponding semi-axes (see Figure 4.2c). The torque due to the excess polarization is given by:

$$\mathbf{T}_{dielectric} = \Delta\mathbf{p} \times \mathbf{E}_{ext} = \tfrac{1}{2}\left(\alpha_a - \alpha_b\right)\sin 2\theta\, \varepsilon_0 E_{ext}^2 \mathbf{1}_c \tag{4.4}$$

With $\theta$ the angle between the long axis of the spheroid and the electric field.

If the NR has a permanent dipole moment **p** along the long axis of the NR, then the external electric field yields an additional dipolar torque:

$$\mathbf{T}_{dipolar} = \mathbf{p} \times \mathbf{E}_{ext} = pE \sin\theta \mathbf{1}_c \qquad 4.5$$

Including the two torques into the dynamic equation of reorientation yields the following differential equation for the orientation angle $\theta$:

$$I \frac{d^2\theta}{dt^2} + \gamma_r \frac{d\theta}{dt} = \left(2k_B T \gamma_r\right)^{1/2} \xi(t) + pE \sin\theta + \tfrac{1}{2}\left(\alpha_a - \alpha_b\right) \sin 2\theta \varepsilon_0 E^2 \qquad 4.6$$

The first term contains the moment of inertia $I$ and is usually negligible for small spheroids, except for very high frequencies (MHz range). The second term represents the viscous torque and contains the rotational viscosity [105] $\gamma_r$ for a spheroidal particle:

$$\gamma_r = \frac{16\pi\eta\sqrt{a'^2 - b'^2}\,(a'^4 - b'^4)}{3\left[(a'^2 - b'^2/2)\ln\dfrac{a' + \sqrt{a'^2 - b'^2}}{a' - \sqrt{a'^2 - b'^2}} - a'\sqrt{a'^2 - b'^2}\right]} \qquad 4.7$$

with $\eta$ the dynamic viscosity of the medium (unit: Pa.s) and $a$' and $b$' the semi-axes of the prolate ellipsoid NR, which include the length of the ligands (2 nm). The first term on the right hand side is the torque due to Brownian interaction [110], with $k_B$ the constant of Boltzmann.

I can estimate the typical time $\tau_{on}$ to align a spheroid when switching on a sufficiently strong electric field, by neglecting the Brownian term in equation 4.6, replacing the derivative by the ratio $\Delta\theta/\tau_{on}$, and setting $\Delta\theta = \theta = \pi/4$:

$$\tau_{on} \simeq \frac{\pi\gamma_r}{2\sqrt{2}pE + 2\left(\alpha_a - \alpha_b\right)\varepsilon_0 E^2} \qquad 4.8$$
$$f_{on} \simeq 1/\left(2\pi\tau_{on}\right)$$

The typical time for reorientation when switching off the voltage is called the relaxation time, which is usually longer than $\tau_{on}$. This time and the relaxation frequency and can be estimated using the Debye-Perrin model[111] and equation 4.6:

$$\tau_{relaxation} \simeq \frac{\gamma_r}{k_B T}$$
$$f_{relaxation} \simeq \frac{k_B T}{2\pi\gamma_r} \qquad 4.9$$

The excess electrostatic energy of a spheroid in an electric field is given by:

$$U_{el} = -p_0 E_{ext}\cos\theta - \tfrac{1}{2}\left(\alpha_b \varepsilon_0 E_{ext}^2 + (\alpha_a - \alpha_b)\varepsilon_0 \cos^2\theta E_{ext}^2\right) \qquad 4.10$$

In the quasi-static case, when the frequency of the field is well below $f_{\text{relaxation}}$ (and also below $f_{on}$), the probability $P(\theta)$ to find a spheroid in a given solid angle $d\Omega$ is determined by the Boltzmann distribution for the momentary electric field:

$$P(\theta) \propto \exp\left(-\frac{U_{el}}{kT}\right) \qquad 4.11$$

### 4.3.2 Absorbance of dispersed spheroidal particles

When an absorbing spheroidal particle is dispersed in a non-absorbing solvent, the effective absorption coefficient for light depends on the orientation of the particle. Based on the depolarization factors parallel and perpendicular to the long axis of the spheroid, I can write down the intrinsic absorption coefficients based on the model in [112] :

$$\mu_{\parallel} = \frac{2\pi\varepsilon_{nr,I}}{n_h\lambda}\left|\frac{n_h^2}{n_h^2 + L_a\left(\varepsilon_{nr,R} + i\varepsilon_{nr,I} - n_h^2\right)}\right|^2$$
$$\mu_{\perp} = \frac{2\pi\varepsilon_{nr,I}}{n_h\lambda}\left|\frac{n_h^2}{n_h^2 + L_b\left(\varepsilon_{nr,R} + i\varepsilon_{nr,I} - n_h^2\right)}\right|^2 \qquad 4.12$$

In this expression $n_h$ is the refractive index of the host solvent and $\varepsilon_{nr,R} + i\,\varepsilon_{nr,I}$ is the NR complex dielectric constant for the considered wavelength. In

the typical situation for semiconductor NRs in an apolar solvent, $\varepsilon_{nrR}$ is larger than $\varepsilon_h$. For a prolate spheroid $L_a$ is smaller than $L_b$ and the absorption coefficient for parallel orientation is larger. For a spheroid with inclination $\theta$ and azimuth $\varphi$ as shown in Figure 4.2c the absorption coefficient is an average of the parallel and perpendicular components, weighted by the square of the projection of the electric field:

$$\mu(\theta,\varphi) = \mu_{||}\cos^2\varphi\sin^2\theta + \mu_{\perp}(1-\cos^2\varphi\sin^2\theta) \tag{4.13}$$

For an ensemble of spheroids the absorption coefficient $\mu$ in equation 4.13 has to be averaged over all orientations of the long axis of the NRs, weighted with the corresponding Boltzmann factor (4.11):

$$\mu = \frac{\int_0^{2\pi}\int_0^{\pi} P(\theta)\mu(\theta,\varphi)\sin\theta d\theta d\varphi}{\int_0^{2\pi}\int_0^{\pi} P(\theta)\sin\theta d\theta d\varphi} \tag{4.14}$$

The absorbance $A$ of a spheroid dispersion is given by the intrinsic absorption coefficient $\mu$ [23] multiplied with the volume fraction $f$ of the spheroids and the thickness of the dispersion, divided by the natural logarithm of 10:

$$A = \mu\frac{f\,d}{\ln 10} \tag{4.15}$$

## 4.4 Results and discussion

### 4.4.1 Full Alignment of Colloidal NRs by Electric Fields

To explore the full alignment of dispersed colloidal NRs by electric fields, a dodecane-based dispersion of CdSe/CdS NRs is loaded in a cell as described in 4.2.2. As a fraction of NRs will carry an electric charge,[113] application of a DC field will make the NRs drift to the electrodes. To avoid artefacts

due to NR accumulation at the electrodes, I use AC fields with a period shorter than the cell transit time $\tau_r = d / uE$ where $u$ is the mobility of the NRs which is equal to the charge of the NR over the translational friction coefficient. If we consider one unit charge per NR, the mobility in dodecane is estimated as $5.8*10^{-10}$ $m^2/V.s$. NRs in a 50 µm cell have a cell transit time of ≈ 5ms for fields of 17 V/µm. Therefore, I use frequencies higher than 200 Hz to study NR alignment.

A first measurement involves the optical transmission of a 50 µm cell filled with a 1 µM dispersion of NRs in dodecane at 470 nm in the presence of a sinusoidal AC electric field. An example is given in Figure 4.3, where it can be seen that the two extreme values of the electric field during a single period both correspond to a maximum increase of the transmission (more results are provided in the Appendix A, paragraph 4).

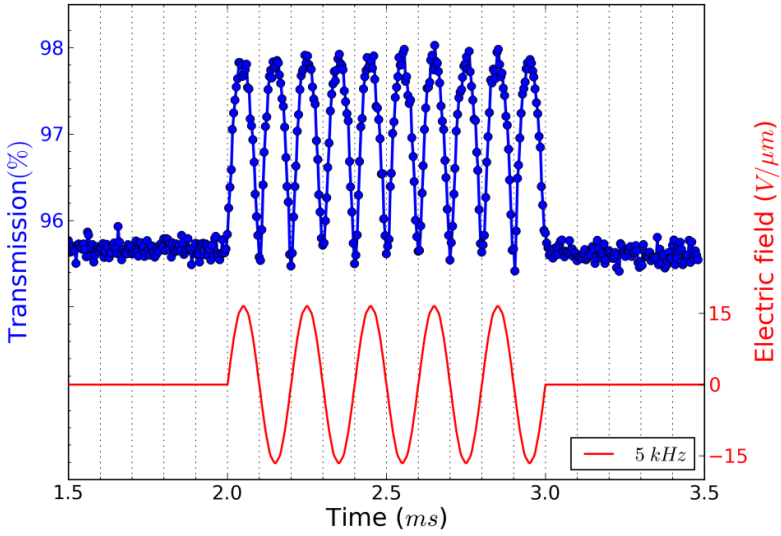


**Figure 4.3:** Transmission measurements (blue dots) of a CdSe/CdS NR suspension for blue light (~470 nm) with and without the presence of an AC electric field with a frequency of 5 kHz and an amplitude of 17 V/µm (red line).

From these transmission measurements, the absorbance $A$ by the NR dispersion is calculated as:

$$A = -\log \frac{I_T}{I_0} \qquad 4.16$$

Here, $I_0$ is the light intensity passing through the cell loaded with dodecane only, while $I_T$ is the (possible time dependent) intensity transmitted through the NR-loaded cell. One readily sees that the increased transmission upon application of an electric field corresponds to a drop of the absorbance. This is in agreement with NRs aligning their long axes parallel to the AC electric field and perpendicular to the electric field of the incident light, where the absorbance drop is due to the higher depolarization factor for fields along the short axis of the CdSe/CdS NRs ($L_b$ = 0.49 instead of $L_a$ = 0.018).

In order to eliminate the trivial influence of cell thickness and NR concentration from the measurements, I introduce the relative change of the absorbance $\Delta A/A_0$ (usually <0):

$$\frac{\Delta A}{A_0} = \frac{A - A_0}{A_0} \qquad 4.17$$

Here, $A_0$ is the absorbance of the NR-loaded cell in the absence of an electric field. Figure 4.4 represents the variation of the minimum of $\Delta A/A_0$ as a function of the applied electric field.

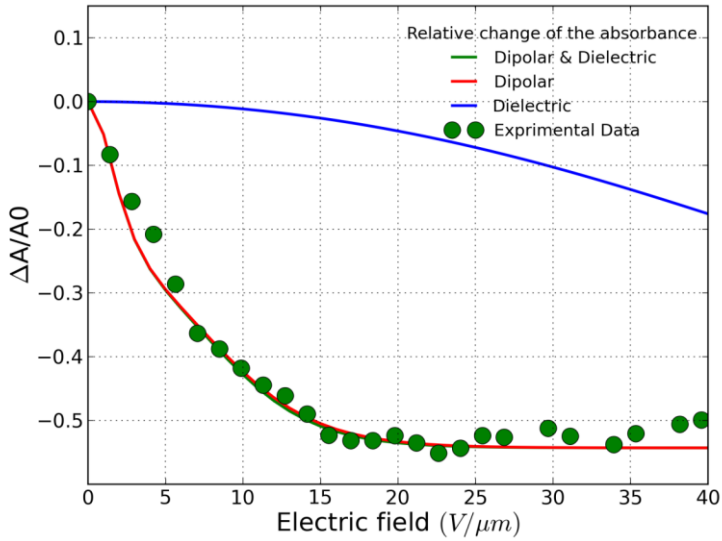


**Figure 4.4:** Minimum value of the relative change of the absorbance of the 1 µMolar NR dispersion in the presence of an AC electric field with a frequency of 1 kHz as a function of peak value of the electric field. Measurements (green dots) and simulations assuming only dielectric torque (blue), only dipolar torque (red) and both dielectric and dipolar torques (green, almost identical to red).

One sees that while increasing the electric field initially leads to a more pronounced drop of the absorbance, $\Delta A/A_0$ levels off at ≈ -0.54 for fields exceeding 15 V/µm. This levelling-off is also apparent from the variation of $\Delta A/A_0$ over a single period of the AC field. When applying for example a 1 kHz field with a maximum amplitude of 17 V/µm, *i.e.*, close to the field strength for which the time-averaged absorption change saturates, Figure 4.5 shows how $\Delta A/A_0$ hits a plateau each time the field is around its extreme values. I attribute this behaviour to the NRs being fully aligned along the direction of the electric field such that any additional increase of the field strength cannot further reduce the absorbance.

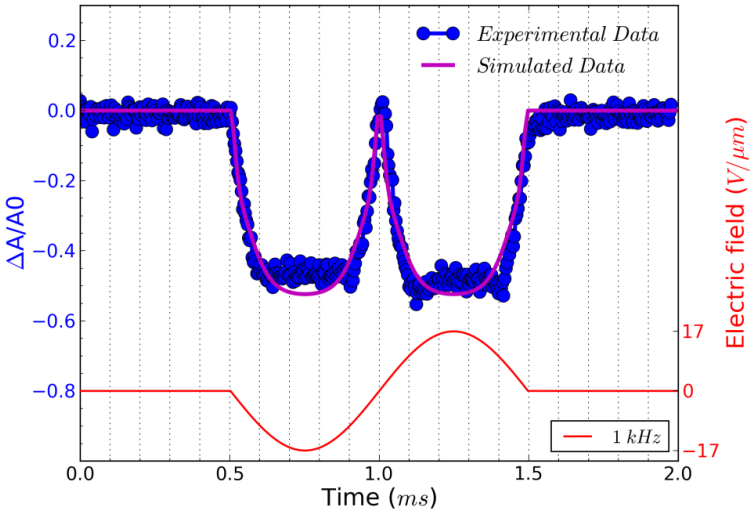


**Figure 4.5:** Relative change of the measured (blue dots) and simulated (magenta) absorbance of the 1 µMolar NR dispersion for blue (~470 nm) light in the presence of an AC electric field with frequency 1 kHz and amplitude 17 V/µm (red).

### 4.4.2 Dynamical Properties of Colloidal NR Alignment

Next to the levelling off of the absorbance change, Figure 4.5 also makes clear that the change in absorbance is established without noticeable delay. This indicates that at the fields and frequencies used, the NRs readily flip from a θ=0° to a θ=180° orientation when the field changes direction (see Figure 4.2c for a definition of the angle $\theta$). Hence, the NR reorientation occurs on a time scale much shorter than the 1 ms period of the AC field, an outcome in line with the dynamical properties of NR (re)orientation. Indeed,

using eqs 4.7 and 4.9, the rotational relaxation frequency $f_{rel}$ in dodecane of the CdSe/CdS NRs used here can be estimated at 13 kHz. Hence, fields with a frequency well below 13 kHz, should give the NRs enough time to establish a quasi-equilibrium Boltzmann distribution that follows the variation of the electric field, thus bringing them from random orientation to full alignment. In line with this, increasing the AC frequency from 1 to 10 kHz only changes the frequency at which the transmission changes, without affecting the limiting value corresponding to full alignment as shown in Figure 4.6. Hence, the only difference between a 1 and a 10 kHz field is that the latter makes the QRs flip faster between the θ=0° to a θ=180° orientation. At frequencies above $f_{rel}$, the distribution will not return to random alignment and the minimum in the transmission will not be as low as the zero-field transmission, whereas the NRs will stop reacting on the AC field once the frequency is higher than the turn on frequency $f_{on}$, which is estimated at ≈100 kHz in this case.

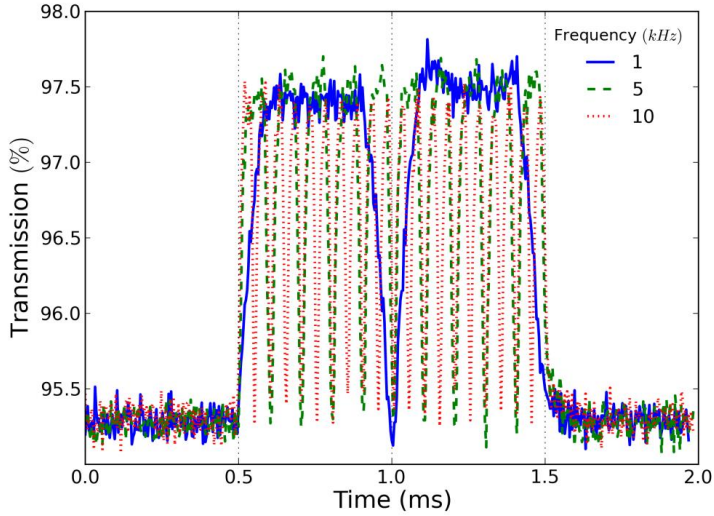


**Figure 4.6:** Transmission of a cell (thickness 50 µm) with CdSe/CdS suspension when an AC electric field is applied with amplitude 17 V/µm and various frequencies.

This description of the NR orientation dynamics is further confirmed by the response of the transmission to a single block pulse with an amplitude of 17 V/µm. As shown in Figure 4.7, the regimes of full alignment and de-alignment are reached within less than 50 µs.

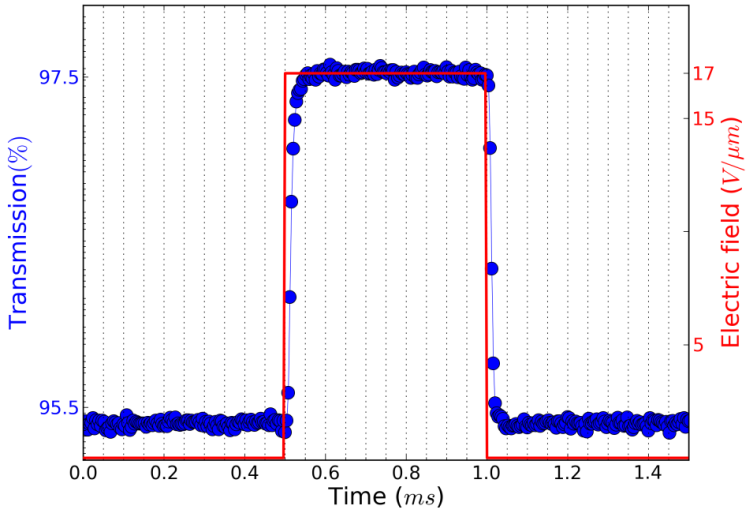


**Figure 4.7:** Transmission versus time of a CdSe/CdS NR suspension in dodecane when a pulse with amplitude of 17 V/µm is applied.

### 4.4.3 Permanent *versus* Induced Dipole Moments

As the absorbance of the CdSe/CdS NRs at 470 nm will be dominated by the CdS rod (Figure 4.1c), the bulk optical constants of CdS can be used to estimate the dielectric function of the quantum rod in the expressions for the polarizability and the absorption coefficient of dielectric ellipsoids, i.e., eq 4.2 and 4.14 respectively. The thus calculated polarizability and absorption coefficients at 470 nm have been summarized in Table 4.2. Using these figures, the degree of orientation and the concomitant relative absorbance change can be calculated if only the dielectric torque were present. The thus predicted dependence of $\Delta A/A_0$ on the electric field strength has been added to Figure 4.4, where it follows that fields of more than 40 V/µm would be needed to obtain an appreciable alignment of the NRs. I therefore conclude that the (full) alignment of the NRs is indeed due to the permanent dipole moment of the NRs.

Considering the NR dipole moment $p$ as an adjustable parameter, the field dependence of $\Delta A/A_0$ can again be predicted. Figure 4.4 shows that taking $p$=1500 D ($5*10^{-27}$ C.m), a typical value for the CdSe/CdS NRs used here, makes the simulated field dependency of $\Delta A/A_0$ all but match the experimental data. I stress that this predicted trend depends on a single adjustable parameter, i.e., the dipole moment $p$, which mainly determines the

region of electric fields where the NRs change from random to full alignment. The high-field limit of $\Delta A/A_0$ on the other hand only depends on the difference in absorption coefficient of fully aligned ($\mu_\perp$) and randomly aligned ($\mu_0$) quantum rods:

$$\lim_{E\to\infty} \frac{\Delta A}{A_0} = \frac{\mu_\perp - \mu_0}{\mu_0} \qquad 4.18$$

Inserting the estimated absorption coefficients (see Table 4.2), a limit of -0.54 is indeed obtained, in line with the experimental findings.

A number of interesting values for NRs obtained from experimental and simulation results are listed in Table 4.2.

**Table 4.2:** Obtained experimental results for CdSe/CdS NRs.

| Nanorod dimensions | Ellipsoid with axes: 51.5 nm; 4.8 nm; 4.8 nm | |
|---|---|---|
| Depolarization factor | $L_\parallel = 0.018$ | $L_\perp = 0.49$ |
| Field inside CdSe ( $E_{ext} = 20V/\mu m$) | $E\ (E_{ext} \parallel c) = 18.16$ | $E\ (E_{ext} \perp c) = 8.95$ |
| Field inside CdS ( $E_{ext} = 20V/\mu m$) | $E\ (E_{ext} \parallel c) = 19.21$ | $E\ (E_{ext} \perp c) = 9.44$ |
| Dielectric polarizibity | $\alpha_\parallel = 2.4*10^{-24}\ m^3$ | $\alpha_\perp = 0.8*10^{-24}\ m^3$ |
| Absorption coefficient for 470 nm | $\mu_\parallel = 1.8*10^{7}\ m^{-1}$ | $\mu_\perp = 0.4*10^{7}\ m^{-1}$ |
| Relaxation time of NRs in dodecane | 12 µs | |
| Relaxation frequency of NRs in dodecane | 13 kHz | |
| Typical time to align ($\tau_{on}$) | 1.6 µs | |
| Turn on frequency ($f_{on}$) | 100 kHz | |
| Fitted permanent dipole moment | 1500 Debye | |
| Estimated induced dipole moment at 17 V/µm | 100 Debye | |

### 4.4.4 Absorption Anisotropy at the Band-Edge Transition

As indicated by eq 18, the regime of full alignment provides a way to directly determine the absorption anisotropy of colloidal NRs at a given wavelength. I therefore extended the analysis to the NR absorbance at the CdSe/CdS first exciton transition at around 560 nm (see Figure 4.1c), which is due to electronic transitions between quantized states in the CdSe core. To adjust for the absorbance difference at 470 and 560 nm of the CdSe/CdS NRs, I had to analyze QR dispersions with a concentration 10 times higher than used for the previous measurements. Hence, I now measure the transmission of green light (≈560 nm) through a 50 µm thick cell filled with a 10 µM QR dispersions in the presence of an AC electric field (17 V/µm, 1 kHz). Figure 4.8 shows that the AC field leads to a similarly oscillating increased transmission – meaning a decrease in absorbance – as observed before at 470 nm. Hence, also the CdSe core transitions exhibit a marked absorption anisotropy.

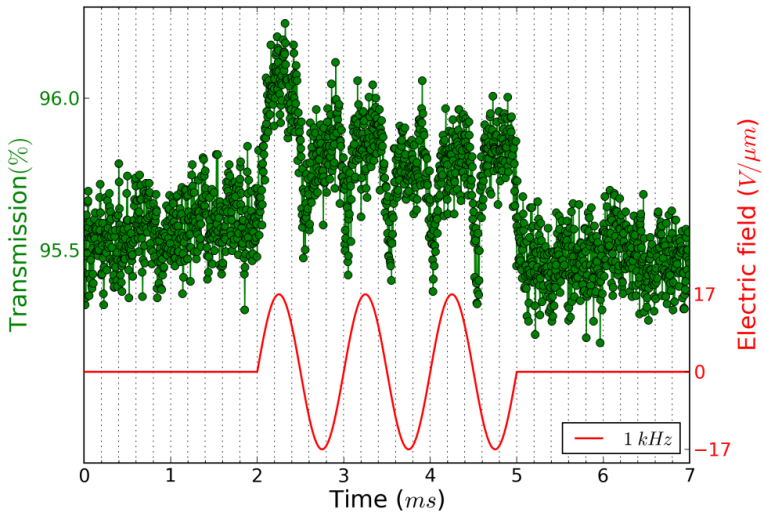


**Figure 4.8:** Transmission measurement (green dots) of a NR suspension for green (~560 nm) light in the presence of an AC electric field with frequency 1 kHz and amplitude 17 V/µm (red).

An issue with the more concentrated dispersions used here is that a considerable fraction of the NRs form aggregates that are not oriented by the applied electric field. Figure 4.9 therefore compares the relative change of the absorbance determined at 560 nm with that determined at 470 nm for the

same dispersion under the same conditions of the applied field. Since this transmission change would reach -0.54 if all rods were aligned, the actual plateau value can be used to estimate the fraction of NRs that can be aligned and thus calibrate the transmission changes at 560 nm. Figure 4.9 shows that this calibration is actually quite straightforward since the high-field limit of $\Delta A/A_0$ at 560 nm due to CdSe core absorption is very similar to the one measured at 470 nm, which is due to absorption in the CdS rod. Hence, a quite similar corrected limiting value of $\Delta A/A_0$ in the ranged -0.5 to -0.55 is obtained at the band-gap transition as well.

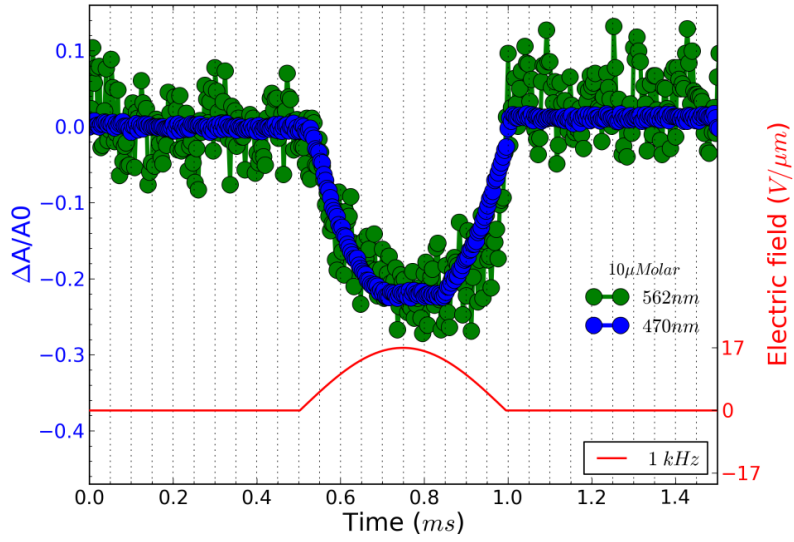


**Figure 4.9:** Relative change of the measured absorbance of the 10 µMolar NR dispersion for blue light (blue dots) and green light (green dots) in the presence of an AC electric field with frequency 1 kHz and amplitude 17 V/µm (red).

This result may seem surprising since the core is a spherically symmetric object, yet it can be understood by realizing that the dielectric mismatch between the CdSe core and the CdS shell is small. Figure 4.10 shows the electric field distribution for a CdSe sphere inside a CdS ellipsoid in dodecane, obtained from a 3D finite element field calculation (Comsol), based on the real parts of the anisotropic bulk dielectric functions for these materials at 560 nm (see Table 4.1). The internal field in the CdSe core amounts to ≈ 95% of the field in the CdS host, independent from the fact that the applied field is parallel or perpendicular to the c-axis of the rod. The electric field in the rod (and the sphere) is almost identical to the external

electric field when the applied field is parallel to the c-axis of the rod. When the applied field is perpendicular to the c-axis of the rod, the field in the rod (and dot) is only about half of the applied external field. This is expected, because the depolarization factor in the perpendicular case is larger ($L_{\perp}$=0.49).

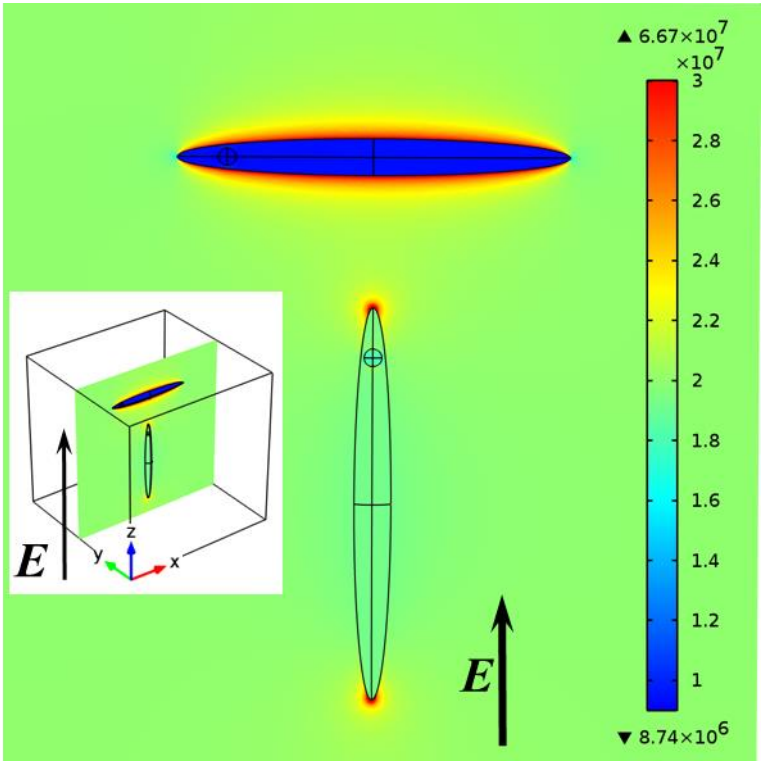


**Figure 4.10:** Simulation of the field distribution inside a dot in rod using the bulk dielectric function for incident light parallel and perpendicular to the c-axis of the rod at 560 nm (Inset: 3D structure shows the position of the NRs in the medium).

The simulation illustrates that the CdSe core experiences the same enhanced or reduced screening of the field as the CdS rod for incident optical fields perpendicular to or parallel with the long axis of the NR. Hence the largely similar absorption anisotropy for the quantum dot band gap transition.

Note that the experimentally determined high-field limit of $\Delta A/A_0$ corresponds to a polarization ratio of 60-65% for the emission [96], which is similar to the experimentally determined values of up to 75% as determined on single CdSe/CdS QRs [24].

## 4.5 Conclusion

I have shown that colloidal CdSe/CdS NRs can be fully aligned in a colloidal dispersion by the application of AC electric fields with an appropriate field strength. The alignment is monitored by measuring the variation of the transmission concurring with the oscillation of the electric field at wavelengths where the CdS rod absorption dominates. For the rods used, complete alignment parallel with the electric field is obtained for field strengths exceeding 15 V/μm and switching back and forth to random orientation occurs within 50 μs. I develop a theoretical description of the relation between the electric field and the alignment of dielectric ellipsoidal nano-objects, considering both a permanent and an induced dipole moment. Doing so, it follows that the experimentally determined alignment as a function of field strength can be attributed to the interaction between the NR permanent dipole and the applied AC field.

Since the transmission change in the regime of full alignment only depends on the difference between the NR absorption coefficient for optical fields parallel and perpendicular to the NR long axis, transmission measurements during AC driven full alignment provide an excellent method to measure anisotropic absorption by NRs. Excellent agreement between experiment and theory is obtained for the absorption anisotropy at 470 nm, i.e., wavelengths where the rod absorption dominates. Moreover, I find that band-edge transition exhibits a quite similar absorption anisotropy, a result we attribute to the small dielectric mismatch between the CdSe core and the CdS rod.

---

"Spend properly and do not be the treasurer of others. If you cry over what has gone out of your hands then also cry for what has not at all come to you. Infer about what has not yet happened from what has already happened, because occurrences are ever similar".

Ali ibn Abitalib's commandment for His Son

---

# Chapter 5

# Anisotropic light emitters based on aligned NRs

Semiconductor NRs mainly absorb and emit light which is polarized with the electric field along the long axis of the rods, it is therefore important to collectively align the long axes of NRs along a preferred direction. In this chapter, I present four methods for the homogeneous deposition and alignment of NRs from a colloidal suspension. The deposition, orientation, and polarized fluorescence of the NRs is verified by AFM and polarized fluorescence microscopy. Main results of this chapter are already published in [6] and [8].

## 5.1 Introduction

The ability to control the position and orientation of NRs in a device is important from a scientific and technologic point of view [80-84]. The homogeneous deposition of aligned NRs on large substrates is interesting for large size applications such as solar cells and OLEDs. Moreover, semiconductor nanoparticles can be used to efficiently transform blue light from GaN-based LEDs into for example green or red light, which is also needed for color displays. The combination of blue, green and red light is desired for backlights in liquid crystal displays. Nowadays liquid crystal displays have a limited transmission, on the order of 10% [114]. This is mainly due to the absorbing polarizers and color filters. In a conventional backlight the emitted light is unpolarized because it originates from LEDs or phosphor materials. Because an LCD is designed to work with polarized light [114], the polarizer typically absorbs half of the light.

Light emission is usually the result of a dipole transition in an atom, molecule or quantum dot. Recently the development of red and green quantum dots has improved the color saturation of LCDs [115]. Anisotropic emitters can have characteristics that are close to that of a dipole antenna. If the emitters are aligned parallel to the electric field of the light that is transmitted by the polarizer, most of the light that is emitted will pass the polarizer and contribute to the emission of the LCD display as shown in Figure 5.1.

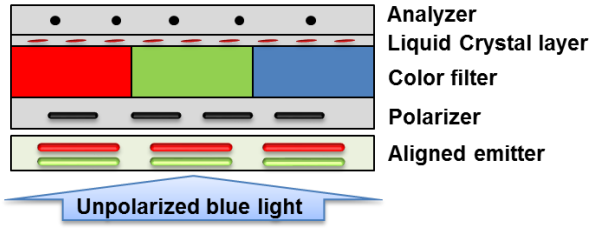


**Figure 5.1:** Scheme of polarized LC backlight

As liquid crystal devices modulate the transmission of polarized light, it would be an advantage to start from a backlight that is able to emit polarized green and red light.

Several techniques for aligning NRs have been explored such as: rod solubility in a binary solvent/non-solvent mixture [83], coffee stain evaporation dynamics [32, 89, 116], radial fluid flow with spin coating &

drying lyotropic phase [80, 117], slow solvent evaporation at a liquid-solid-air interface [28, 81], Langmuir-Blodgett deposition [84], wet-chemical attachment of NRs & epitaxial growth [118], mechanical rubbing of rods[93] or external electric fields [119]. Among them, electric-field-driven deposition from colloidal suspensions has proven to be an efficient method for the controlled positioning and alignment of all kinds of anisotropic particles such as nanowires [120] carbon nanotubes [121], gold NRs [119, 122] and semiconductor [30, 87, 123-127] NRs. In these papers, good alignment is obtained, but the methods are not compatible with cheap, reproducible and homogeneous deposition on large substrates as required for large size applications such as solar cells or OLEDs.

In contrast to the previously cited works, I use an AC field with high amplitude in which the alignment is considerable. The theory, simulation and full alignment of NRs in apolar solvents has already been treated in chapter 4.

Using such strong AC fields Ahmed *et al*. [122] already reported an effective alignment of gold NRs by drying a drop of a colloidal NRs suspension on a silicon wafer with platinum electrodes. Similarly, Hu et al. achieved effective CdSe and CdTe NR alignment on $Si_3N_4$ membranes with electrodes through slow drying in $N_2$ atmosphere of a colloidal solution drop while applying a strong DC electric field, directly inside a small atomic force microscope chamber [124]. In these two papers good alignment is obtained, but the methods are based on the casting of single drops and subsequent drying of the solvent, which is not compatible with reproducible and homogeneous deposition on large substrates as required for large size applications such as solar cells or OLEDs. In this chapter, I propose four novel techniques to homogeneously deposit aligned CdSe/CdS NRs in a solid layer:

1. Deposition of aligned NRs by dip-coating
2. Aligned NRs in a reactive liquid crystal
3. Aligned NRs in polymer
4. Aligned NRs in polymeric nanofibers

## 5.2 Deposition of aligned NRs by dip-coating

In this section, I present a novel technique for the homogeneous deposition and strong alignment of CdSe/CdS NRs on a glass substrate patterned with transparent indium tin oxide (ITO) interdigitated electrodes with a spacing of a few micrometers. This fast and versatile method is based on applying an electric field over the electrodes during the dip-coating procedure and is compatible with large-scale processing on cheap and transparent substrates. The accumulation, alignment, and polarized fluorescence of the NRs as a function of the electrical field are investigated. An alignment with order parameter of 0.92 and a polarization ratio of 0.60 is obtained with this method.

### 5.2.1 Fabrication

The CdSe/CdS NRs are synthesized according to a procedure described in Appendix A, paragraph 1. The CdSe/CdS NRs are dispersed in chloroform and the solution is filtered with a 0.2 μm PTFE syringe filter. Absorption and emission spectrum of the CdSe/CdS NRs are shown in Figure 4.1.

Standard optical lithography is used to pattern a 30 nm thick ITO layer on a glass substrate. The ITO electrodes in different designs have an interdigitated finger pattern, with each line 2600 μm long and 6 μm wide, with a gap of 4 or 6 μm (see Figure 5.2b). For comparison, each substrate has a second electrode finger pattern which is not connected to the voltage source during deposition. The experimental setup and pattern are schematically shown in Figure 5.2a and b.

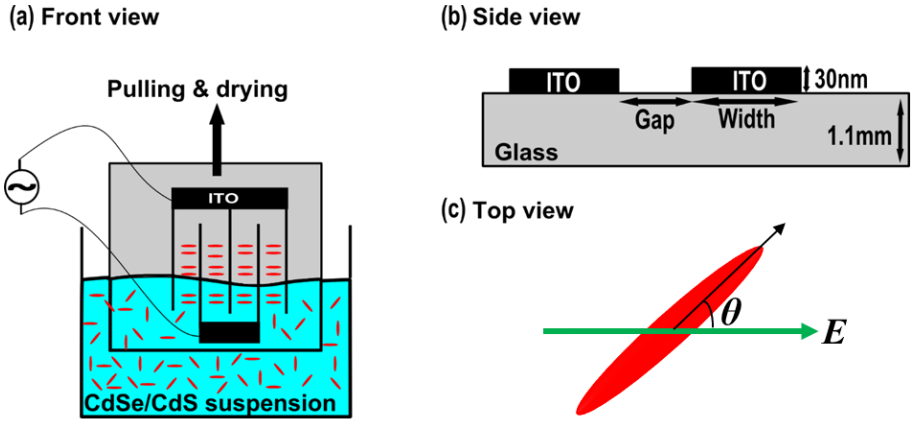


**Figure 5.2:** a) A sketch of the experimental setup: a glass substrate with interdigitated ITO electrodes is pulled out of a colloid suspension in the presence of an electric field. (b) The width of the ITO electrodes is 6 μm and the gap is 4 or 6 μm (not to scale). (c) The electric field is perpendicular to the ITO lines, and θ is the angle between the electric field and the NR long axis.

The electric field in the gap can be approximated by assuming a homogeneous field $E = V/G$, with $V$ the applied voltage and $G$ the size of the gap. Figure 5.3 shows the electric field distribution of the medium between the electrodes obtained from a 2D finite element field calculation (obtained with Comsol) based on the dielectric functions for chloroform. The electric field is almost homogeneous between the electrodes and is higher close to the corners of the electrodes.

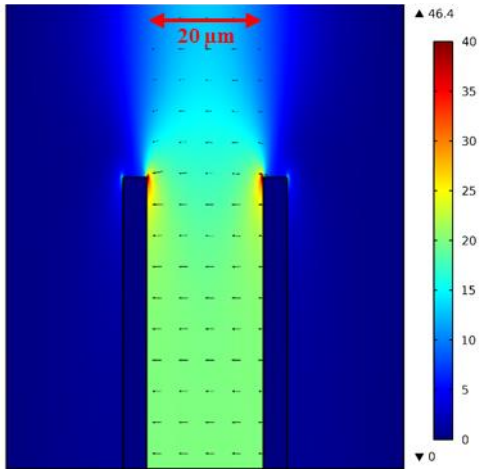


**Figure 5.3:** Simulation of the field distribution (V/µm) in the gap between the electrodes based on the dielectric functions.

A function generator (TTi-TG315) and a voltage amplifier (FLC electronics-A800X) are used to apply an AC voltage on electrodes with gaps of 6 µm or 4 µm respectively, to 2×2.6 mm pixel, resulting in an electric field. The deposition is realized by immersing vertically the substrate in a 10 nM NRs solution. The AC voltage is applied and the substrate is then pulled out completely at a speed of 85.7 mm/minute. After the chloroform has dried (in a few seconds), the voltage is switched off.

### 5.2.2 Results and discussion

After deposition, the layer is imaged with a fluorescence microscope (Nikon-eclipse Ti). The NRs are excited by the UV band (330-380 nm) of a Xenon lamp. The NR emission is detected by an Andor CCD camera after passing through a dichroic mirror, a long wavelength pass filter and a linear polarizer. The cut-off wavelength for the dichroic mirror is 400 nm and for the long pass filter is 420 nm. Figure 5.4 shows a scheme of the filter block and transmission spectra of the filters and mirror inside the block.

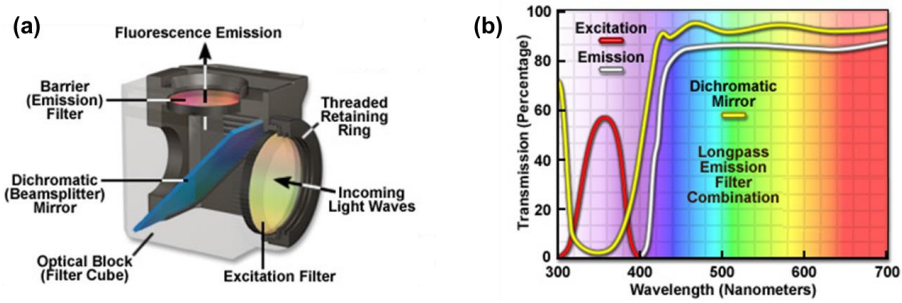


**Figure 5.4:** a) Ultraviolet Excitation Filter block consisting of an excitation filter, a dichroic mirror and emission filter. b) Transmission spectra of the dichroic mirror (yellow), excitation filter (red) and emission filter (white). The figure is from Nikon Company.

The fluorescence microscopy images in Figure 5.5 are for the substrate with ITO in absence (Figure 5.5a) and presence (Figure 5.5b) of an electric field of 17.7 V/µm, 50 kHz during dip coating. In Figure 5.5a there are (practically) no deposited NRs, the moderate brightness of the gap region is due to a weak fluorescence of the glass, whereas ITO absorbs UV light. Figure 5.5b shows that NRs are not deposited on the electrodes and that when the electric field is present, many NRs are deposited inside the gap. The comparison between Figure 5.5a and b indicates that the NRs are attracted by the strong electric field near the surface of the substrate between the electrodes, which is well known for high-dielectric particles in an electric field gradient. The distribution of the NRs inside the gap is also observed in atomic-force microscopy (AFM) (Figure 5.5c). Both techniques reveal a higher density of rods near the center of the gap.

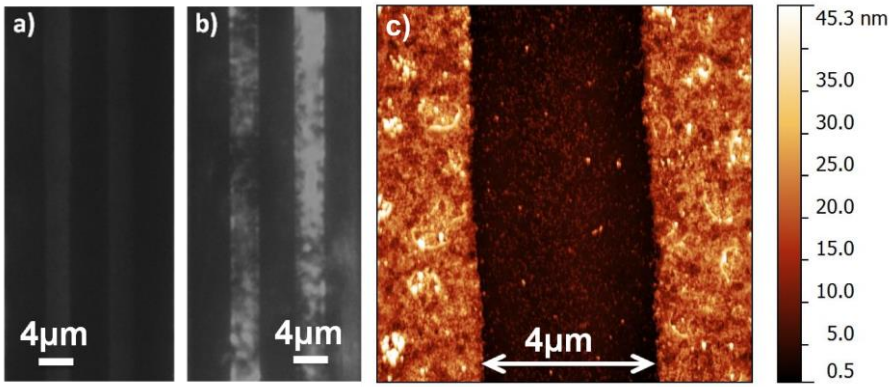


**Figure 5.5:** Fluorescence microscopy images of a substrate (electrode gap of 4 µm indicated by white line) after dip-coating in absence (a) or presence (b) of an electric field, and AFM image of the same substrate in presence of an electric field (c).

Based on the theoretical framework of the full alignment regime of the NRs in chapter 4, I can calculate the required electric field to align the NRs in chloroform. The orientation of the NRs for the substrate in presence of an electric field of 20 V/µm, 1 kHz during dip coating, is investigated in detail by AFM. Figure 5.6a shows a preferential horizontal alignment of the NRs.

In order to analyze the orientation of NRs from the image in an objective way, the image data is analyzed by a computer program. In a first step, the image is subjected to a threshold to obtain a black and white image. In the second step, white regions that are surrounded by black pixels are identified. To avoid the analysis of NR clusters and small noise related regions a maximum and minimum area for the white regions is set. Only the white regions with an area within the defined interval are ascribed to individual NRs and are represented in Figure 5.6b. The white regions are then fitted to ellipses and the azimuth angles $\theta$ of the long axes are determined. Figure 5.6c finally show the histogram of the azimuth angles $\theta$ for the selected NRs. The angle of the NRs is mostly between -10° to 10°, evidencing a clear preferential horizontal alignment (i.e. perpendicularly to the electrodes).

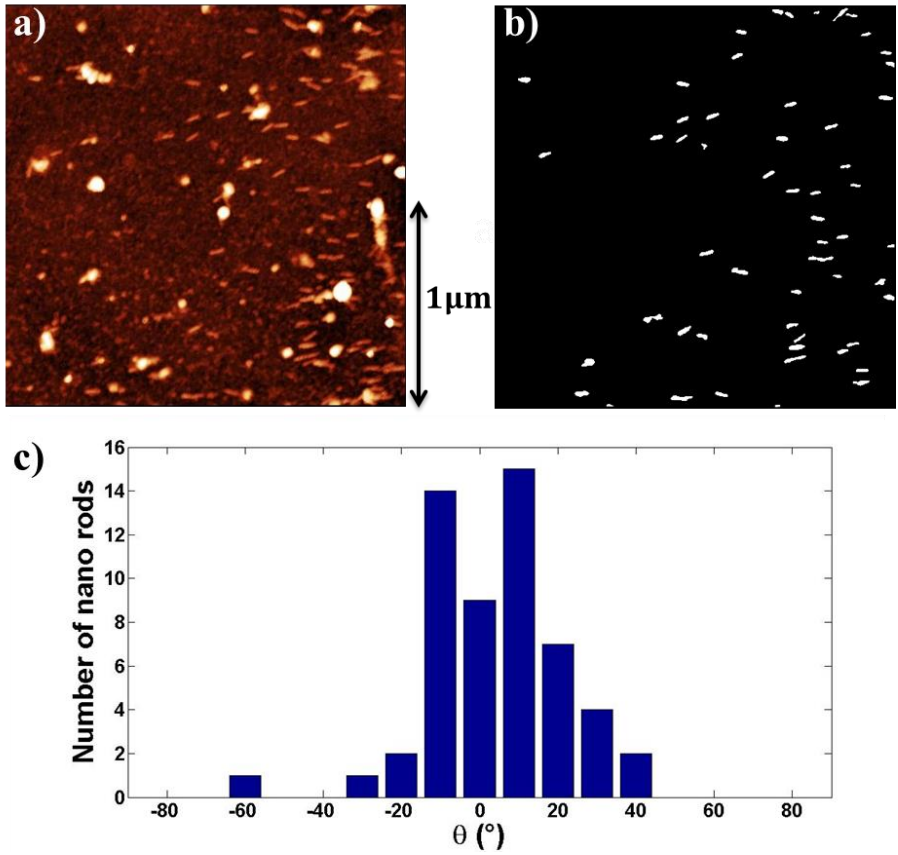


**Figure 5.6 :** a) AFM image of aligned NRs between the electrodes deposited in the presence of an alternating electric field with frequency 1 kHz and amplitude 20 V/µm. b) Processed images to identify individual NRs c) Histogram of the azimuth angles of the NRs in the image.

To quantify the degree of NR alignment in the images, I use the orientation order parameter $\mathcal{S}$, which is defined as:

$$\mathcal{S} = \langle 2\cos^2\theta - 1 \rangle \qquad 5.1$$

With $\theta$ the angle between the NR long axis of an individual NR and the average direction of the long axes of all NRs. This expression accounts for the two-dimensional nature of the NR alignment and yields $S = 1$ in the case of perfect alignment and $S = 0$ in the case of random orientation [122, 124].

The obtained *S* is 0.92 for the NRs deposited in Figure 5.7. The orientation of the NRs depending on the deposition condition (11.8 V/µm or 17.7 V/µm) is investigated in detail by AFM (Figure 5.7). Both Figure 5.7 a and b show a preferential horizontal alignment of the NRs in the cases $E$ = 11.8 V/µm and $E$ = 17.7 V/µm. The individual NRs are represented in Figure 5.7 c and d and the corresponding histograms of the azimuth angles $\theta$ for the selected NRs are indicated in Figure 5.7 e and f.

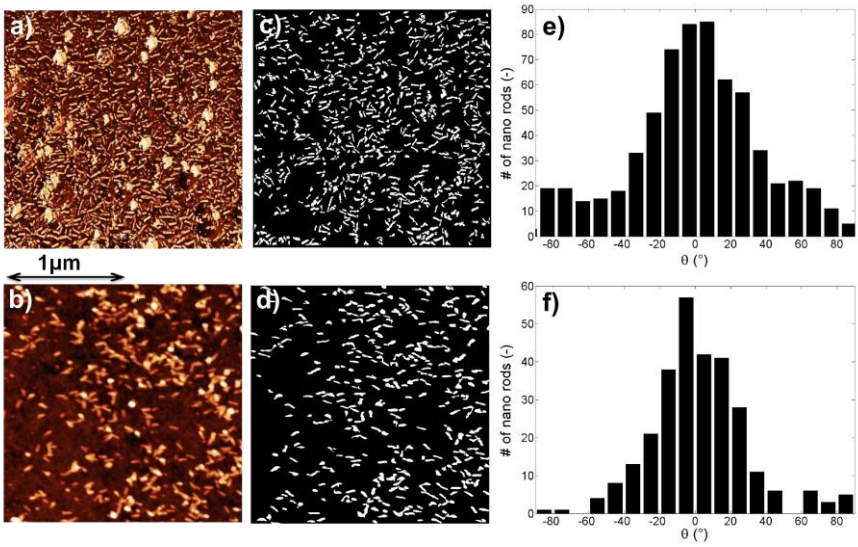


**Figure 5.7 :** AFM images of aligned NRs between the electrodes (a) deposited with an AC field of 11.8 V/µm (1 kHz) and (b) deposited with an AC field of 17.7 V/µm (50kHz). (c,d) Processed images to identify individual NRs. (e,f) Histograms of the azimuth angles of the NRs in images c and d.

The obtained order parameter *S* is 0.67 for the NRs deposited in the stronger electric field at higher frequency (Figure 5.7 b) and 0.45 for the NRs deposited in the weaker field at lower frequency (Figure 5.7 a).

To observe the anisotropic emission of the deposited NRs, the sample with the highest obtained order parameter is imaged with a fluorescence microscope. The fluorescence intensity is collected by an objective (60x), passes through a rotatable linear polarizer and is detected by an Andor CCD camera as shown in Figure 5.8a. One should note that in our experiments the excitation light is not polarized. This is preferred in order to avoid preferential absorption by the NRs that have the best alignment and allow for a better assessment of the true polarization ratio of the sample.

Figure 5.8b shows the emission of the NRs while the polarizer is oriented perpendicularly (left) or parallel (right) to the line electrodes. The strongest photoluminescence is observed when the polarizer is parallel to the alignment of the NRs ($\theta$ = 0). This is in agreement with earlier polarization measurements on individual NRs [85] and aligned NR arrays [24, 32, 87].

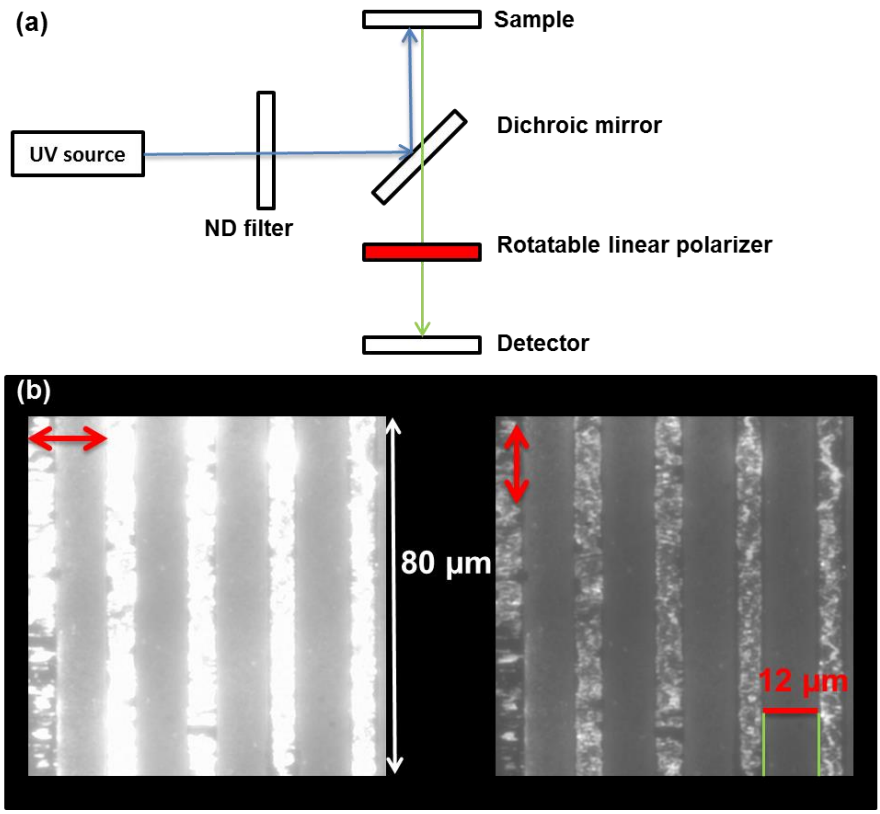


**Figure 5.8:** Fluorescence microscopy a) set up and b) images of a substrate (electrode width of 12 µm as indicated by a scale bar) after dip-coating while the polarizer is oriented perpendicular (left) and parallel (right) to the line electrodes.

Figure 5.9a shows the fluorescence images of the NRs for different orientations of the polarizer. The average intensity *I* of the fluorescence is obtained by averaging the grey scale values over the pixels within a selected region in the image. Figure 5.9b shows the parameter *I* as a function of the

orientation of the polarizer which corresponds to a function $I_{\perp} + \left(I_{\parallel} - I_{\perp}\right)\cos^2\theta$. The polarization ratio is expressed as [32]:

$$\prod_r = \left(I_{\parallel} - I_{\perp}\right) / \left(I_{\parallel} + I_{\perp}\right) \qquad 5.2$$

From Figure 5.9b I find that the polarization ratio is 0.6. One should keep in mind that the polarization ratio of a single CdSe/CdS NR with a spherical core is limited to 75%, so that a polarization ratio of 100% cannot be achieved [128-130]. The fact that I find a smaller may be attributed to several factors: a limited degree of alignment, loss of polarization due to scattering or unpolarized emission from aggregates. It may also be due to the fact that the transition dipole moment of the NRs considered here is not perfectly aligned with the NR long axis [96]. I verified that the fluorescence from regions with randomly oriented NRs yields a vanishing polarization ratio.

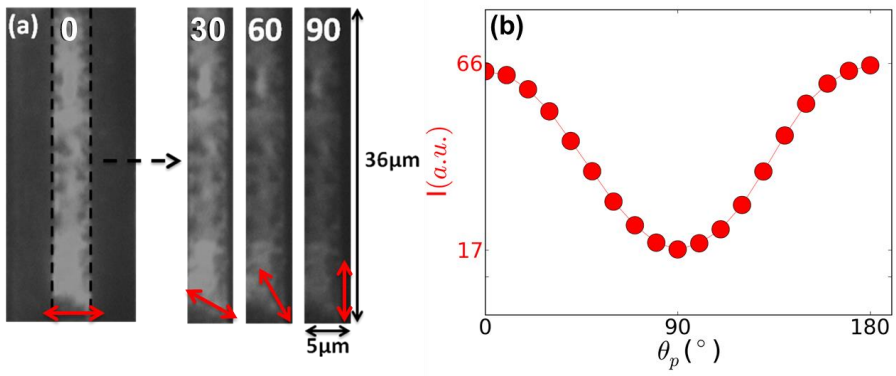


**Figure 5.9:** a) Fluorescence microscopy images of the NRs located in the gap between two electrodes (dashed lines), for four azimuthal orientations of the polarizer. b) Variation of the integrated fluorescence intensity of the NRs in the same region as a function of the azimuth of the polarizer ($\theta_p$).

I can conclude the dip coating deposition method is fast, facile, and can be applied on relatively large substrates. In addition, I believe that this method can be extended to the deposition or printing of most of aligned anisotropic particles. An alignment with order parameter 0.92 and a polarization ratio of 0.60 is obtained with this method.

## 5.3 Alignment of NRs suspension in liquid crystal

### 5.3.1 Introduction

In the previous section, I presented a novel technique for the homogeneous deposition and efficient alignment of CdSe/CdS NRs on a glass substrate which is based on applying an electric field over the electrodes during a dip-coating procedure [96, 131]. But aligning the NRs with this method requires high electric fields up to 20 V/μm and this can be an issue for roll to roll fabrication.

On the other hand, liquid crystals exhibit unique properties such as long-range orientational order and anisotropic optical and electronic properties in a certain temperature range while keeping the fluidic properties. The self-organizing nature of these liquid crystals has been demonstrated in different configurations [132, 133] and introduced in chapter 1. These self-organizing properties of anisotropic liquid crystals can aid in the alignment of anisotropic objects such as nanowires, nanotubes [134] and both metal [135] and semiconductor NRs. Hybridization of two different material systems may lead to novel materials with interesting properties and resulting device applications. One of the technical challenges is to homogeneously disperse nanoparticles in anisotropic fluids without aggregation of the nanoparticles in the medium in sufficiently high concentrations to be useful for applications. The use of surfactant stabilization is a common method applied to reduce clustering as e.g. for the case of gold NRs in lyotropic LC [135-137].

In this section, I propose a novel technique to homogeneously disperse and align CdSe/CdS NRs in a polymer film. The fabrication uses a glass substrate with transparent interdigitated indium tin oxide electrodes. This method is based on doping the reactive nematic liquid crystal with NRs and consequently aligning the mixture by an electric field.

In the next subsections, the electric field strength required to align the semiconductor NRs is determined experimentally. Application of high electric field yields a reduction of clustering NRs in LC medium. The relaxation times and critical frequencies of the semiconductor NRs are estimated by the experimental results.

### 5.3.2 Thin film aligned NRs in reactive LC

#### 5.3.2.1 Mixture of NR and LC Synthesis

The CdSe/CdS NRs are synthesized according to a procedure described in Appendix A, paragraph 1. Absorption and emission spectra and TEM images of the CdSe/CdS NRs are already shown in section 5.24.2. After purification, the CdSe/CdS NRs are dispersed in chloroform and a mixture of reactive nematic liquid crystal. This mixture is prepared by mixing a photo initiator (Irgacure 819, BASF) with a blend of different reactive mono- and di-acrylate mesogens (Merck) and a inhibitor (tert-Butylhydroquinone, Sigma-Aldrich). A NR suspension in LC at a concentration of 1 w% is obtained by evaporating the chloroform.

#### 5.3.2.2 Fabrication

Two glass substrates with interdigitated ITO electrodes are used to make a liquid crystal device with 10 μm spacing between the substrates. The thickness, length and width of the ITO electrodes are 30 nm, 2600 μm and 4 μm respectively and the gap between two electrodes is 20 μm. The experimental setup and ITO pattern are schematically shown in Figure 5.10 a and b. A function generator (TTi-TG315) and a voltage amplifier (FLC electronics-A800X) are used to apply an AC electric field over the gaps between the electrodes. The deposition is realized by infiltrating a 1wt% NR suspension of the LC mixture into the device. An electric field (20 V/μm, 1 kHz) is applied and after an interval of a few seconds, the device is illuminated with 30 $mW/cm^2$ UV light during one minute in order to photopolymerize the reactive LC mixture. After polymerization, the voltage is switched off.

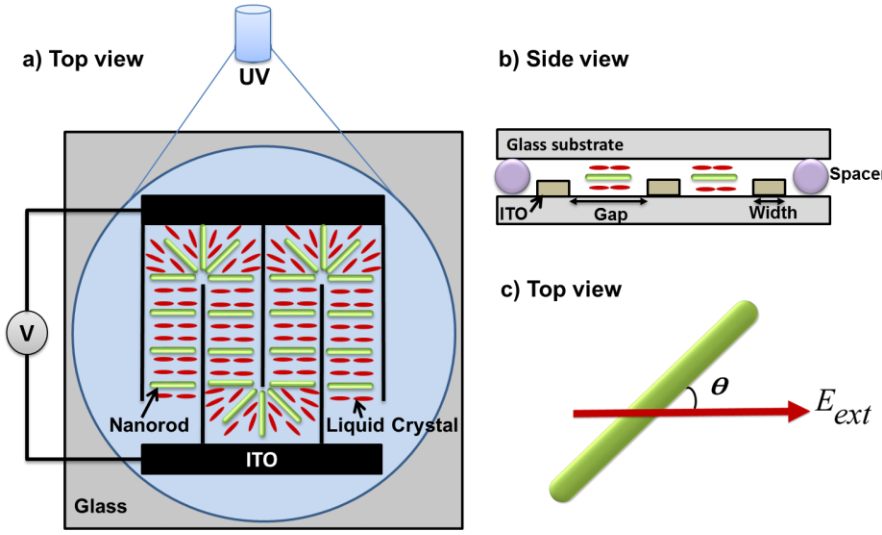


**Figure 5.10:** a) A sketch of the experimental setup: a device with two parallel glass substrates with interdigitated ITO electrodes on one of the substrates, is filled with a NR suspension in a reactive liquid crystal and illuminated by UV light in the presence of an electric field. b) The width of the ITO electrodes is 4 μm and the gap is 20 μm (not to scale). c) $\theta$ is defined as the angle between the electric field and the NR long axis.

Finally, both two glass substrates can be removed and the free-standing polymer layer remains. Figure 5.11 shows a flexible thin film aligned NRs that is excited by UV lamp and emit polarized light.

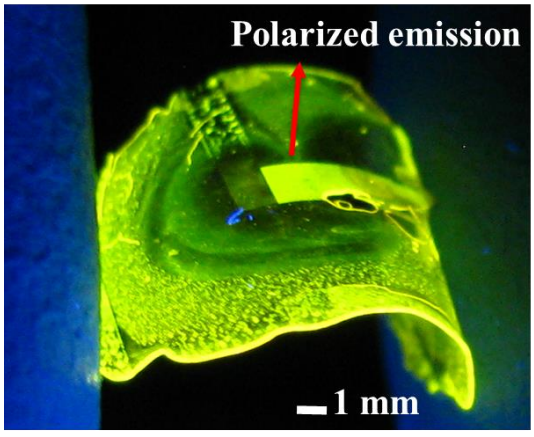


**Figure 5.11:** A photograph of a flexible thin film aligned NRs in a polymer LC. The NRs are excited by a UV lamp and emit polarized light.

In general, the absorption spectrum should not be affected in a dielectric host. The emission spectrum could be slightly red shifted if the concentration of the rods is very high and self-absorption start to play a significant role but usually we would consider this in dense film of NRs without a host. The volume fraction of rods in the LC is too low to have a significant effect to shift the emission and absorption spectrum of the NRs.

#### 5.3.2.3 Results

The anisotropic emission of the deposited NRs is observed using a fluorescence microscope. The NRs are excited in the UV band (330-380 nm) using a Xenon lamp. The NR emission is detected by an Andor CCD camera after passing through a dichroic mirror and a rotatable linear polarizer as shown in Figure 5.8a. Fluorescence microscopy images of the NR layer are shown when the polarizer is oriented perpendicularly (Figure 5.12a) or parallel (Figure 5.12b) to the line electrodes. Figure 5.12c and d are similar measurement close to the edge of the electrodes with 100 times objective.

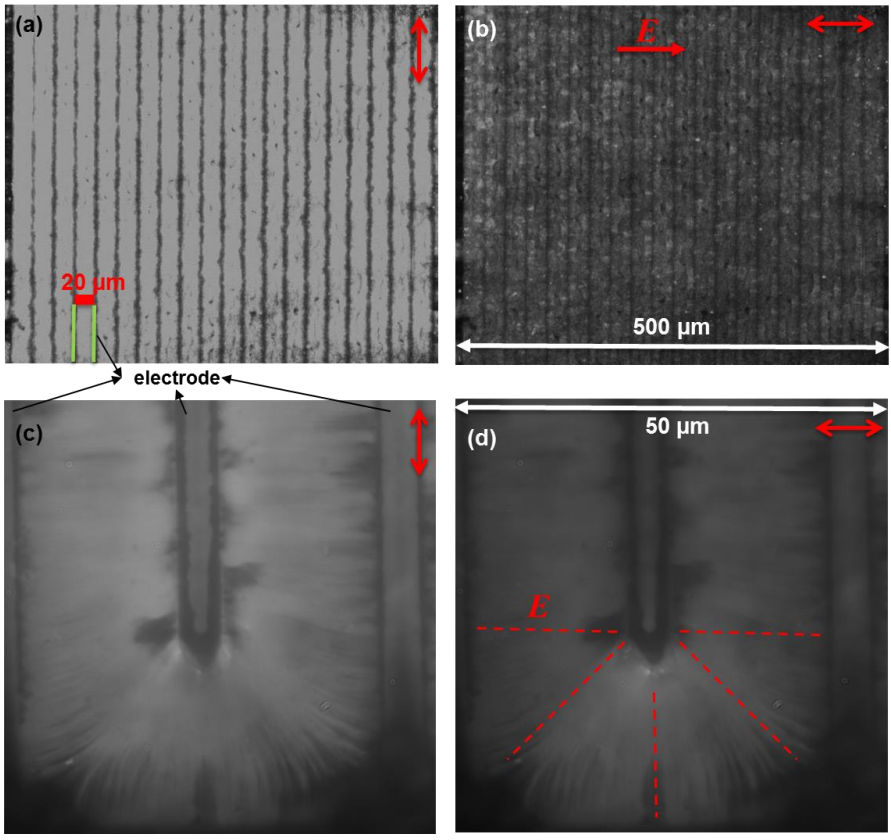


**Figure 5.12:** Fluorescence microscopy images of a deposited layer of NRs in a polymer LC on ITO electrodes with the polarizer oriented (a, c) parallel and (b, d) perpendicular to the applied electric field. The images (c, d) show a zoom-in of an electrode tip.

The lines with lower intensity are the regions of the ITO electrode lines, which illustrates that the NRs tend to move to regions between the electrodes where the electric field is stronger. The photoluminescence is stronger when the polarizer is parallel to the electric field, indicating that the NRs are aligned along the electric field and that they emit light polarized along their long axis. The polarization ratio (equation 5.2) for regions with aligned NRs is about 0.6.

The electric field required to align NRs in dodecane is about 17 V/µm [138]. When an electric field is applied to the mixture of NR and LC, the LCs orient along the electric field. Aligning the NRs in the same direction lowers not only the electrical energy of the NRs, but also the elastic deformation

energy of the LC around the NRs. Figure 5.13 shows fluorescence microscopy images of aligned NRs close to the edges of electrodes. The polarizer is oriented perpendicularly (Figure 5.13a) or parallel (Figure 5.13b) to the line electrodes. Between the electrodes, the NRs are aligned along the electric field, perpendicular to the electrode lines. Note that in the left part two electrodes are disconnected due to lithography issues. Near the end of the electrodes the NR alignment follows the field lines, pointing away from the electrode tips (Figure 5.13c, d), although the electric field is lower than 20 V/µm. The curvature of the bright lines above the area with electrodes is due to a fluid flow, resulting from the applied voltage, and the transport of NRs from the regions between the electrodes where their concentration is higher.

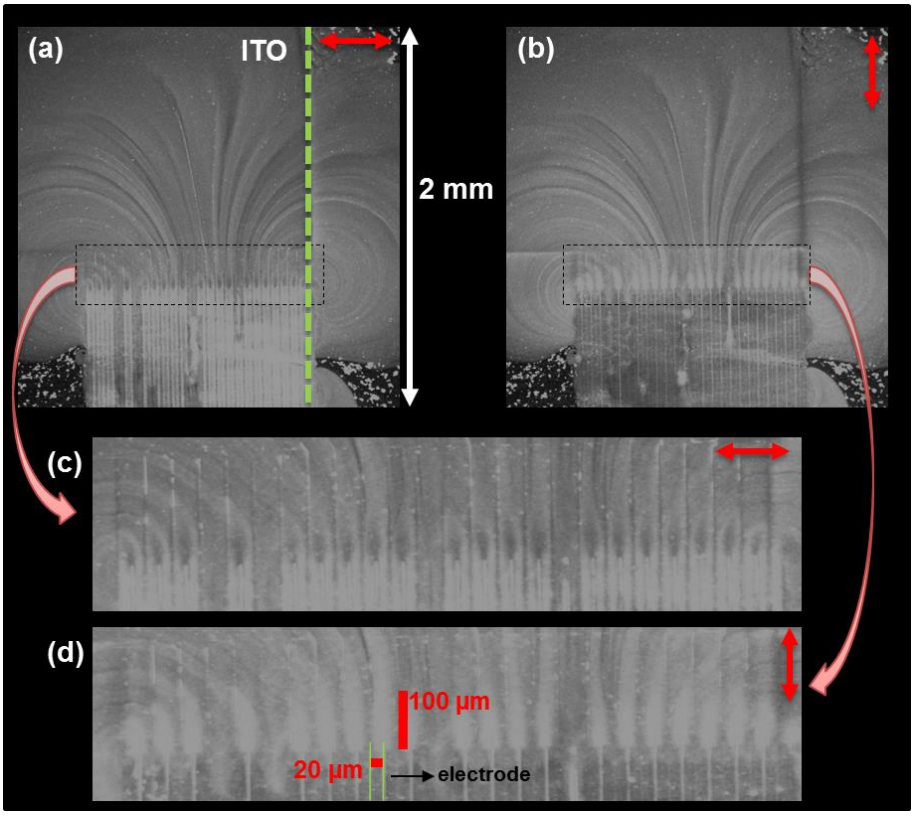


**Figure 5.13:** Fluorescence microscopy images of NRs close to the edge of the electrode area while the polarizer is oriented a) perpendicularly and b) parallel to the line electrodes, c), d) close-up near the edges of the electrodes in image a and b respectively. The applied voltage is 400 V, 1 kHz.

The orientation and the position of NRs in space can be controlled by the design of the electrode pattern that is interesting both from a scientific and a technological point of view. The fluorescence microscopy image in Figure 5.14 shows the accumulation of aligned NRs between the circular in-plane electrodes with 3 µm width and 20 µm gap. The film is made with the same recipe as in Figure 5.13 with an applied AC voltage of 400 V, 1 kHz. Also here some of the electrodes are disconnected.

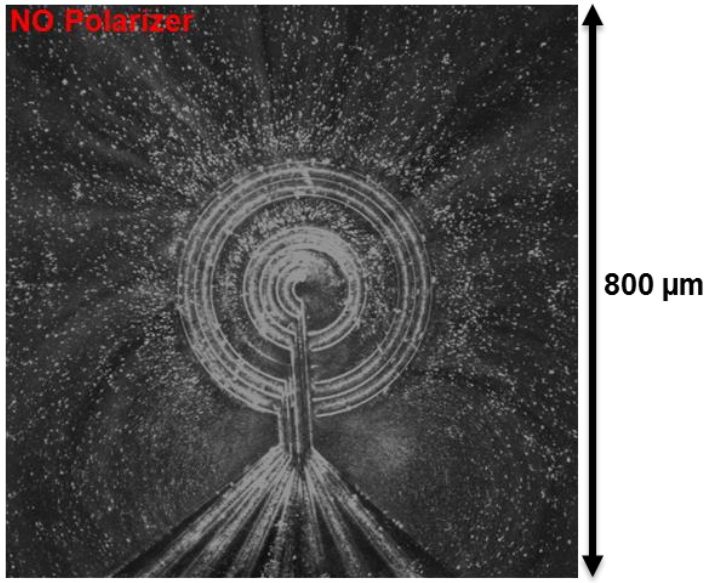


**Figure 5.14:** Fluorescence microscopy image of LC film with NRs near a region with circular electrodes (3 µm width and 20 µm gap) and applied voltage of 400 V, 1 kHz.

In addition, I am able to make a thin film with homeotropic alignment of NRs for solar cell applications. Instead of finger pattern substrate, a one pixel substrate (Figure 4.2d) can be used for this application.

### 5.3.3 NR suspensions in nematic LC

The previous results based on photopolymerized films indicate the potential for applications using polarized light emission. In this section I study the dynamic NRs alignment in (non-polymerizable) LC between two planar substrates covered with homogeneous electrodes. The test device has two 1 $cm^2$ ITO electrodes at a distance of $d$=30 µm. The electric field is approximately homogeneous and given by $E = V/d$. The NR suspension in chloroform is mixed with non-reactive LC (MDA-00-3536) and the solvent is evaporated to obtain a 1 wt% NR in LC suspension. The suspension is filled into the cell without alignment layers by capillary force. The LC director is mainly homeotropic near the ITO surface but with many defects in the bulk, while the NRs are not aligned and the fluorescence is unpolarized. When a voltage is applied both NRs and LCs align along the electric field, as shown in Figure 5.15a and b. A computer controlled DAQ and a 200 times voltage amplifier are used to apply AC fields up to 20 V/µm with frequency between 50 Hz and 40 kHz. The transmission of blue light (using a 470 nm LED array) is measured using a photodetector with response time of 0.7 µs which is mounted on the microscope and DAQ. The alignment of the NRs can be monitored at high speed by measuring the anisotropic absorption of the NRs.

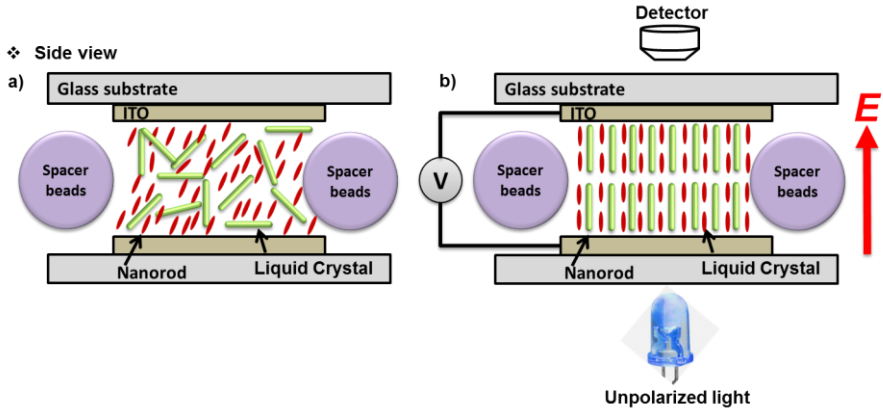


**Figure 5.15:** NRs suspension in liquid crystal: a) without and b) with applied voltage. The applied electric field is perpendicular to the ITO electrodes. The transmission of light through the cell is measured to evaluate the orientation.

The transmission is measured for a 1 wt% NR suspension in the presence of AC electric fields with different amplitudes. Figure 5.16a shows the increase

in transmission when an electric field is applied and the LC director and NRs align along the applied electric field, which is perpendicular to the polarization of the incident light. I represent the Relative Change in Transmission (RCT) as $(T-T_0)/T_0$ where $T_0$ is the average transmission in the OFF state, and $T$ is the average transmission in the presence of an electric field. The 30 µm thick cell filled with nematic LC exhibits considerable scattering due to defects. The scattering of the LC is reduced by applying a voltage, due to the more homogeneous alignment of the LC director in the bulk. The RCT of NRs suspension in pure LC is shown as a function of the electric field in Figure 5.16b. It shows a sharp raise for a field of 1 V/µm and saturates for a field of 2 V/µm, which are both considerably lower than the field required for alignment in dodecane (12 V/µm), see section 4.4) [138]. It means that the LC helps to align the NRs at a lower electric field. In addition, the alignment of the NRs remains for several milliseconds after switching off the voltage due to the relaxation time of the LCs.

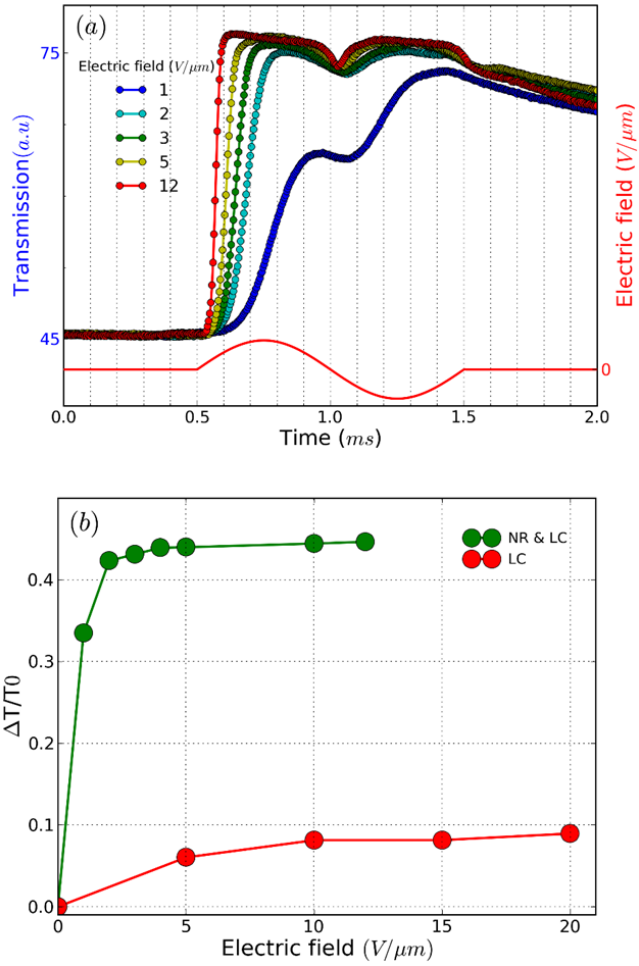


**Figure 5.16:** a) Transmission measurements (dots) for a NR in LC suspension between homogeneous electrodes for blue light (~470 nm) in the presence of an ac electric field with frequency 1 kHz and various amplitudes b) RCT for NR in LC suspension (green dots) and pure LC (red dots) as a function of the electric field.

In another experiment, a cell with 20 µm thick and interdigitated electrodes on one of the substrates (see Figure 5.10b) used to observe the orientation of the NRs by polarization fluorescence microscopy in the absence and presence of an electric field. Figure 5.17a shows bright clusters of NRs that emit unpolarized light. By applying an electric field of 1V/µm, the LC director aligns but the clusters of NRs remain visible (Figure 5.17b). By applying an AC electric field with higher amplitude (20 V/µm) the clusters

disappear. The emission for parallel (Figure 5.17c) and perpendicular (Figure 5.17d) orientation of the polarizer with respect to the line electrodes is different, indicating good alignment of the NRs. The fact that clustering disappears abruptly when the amplitude of the ac field is sufficiently high can be explained by the permanent dipole moment of the NRs that is typically oriented along the long axis. Due to their permanent dipole moment NRs tend to align head to tail (by two or in larger groups) to reduce the electrostatic energy. In an electric field with sufficient amplitude all NRs tend to align their dipole moment in the same direction, thereby breaking the attraction between NRs.

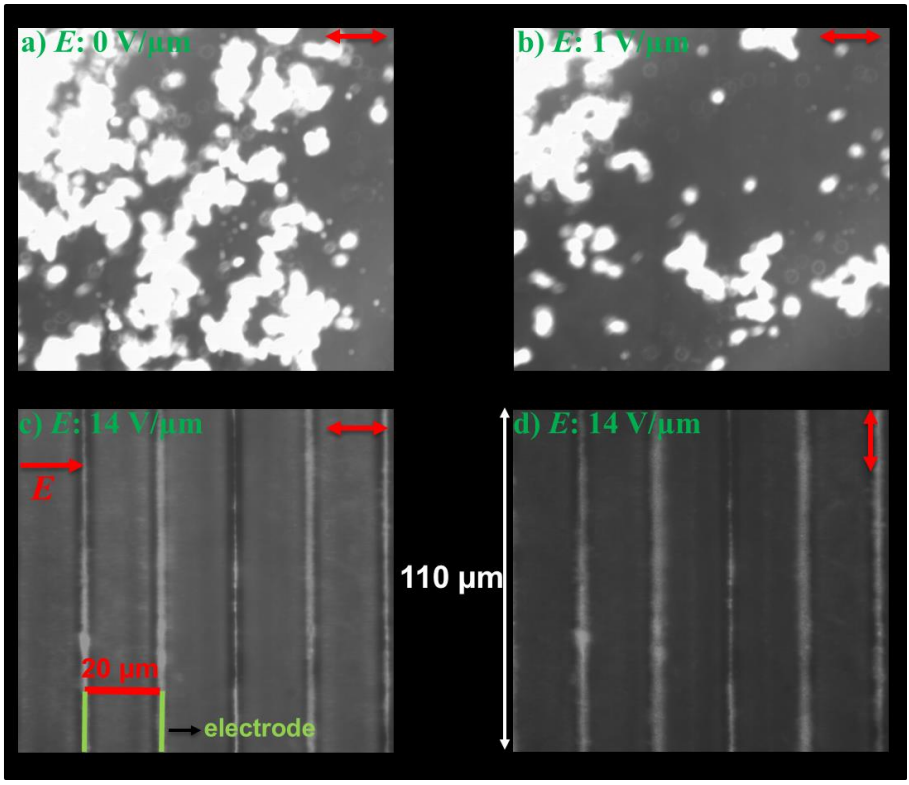


**Figure 5.17:** Polarized fluorescence microscopy images of NRs suspended in LC, in cell with interdigitated electrodes. The electrode gap of 20 µm is indicated by green lines. The electric field is: a) absent, b) 1 V/µm, c) and d) 14 V/µm with the polarizer c) parallel and d) perpendicular to the applied electric field.

The response of the transmission is shown in Figure 5.18 when a block pulse with amplitude 20 V/µm is applied over a dispersion of NRs in non-reactive

LC. Switching on occurs within 0.05 ms while the relaxation time is about 0.5 ms.

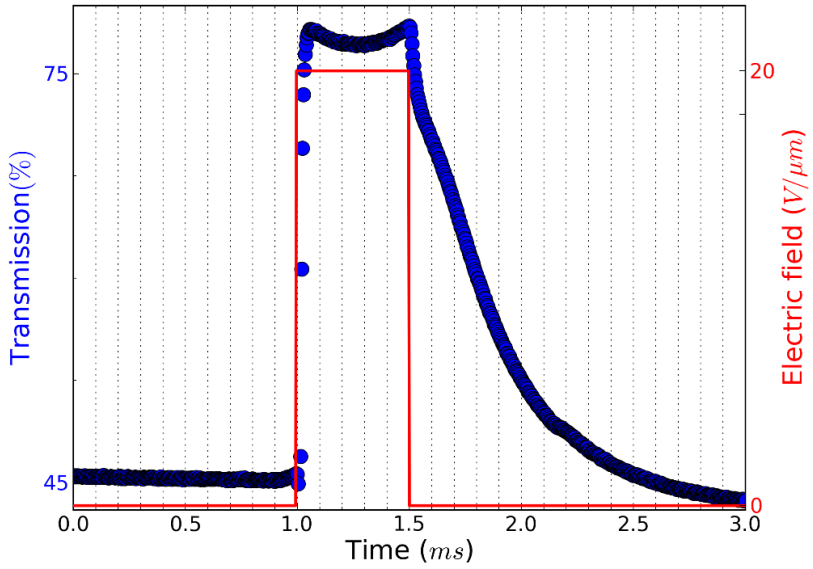


**Figure 5.18:** Transmission versus time of a CdSe/CdS NR suspension in LC when a pulse with amplitude of 20 V/µm is applied.

In conclusion, a thin polarized light emitting film based on aligned NRs in a LC is realized by applying an electric field to align the NRs and simultaneously illuminating with UV to polymerize the reactive LC. An alignment with a polarization ratio of 0.60 has been obtained. The aligned NRs film emits polarized light when illuminated with unpolarized light of an appropriate wavelength. This method is compatible with large-scale processing on cheap, flexible and transparent substrates and also can be realized in a roll-to-roll process. The required electric field strength to align the semiconductor NRs and relaxation time of the NRs in LC are obtained experimentally. The reduction of NR clustering in liquid crystal is realized by applying a high electric field.

## 5.4 Aligned NRs in polymer

In this section, I use UV curable glue (NO68) instead of reactive LC to homogeneously disperse and align CdSe/CdS NRs in a polymer film. The fabrication uses a glass substrate with transparent interdigitated indium tin oxide electrodes. This method is based on doping glue with NRs and consequently aligning the mixture by an electric field. The alignment is fixed after the polymerization reaction. The solid film can be detached from the substrate. Fluorescence microscopy images of the NR layer are shown when the polarizer is oriented perpendicularly (Figure 5.19a) or parallel (Figure 5.19b) to the line electrodes. The lines with lower intensity are the regions of the ITO electrode lines. The polarization ratio (equation 5.2) for regions with aligned NRs is about 0.4. The resulting film emits polarized light when illuminated with unpolarized light of an appropriate wavelength. This method is compatible with large-scale processing on cheap, flexible and transparent substrates.

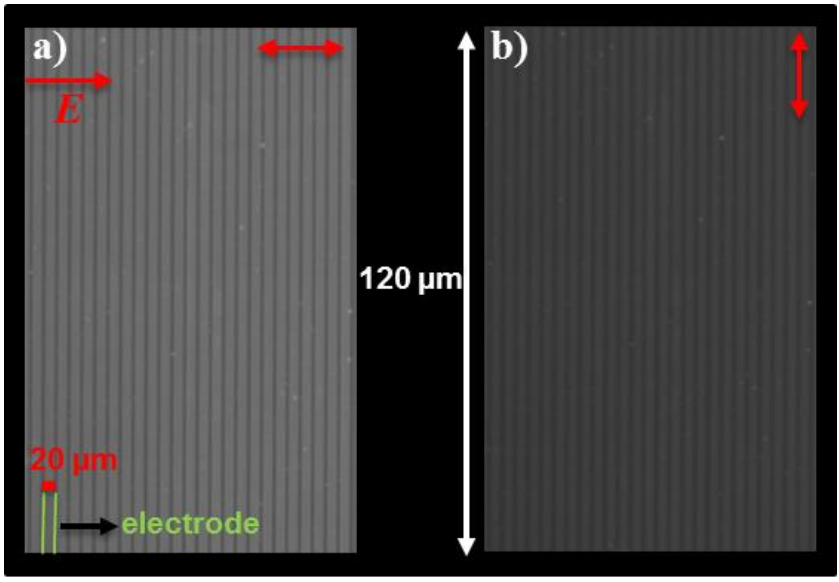


**Figure 5.19:** Fluorescence microscopy images of a deposited layer of NRs in a glue on ITO electrodes with the polarizer oriented (a) parallel and (b) perpendicular to the applied electric field.

## 5.5 Nanorods aligned in polymeric nanofibers

In this section, I demonstrate another method to fabricate a thin film including aligned nanorods based on electrospinning of nanofibers. The electrospinning is performed by Ljiljana Palangetic from the Department of Chemical Engineering at KU Leuven. The NR mixtures are made in the Physics and Chemistry of Nanostructures group at Ghent University. I contributed to this work by integrating the aligned nanofibers in a liquid crystal cell where applying a voltage allows switching the emitted light on and off. I analyze and determine the fluorescence properties of the resulting films and devices. In this section I briefly explain the fabrication of the film and then I focus on my work.

### 5.5.1 Fabrication

#### 5.5.1.1 CdSe/CdS dot-in-rods

The CdSe/CdS NRs are synthesized according to a procedure described in the literature (see the Appendix B, paragraph 1 for the synthesis details) [139]. The synthesized CdSe/CdS NRs have an average diameter of 4.1 nm and an average length of 29.3 nm which is different from the NRs used in the previous section. Figure 5.20 shows a TEM image of the synthesized CdSe/CdS NRs.

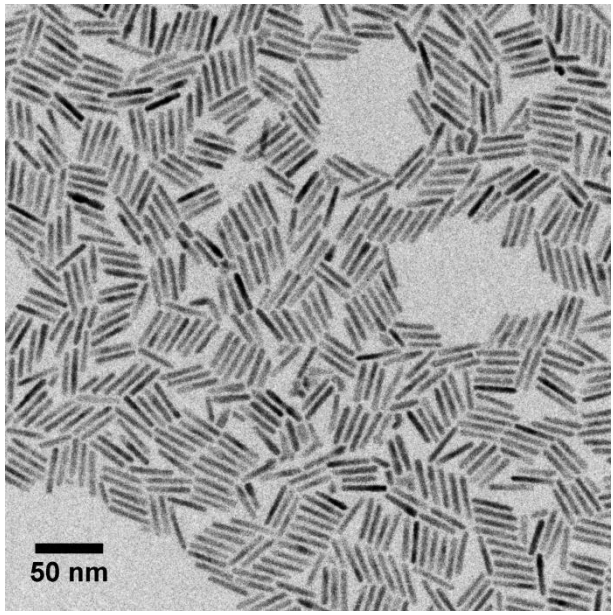


**Figure 5.20:** TEM image of the CdSe/CdS dot-in-rods on a copper grid coated with a carbon film.

The absorption and emission spectra of the CdSe/CdS NRs are measured in toluene and are revealed in Figure 5.21. The NRs have an emission around 600 nm for an excitation wavelength of 365 nm.

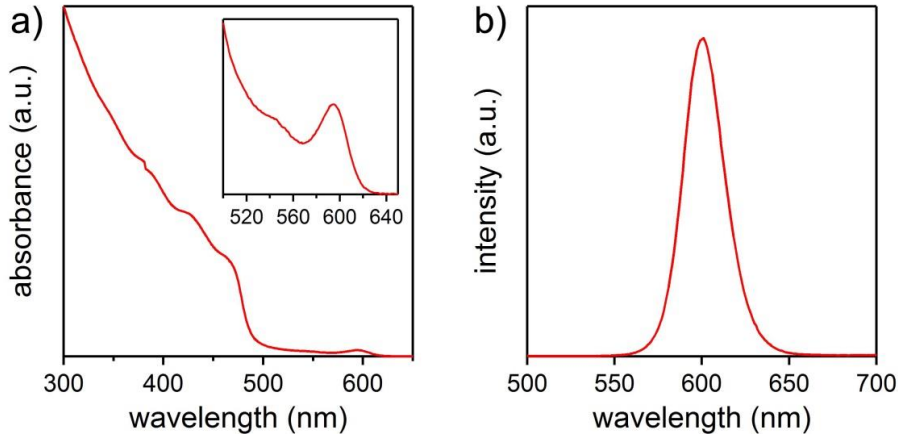


**Figure 5.21:** (a) Absorption spectrum (inset: focus on the absorption of the CdSe core) and (b) emission spectrum of the CdSe/CdS NRs in toluene for an excitation wavelength of 365 nm.

The CdSe/CdS NR suspension should be mixed with the polymer before electrospinning deposition. But apolar solvents such as chloroform or toluene which I already used in the dip coating method are not compatible with the polymer and NRs cannot be dispersed in polar solvent. To overcome this problem and to be able to disperse the NRs in ethanol, the NRs are first coated with silica (see the Appendix B, paragraph 2 for the complete coating details).

The TEM image of the CdSe/CdS NRs coated with 6 nm of $SiO_2$ is shown in Figure 5.22a. The aspect ratio is reduced to 2.4 while the initial CdSe/CdS NRs have an aspect ratio of 7.1. The coated NRs are mixed with PVP and deposited with the electrospinning method to produce a 1.5 $cm^2$ film (The details of electrospinning of the nanofibers are explained in Appendix B paragraph 3). Figure 5.22b shows scanning electron microscopy (SEM) image of the collected nanofibers. This image shows that most of the fibers are deposited parallel to each other. The parallel fibers are collected between two Aluminum stripes as shown in Figure 5.22c. The TEM image of a single nanofiber in Figure 5.22d indicates that most of the NRs are aligned along the axis of the nanofiber.

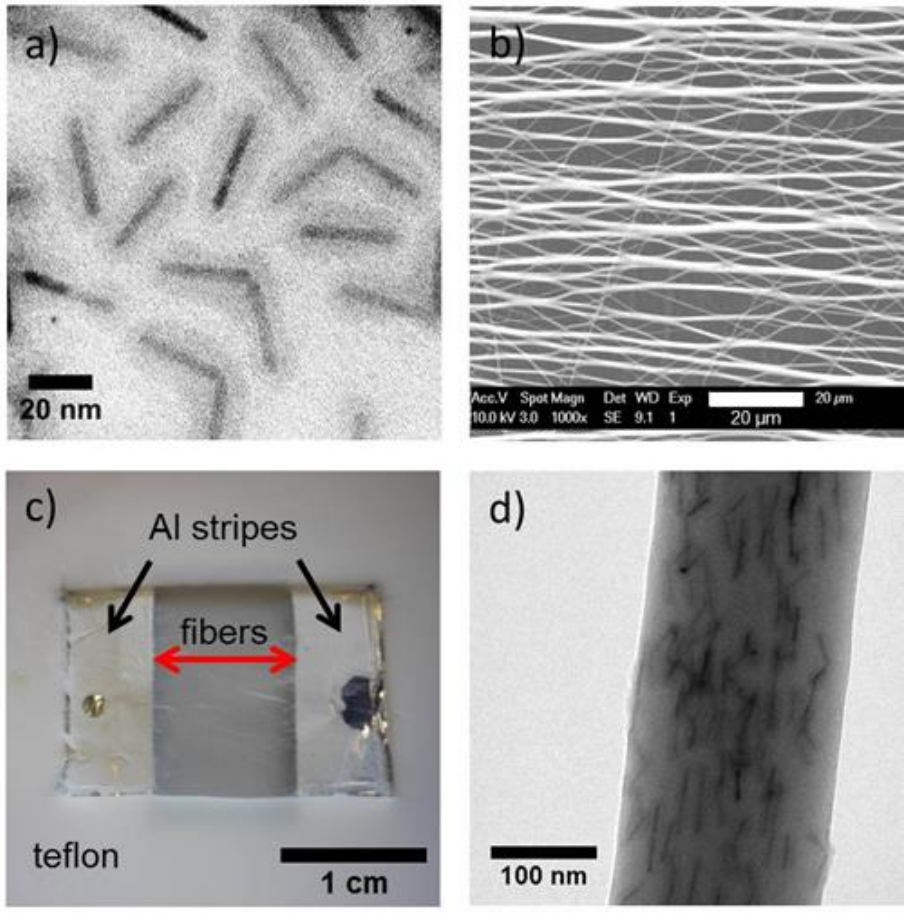


**Figure 5.22:** (a) TEM image of the CdSe/CdS NRs coated with $SiO_2$. (b) SEM image of the aligned nanofibers. (c) Photography of the aligned nanofibers film (red arrow indicates the alignment direction of the nanofibers). (d) TEM image of the nanofiber.

### 5.5.2 Results and discussion

The anisotropic emission of the deposited nanofibers is observed using a fluorescence microscope. In order to avoid emission from the LC which also absorbs in the UV range, the NRs are excited with a Xenon lamp in the green band (510-560 nm) which corresponds to absorption of the CdSe cores in the CdSe/CdS NRs (see Appendix B, Figure B.1 for their optical characterization). The NR emission is detected by an Andor CCD camera after passing through a dichroic mirror and a rotatable linear polarizer as

shown in Figure 5.8a. Fluorescence microscopy images of the NR layer are shown when the polarizer is oriented perpendicularly (Figure 5.23a) or parallel (Figure 5.23b) to the nanofibers long axis. The integrated intensity $I$ as a function of the orientation of the polarizer is shown in Figure 5.23c which can be fitted to the function: $I_{\perp} + \left(I_{\parallel} - I_{\perp}\right)\cos^2\theta$ [96, 140, 141]. The obtained polarization ratio (defined by equation 5.2) for the nanofiber film is 0.45.

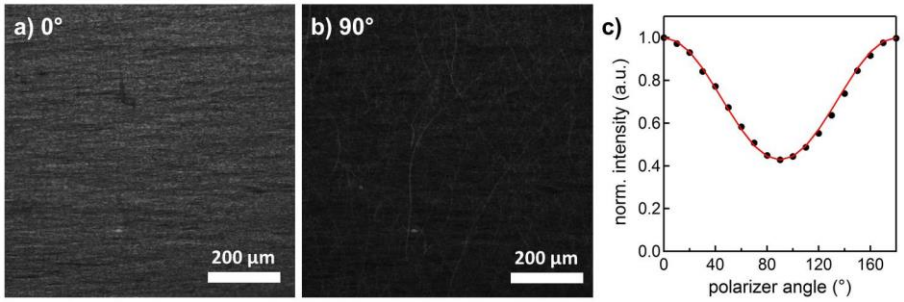


**Figure 5.23:** Fluorescence microscopy images of the aligned nanofibers when the polarizer is (a) parallel (0°) or (b) perpendicular (90°) to the axis of nanofibers. (c) Normalized integrated intensities as a function of the polarizer angle (black markers) fitted with a $\cos^2$ function (red line).

A single nanofiber is also analyzed by fluorescence microscopy using a 100× objective. Figure 5.24a shows a bright nanofiber when the polarizer is oriented parallel to its long axis. The fiber loses brightness when the polarizer is oriented perpendicular to its long axis as shown in Figure 5.24b. This figure specifically indicates that most of the NRs are aligned along the axis of the nanofibers. The best obtained polarization ratio for a single nanofiber is 0.55. This means that if the electrospinning deposition could be improved and all nanofibers align parallel to each other, the maximum polarization ratio could reach 0.55 with this method.

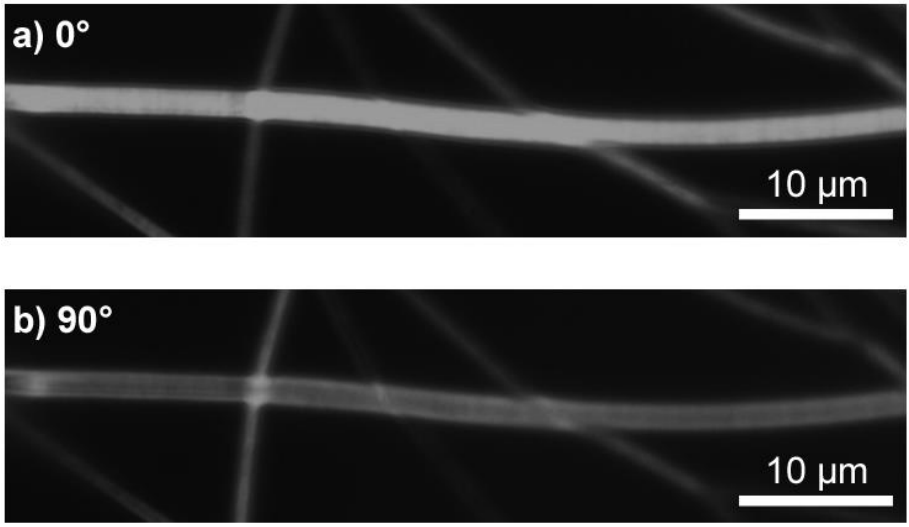


**Figure 5.24:** Fluorescence microscopy image of a single nanofiber (large horizontal one), when the polarizer is (a) parallel (0°) or (b) perpendicular (90°) to the axis of nanofibers.

Additional measurements by fluorescence microscopy are performed on a film of aligned nanofibers using UV excitation (330-380 nm) which corresponds to the absorption of the CdS shell. The emission from PVP with such high molecular weight (1,300,000 g/mol) is negligible compared to the emission of the NRs. Figure 5.25 a, b show the fluorescence microscopy images of the NR layer when the polarizer is oriented perpendicular and parallel to the nanofiber's long axis respectively. The obtained polarization ratio is 0.45 which is as same as the polarization ratio of the film with green excitation. It indicates that the CdSe core and the CdS shell have similar degree of linear polarization which is in line with previous reports indicating that the dipole moments are aligned along the same direction in the CdSe core and in the CdS shell [141].

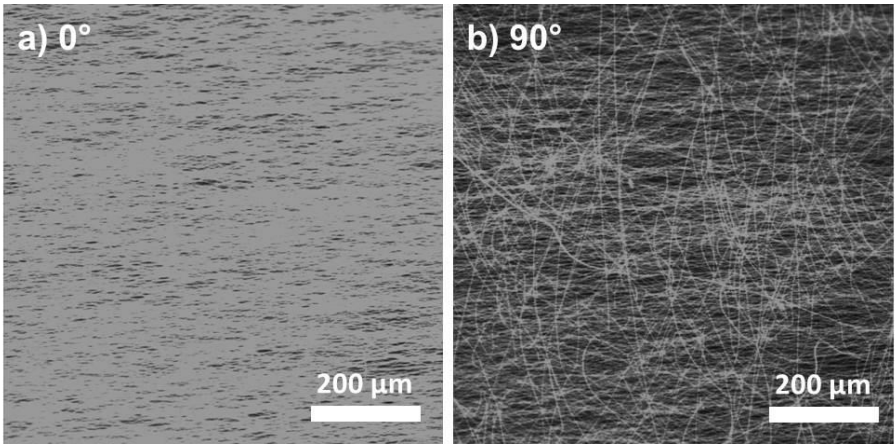


**Figure 5.25:** Fluorescence microscopy images under UV excitation (330-380 nm) of the aligned nanofibers when the polarizer is (a) parallel (0°) or (b) perpendicular (90°) to the axis of nanofibers.

### 5.5.3 Integration in a liquid crystal cell

The fabricated thin films in this dissertation can be used as a polarized emitter in different devices. In this section I integrate the nanofiber film in a LC cell.

The cell as shown in Figure 5.26 consists of two glass substrates coated with 30 nm thick indium-tin-oxide (ITO) electrodes. Nylon-66 is coated on the ITO side of one of the substrates with thickness of 300 nm and rubbed mechanically. The film of aligned nanofibers is placed onto the ITO side of the other substrate. The substrates are bound together with glue containing spacer beads of 10 µm (Sekisui Chemicals) while the direction of rubbed nylon and long axis of nanofiber are perpendicular. The LC (E7-Merck) is infiltrated into the cell in the nematic phase at room temperature. Because of the direction of the fibers and the direction of rubbing on the other substrate have an angle of 90°, the LC makes a twist of 90°between these two layers. It is expected that the LC aligns along the direction of the nanofibers. The experimental results further in this section will confirm this assumption. To ensure that the polarization of light follows the twisting of the LC, the conditions of the Maugain regime are verified. The condition for the Maugain regime is expressed as [142]:

$$\frac{2\lambda}{P\Delta n} \ll 1 \qquad 5.3$$

Where $\lambda$ is the wavelength of the light,$\Delta n$ is the birefringence of the LC and $P$ is the pitch of the twisted liquid crystal which is four times the cell gap. The values for these parameters are $\lambda \approx 600$ nm, $P \approx 4\times10$ µm and $\Delta n = 0.215$. This results in a value of $\frac{2\lambda}{P\Delta n} = 0.14$, which indicates that the Maugain regime is valid.

To observe the polarized emission of the device, a same measurement has been done by fluorescence microscopy under green excitation with different experimental conditions. First, the azimuth of the polarizer is parallel to the long axis of the nanofiber as shown in Figure 5.26a. The microscope image is dark and indicates that the emission of the NRs is blocked. The initial polarization direction of the NR emission is following the twist of the LC director and rotates 90°. This direction is perpendicular to the azimuth of the polarizer and the light cannot pass. In the second condition, the polarizer is rotated 90° and the azimuth of the polarizer is perpendicular to the long axis of the nanofiber. In this case the emitted light can pass through the polarizer and is detected by detector. For this reason we call this the ON state as shown in Figure 5.26b. The polarization ratio of the device (the fluorescence microscopy images of Figure 5.26a and b) is measured to be 0.45 which is the same as the nanofiber film. This indicates that integrating the nanofiber film with LC does not affect the polarization ratio. In the third situation, a sine wave AC electric field (5V/µm, 1 kHz) is applied to the cell. The twisted LCs reorient along the applied electric field and consequently the polarization of the emitted light does not change due to the LC. It means that the polarization direction of the emitted light between the cell and the polarizer is parallel to the long axis of the nanofiber and perpendicular to the azimuth of the polarizer. As a result, the light is blocked and we call this the OFF state as indicated in Figure 5.26c. The polarization ratio between the ON and OFF state is obtained 0.43 which is close to the value of 0.45. This indicates a high efficiency of the electrical switching of the LC in this polarized light emitting device. Also to indicate that the device can switch in large scale, the device excited with a portable UV lamp and the images are taken corresponding to the conditions of Figure 5.26 b and c. The images are shown as the insets in Figure 5.26 b and c.

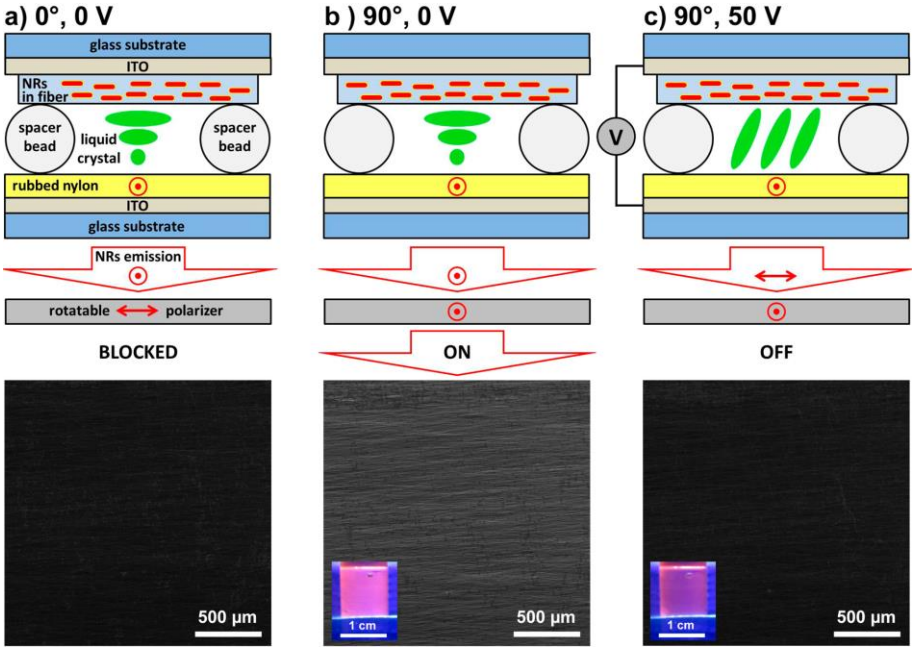


**Figure 5.26:** Sketch of the device with nanofibers and LC and polarizer in various conditions with the corresponding fluorescence microscopy images (a) Azimuth of the polarizer is parallel to the long axis of the nanofibers (0°), no applied electric field. (b) Azimuth of the polarizer is perpendicular to the long axis of the nanofibers (90°), no applied electric field (ON state). (c) Azimuth of the polarizer is perpendicular to the long axis of the nanofibers (90°), a sine wave 5V/µm, 1 kHz electric field is applied (OFF state). Insets of the fluorescence microscopy images in (b) and (c): corresponding photographs of the device using a portable UV lamp for the excitation.

In the fourth condition, the azimuth of the polarizer is parallel to the long axis of the nanofibers and the electric field is still applied. In this case, the emitted light can pass through the polarizer and can be detected as shown in Figure 5.27b. The polarization ratio between the cases in Figure 5.27 (two azimuth angles in the presence of the 5 V/µm electric field) is 0.31 which is less than the polarization ratio of the original nanofiber film. By applying 5 V/µm, the LC aligns along the direction of the electric field but the alignment is not perfectly vertical. Due to this effect, the linear polarization state originating from the NRs is distorted and the light becomes slightly elliptical. This results in a reduction in contrast between the two polarization states.

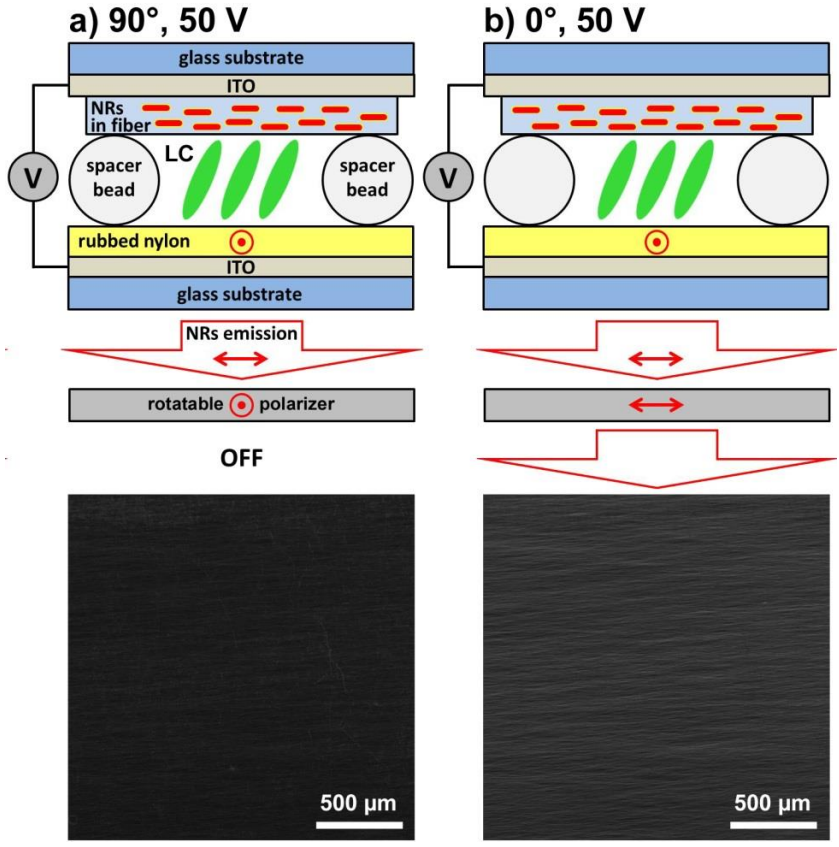


**Figure 5.27:** Sketch of the device with the nanofibers and corresponding fluorescence microscopy images under a AC electric field (5 V/µm, 1 kHz) and with the azimuth of the polarizer (a) perpendicular (90°) and (b) parallel (0°) to the long axis of the nanofibers.

In conclusion, a polarization ratio of 0.45 is obtained for a flexible thin film with large scale (1.5 $cm^2$). The film is integrated with LC and it is demonstrated that it can be used as a polarized light emitter which can be switched on and off. The device is maintaining the polarization ratio to a large extent.

## 5.6 Conclusion

In this chapter I demonstrated four methods to control the position and orientation of semiconductor NRs and fabricate aligned NR film. As a comparison, the different methods to align CdSe/CdS NRs used in the literature and the methods presented in this chapter are listed in Table 5.1.

**Table 5.1:** Comparison of methods for aligning NRs

| Ref. Num | Substrate | Deposition method | Aligning method | Order parameter | Polarization ratio | features |
|---|---|---|---|---|---|---|
| [28] | CBP | Contact printing | evaporation method at the liquid-solid-air interface | - | 0.34 | |
| [32] | Glass | Drop casting | Coffee stain evaporation | - | -0.3 | |
| [118] | ZnS/$SiO_2$ | wet-chemical | wet-chemical & epitaxial growth | - | 0.54 | |
| [93] | Glass | Spin coating | Mechanical Rubbing | - | 0.49 | -large scale |
| [87] | $Si/SiO_2$ | Drop casting | DC field (25 V/μm) | - | 0.45 | |
| [124] | $Si_3N_4$ | Drop casting | DC field (28 V/μm) | 0.73 | - | |
| Our work | Glass | Dip coating | AC field (20 V/μm) | 0.92 | 0.6 | -Can be applied for large scale |
| Our work | Glass | Fill in a cell | AC field (20 V/μm) | - | 0.4 | -flexible -free-standing -large scale |
| Our work | Glass | Fill in a cell | AC field (20 V/μm)-LC | - | 0.60 | -flexible -free-standing -large scale |
| Our work | Stand free | Electro spinning | Electrospinning-fiber | - | 0.45 | -flexible -free-standing -large scale |

The dip coating deposition method is fast, facile and can be applied on relatively large substrates. NR alignment with an order parameter of 0.92 and a polarization ratio of 0.60 is obtained with this method. A thin and flexible polarized light emitting film based on aligned NRs in a LC or polymer is realized. These methods are compatible with large-scale processing on cheap, flexible and transparent substrates and also can be realized in a roll-to-roll process. An alignment with a polarization ratio of 0.60 has been obtained for LC methods. Finally I have demonstrated the integration of nanofibers and liquid crystal, to show an efficient way of electrically switching on and off polarized light over a large area. I believe that this four methods can be extended to the deposition or printing of most of aligned anisotropic particles.

# Chapter 6

# Conclusions and outlook

In this final chapter, I list the main conclusions of this work and make suggestions for future developments for the different devices that have been discussed.

## 6.1 Conclusions

In this work I successfully demonstrated devices that are based on thin films of (polymerizable) liquid crystals and/or aligned nanorods.

In chapter two, I demonstrate the fabrication of thin film polarizers and color filters based on photo-polymerization of liquid crystalline mono(di)acrylate monomers. The thin film dye-doped polarizer has a broad absorption band between 400 nm and 650 nm and has a contrast ratio of 9 for a film of only 12 µm. The thin film polarizer is fabricated for applications which require small thicknesses of the final device such as electro-active contact lenses. I also demonstrate a technique to make a mono domain CLC thin film color filter with a color that can be chosen. The key parameter to have a mono domain CLC film is cooling rate. The photonic band gap of the color filter is around 80 nm with high reflectivity in the bandgap for one circular polarization. Both thin films have thermal stability up to 100 °C, chemical resistivity for polar protic solvent and can be detached from the substrate.

A widely tunable optical CLC filter with microsecond switching time is demonstrated in chapter three. A wavelength shift of the photonic band gap of 141 nm is obtained by electric switching. The device consists of a mixture of photo-polymerizable liquid crystal, non-reactive nematic liquid crystal and a chiral dopant is polymerized with UV light. The devices feature high reflectivity in the photonic band gap without degradation or disruption when applying voltages. The response times are 50 µs and 20 µs for switching on and off respectively. The influence of the amplitude of the applied voltage on the width and the depth of the reflection band is investigated. I also investigated the influence of UV illumination on a partially polymerized chiral liquid crystal. A blue-wavelength shift of the photonic band gap is obtained for increasing power or duration time of UV illumination and for increasing thickness of the cells. The width and depth of the photonic band gap is unaffected by the change in UV curing conditions, which indicates that there is no degradation by the UV light.

Based on the developed PPCLC devices that only work for circularly polarized light, I demonstrate that also a microsecond-range optical shutter for unpolarized light can be made. The device consists of two PPCLC layers separated by a half wave plate. The device works independently of the polarization state of the incoming light beam. Modulation between 3% transmission and 60% transmission is obtained within a wavelength range of 50 nm with a response time of 20 µs. The shutter features high reflectivity in

the photonic band gap. The influence of the amplitude of the applied voltage on the width and the depth of the reflection band is investigated.

In the second part of my work, the theory of alignment of semiconductor nanorods by an external electric field is described for simultaneously appearing permanent and dielectric dipole moments. A full alignment of colloidal NRs in suspension by an electric field is demonstrated. By comparing optical transmission measurements with theoretical simulations, the permanent and induced dipole moments of the NRs are determined. The required electric field, the values of the permanent dipole moment, relaxation time, absorption anisotropy and critical frequency of the CdSe/CdS dots in rods are determined. The correlation between theory and experiment indicates that the orientation is driven by the permanent dipole moment of the NRs. In addition, I experimentally verify the anisotropic absorption of the CdSe NRs core for a wavelength of 560 nm.

Finally, four methods for the homogeneous deposition and alignment of NRs in solid films from a colloidal suspension are demonstrated. The accumulation, orientation and polarized fluorescence of the NRs is verified by AFM and polarized fluorescence microscopy. The four methods investigated in this work for aligning NRs are

1- Dip coating and evaporation of a NR solution in presence of electric field

2- Depositing and curing of UV curable monomer with NRs in the presence of an applied electric field

3- Depositing and curing of reactive LC with NRs in the presence of an applied electric field.

4- Electro spinning of NRs in a polymer fiber.

An alignment with order parameter 0.92 and a polarization ratio of 0.60 is obtained with the dip coating method.

I demonstrate a thin and flexible polarized light emitting film based on aligned NRs in a LC with polarization ratio of 0.6.

Finally I demonstrated that combining aligned nanofibers and liquid crystal, constitutes an efficient way of electrically switching on and off polarized light while fully preserving the polarization ratio of 0.45 over a large area.

## 6.2 Future work

### 6.2.1 LC devices

As the fabricated thin films can be detached from the substrate, these films are useful for e.g. transfer onto flexible substrates. These films are suitable to be processed in optical device manufacturing as additional films or as in-cell optical components. A broad range of thin film color filter can be made by our methods. The thin film color filter can be used as a mirrors for laser applications, for example in a QD laser.

For the case of the polarizer, it is known that the nematic phase results in a relatively low dichroic dye order parameter and a low dichroic ratio. Using smectic phases, the dichroic ratio and hence the contrast of the film could still be improved drastically in the future.

### 6.2.2 Aligned NR devices

The homogeneous deposition of aligned NRs on large substrates is interesting for large area applications such as solar cells and OLEDs. Moreover, semiconductor nanoparticles can be used to efficiently transform blue light from GaN-based LEDs into for example green and red light, which is also needed for colour displays. The combination of blue, green and red light is desired for backlights in liquid crystal displays. As liquid crystal devices modulate the transmission of polarized light, it would be an advantage to start from a backlight that is able to emit polarized green and red light. These aligning methods are compatible with large-scale processing on cheap, flexible and transparent substrates and also (in case of aligned NR in LC) can be realized in a roll-to-roll process. Also these methods can be considered for other kinds of anisotropic semiconductor nanorods with various aspect ratios. In the case of nanofibers, the polarization ratio could be further manipulated, especially if one would be able to avoid the connection between NRs.

# Appendix A

# Supporting information for alignment of CdSe/CdS NRs

**1. Synthesis of CdSe/CdS NRs (5*5*50nm)**

The first step in synthesizing CdSe/CdS dot-in-rods is making CdSe core QDs[139]. They are prepared from a mixture of 0.12 g of CdO, 6 g of trioctylphosphine oxide (TOPO) and 0.56 g of octadecylphosphonic acid (ODPA) which is degassed under vacuum at 120 °C for 1 hour. Next, the mixture is heated to 350 °C under nitrogen atmosphere and a mixture of 0.116 g of Se and 0.72 g of trioctylphosphine (TOP) is quickly injected. The reaction time is adjusted to obtain CdSe QDs with a diameter of 2.3 nm. The reaction is then quenched and the QDs are purified three times by centrifugation, using toluene and isopropanol as the solvent and the non-solvent respectively. The size and concentration of the CdSe QDs are determined from UV-vis absorption measurements, using an already published sizing curve,[143] and extinction coefficient.[144] The CdSe/CdS dot-in-rods are prepared from a mixture of 0.057 g of CdO, 3 g of TOPO, 0.25 g of ODPA and 0.08 g of hexylphosphonic acid (HPA) which is degassed under vacuum at 120 °C for 1 hour. Next, the mixture is heated to 360 °C under nitrogen atmosphere and 1.9 ml of TOP is injected. Subsequently, at the same temperature 0.089 g of sulfur in 1.9 ml of TOP and 70 nmol of the above-mentioned CdSe QDs are injected in the reaction mixture. The reaction is quenched after 8 minutes and the dot-in-rods are purified three times by centrifugation, using toluene and isopropanol as the solvent and the non-solvent respectively. The NRs involved in this work have an average diameter of 4.8 nm and an average length of 51.5 nm as determined by TEM observation (Figure A.1). The concentration of the NRs suspension in toluene is estimated from the amount of CdSe seeds, considering that no particle was lost during the process.

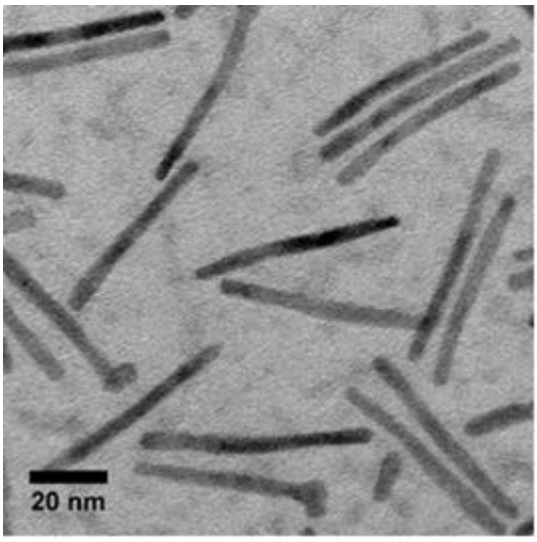


**Figure A.1:** TEM image of the CdSe/CdS dot-in-rods on a cupper grid coated with a carbon film.

## 2. Characterization techniques

Atomic force microscopy (AFM) images are recorded using a Molecular Imaging PicoPlus microscpoce working in alternative contact mode. The transmission electron microscopy (TEM) images are taken using a Cs corrected JEOL 2200 FS microscope. Absorption spectrum is taken using a Perking Elmer Lambda 950 spectrometer. Steady-state photoluminescence measurements are performed with an Edinburgh Instruments FLSP920 setup. The emission spectrum is recorded for an excitation wavelength of 365 nm and is corrected over the sensitivity of the detector.

## 3. CdSe/CdS @ dodecane in cell

Two glass substrates with 1 $cm^2$ ITO electrodes are used to make cells with 50 μm spacing *d* between the electrodes. The NRs suspension is filled inside the cell by capillary force. The NRs dispersed in dodecane are infiltrated into the cells. Figure A.2 shows the NRs suspension in the 1 pixel cell.

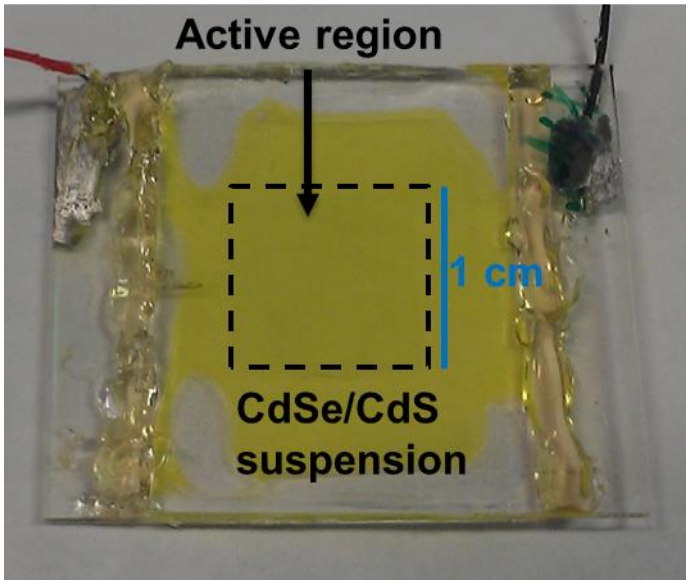


**Figure A.2:** Photograph of the 50 µm thick cell filled with a 1 µM dispersion of NRs in dodecane.

**4. Transmission measurement of CdSe/CdS NR suspension in dodecane**

The transmission of a 50 µm thick cell filled with a 1 µM dispersion of NRs in dodecane at 470 nm is measured in the presence of a block wave AC electric field (17 V/µm, 5 kHz). Figure A.3 shows the variation in the transmission of the NR dispersion, together with the applied electric field. It demonstrates that the transmission of the dispersion switches within 100 µs.

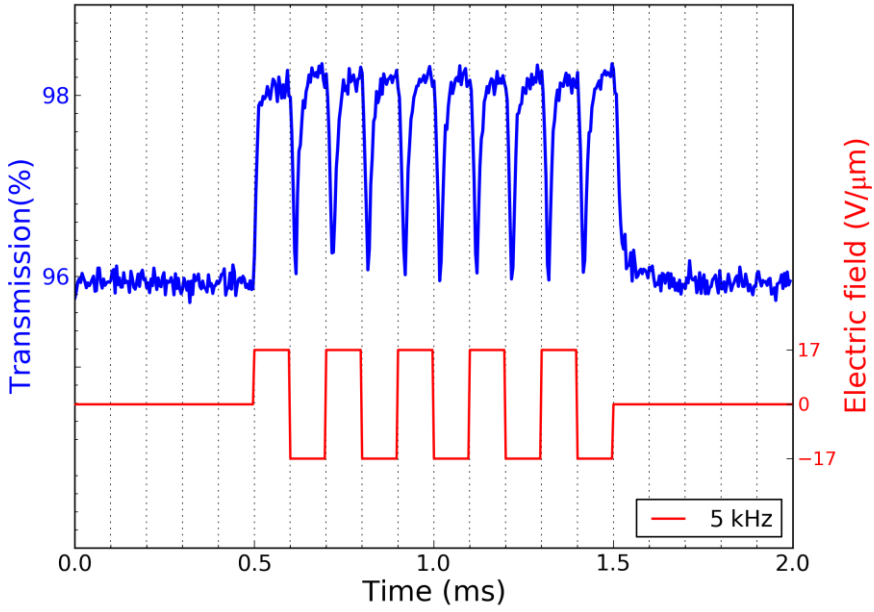


**Figure A.3:** Transmission of a CdSe/CdS NR suspension (blue) for blue (~470 nm) light with and without the presence of a block AC electric field with a frequency of 5 kHz and an amplitude of 17 V/µm (red).

---

And your Lord has commanded that you shall not serve (any) but Him, and goodness to your parents. If either or both of them reach old age with you, say not to them (so much as) “Ugh” nor chide them, and speak to them a generous word. And make yourself submissively gentle to them with compassion, and say: O my Lord! Have compassion on them, as they brought me up (when I was) little.

---

# Appendix B

# $CdSe/CdS@SiO_2@PVP$ nanofibers fabrication

**1. Synthesis of the CdSe/CdS NRs**

The first step in synthetizing CdSe/CdS dot-in-rods is making CdSe core QDs.[139] They were prepared from a mixture of 0.12 g of CdO, 6 g of trioctylphosphine oxide (TOPO) and 0.56 g of octadecylphosphonic acid (ODPA) which was degassed under vacuum at 120 °C for 1 hour. Next, the mixture was heated to 350 °C under nitrogen atmosphere and a mixture of 0.116 g of Se and 0.72 g of trioctylphosphine (TOP) was quickly injected. The reaction time was adjusted to obtain CdSe QDs with a diameter of 3.3 nm. The reaction was then quenched and the QDs were purified three times by centrifugation, using toluene and isopropanol as the solvent and the non-solvent respectively.

The size and concentration of the CdSe QDs were determined from UV-vis absorption measurement, using already published sizing curve,[143] and extinction coefficient.[144]

The CdSe/CdS dot-in-rods were prepared from a mixture of 0.057 g of CdO, 3 g of TOPO, 0.25 g of ODPA and 0.08 g of hexylphosphonic acid (HPA) which was degassed under vacuum at 120 °C for 1 hour. Next, the mixture was heated to 360 °C under nitrogen atmosphere and 1.9 ml of TOP were injected. Subsequently, at the same temperature 0.089 g of sulfur in 1.9 ml of TOP and 70 nmol of the above-mentioned CdSe QDs were injected in the reaction mixture. The reaction was quenched after 8 minutes and the dot-in-rods were purified three times by centrifugation, using toluene and isopropanol as the solvent and the non-solvent respectively. The NRs involved in this work have an average diameter of 4.1 nm and an average length of 29.3 nm. The concentration of the NRs suspension in toluene was estimated from the absorbance at 300 nm and 350 nm, by considering that only CdS contributes to the absorption at these wavelengths, and using the intrinsic absorption coefficients ($\mu_{300}$ = 173021 $cm^{-1}$ and $\mu_{350}$ = 124425 $cm^{-1}$) calculated from the Maxwell–Garnett effective medium theory.[145]

**2. Silica encapsulation of the NRs**

This technique has already proven to be very efficient for the silica coating of initially hydrophobic nanocrystals, including CdSe/CdS dot-in-rods.[146] Here, 10 nmol of NRs is mixed with 100 mL of *n*-heptane (99%, VWR) and 32 mL of polyoxyethylene (4) lauryl ether (Brij L4, formerly known as Brij 30, Sigma-Aldrich). After 15 min under magnetic stirring, 5 mL of MilliQ $H_2O$ and 0.5 mL of $NH_4OH$ (28% in water, VWR) is slowly added to form the microemulsion. After 1 hour under stirring, 0.25 mL of tetraethyl

orthosilicate (TEOS, 98%, Sigma-Aldrich) is added to the microemulsion. The reaction is left stirring for two days to form the silica shell. The CdSe/CdS@$SiO_2$ NRs are then further functionalized with polyethylene glycol (PEG) to provide them with enhanced colloidal stability in polar solvents and to prevent particle-to-particle aggregation. PEGylation of the CdSe/CdS@$SiO_2$ NRs is done in a one-pot process, following the growth of the silica shell, by adding 120 mg of methoxy-PEG-silane (mPEG-silane, $M_w \approx 1000$ g/mol, Gelest) to the microemulsion. After 3 additional days of stirring, the reaction is stopped by adding a large volume of ethanol, resulting in the destabilization of the microemulsion and precipitation of the particles which are collected by centrifugation. The PEGylated CdSe/CdS@$SiO_2$ particles are further purified twice with *n*-heptane and redispersed in ethanol.

**3. Electrospinning of the nanofibers.**

The NRs are mixed with a polymer by adding 240 mg of polyvinylpyrrolidone (PVP, $M_w$ = 1,300,000 g/mol, Sigma-Aldrich) to a solution containing 4.65 nmol of the CdSe/CdS@$SiO_2$ NRs in 2.81 g of ethanol. Even though the NRs are coated with silica, I avoid using water since this is a rather harsh environment that tends to deteriorate the optical properties of the semiconductor NRs.[146] The relatively high molecular weight has been chosen for the ease of nanofiber formation by electrospinning.[147] The nanofibers are made using a climate controlled electrospinning chamber (EC-CLI) from IME Technologies. The temperature and relative humidity are set to 25 °C and 30% respectively. The flow rate was 0.55 mL/h (controlled with a HARVARD syringe pump). The tip-to-collector distance was 15 cm, and the voltage was set to 14 kV. The nanofibers were electrospun from a needle with an inner diameter of 0.25 mm and an outer diameter of 0.52 mm. In order to obtain aligned nanofibers, a parallel plate collector was used.[148] The collector consists of two aluminum stripes separated by a void gap of 1 cm wide and 1.5 cm long. The rest of the collector, where deposition of nanofibers is undesired, was covered with teflon. With this type of collector, the electrostatic forces generated by the two conductive stripes induce a uniaxial alignment of the charged spun nanofibers across the insulating gap.[149]

**4. Photoluminescence of the PVP and the E7 liquid crystal**

Figure B1 demonstrates that under UV excitation, both the PVP (in ethanol solution) and the E7 liquid crystal emit in the visible range. Thus, without filtering the collected light their emission would interfere with our experiments. To avoid this spectral filtering, I therefore used green light to selectively excite the CdSe/CdS NRs.

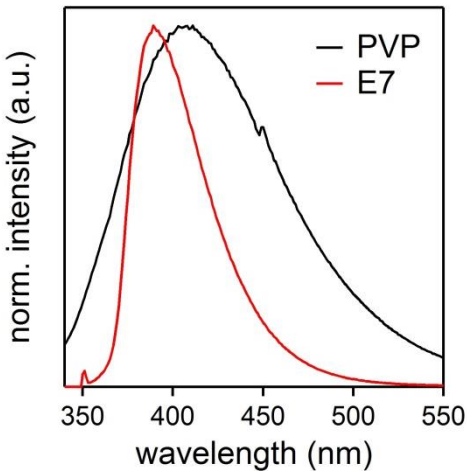


**Figure B.1:** Emission spectra of the PVP (in ethanol solution) and the E7 liquid crystal for excitation wavelengths of 300 nm and 350 nm respectively.

# Bibliography

1. N. J. D. P. Kristiaan, Tassin; Pieter, Van Brabant; Jeroen, Beeckman; Irina, Veretennicoff, *Optical Materials*,122-123 (2013).

2. V. A. Belyakov, "Low threshold DFB lasing at the edge and defect modes in chiral liquid crystals," Molecular Crystals and Liquid Crystals **488**, 279-308 (2008).

3. A. Chanishvili, G. Chilaya, G. Petriashvili, R. Barberi, R. Bartolino, G. Cipparrone, A. Mazzulla, and L. Oriol, "Lasing in dye-doped cholesteric liquid crystals: Two new tuning strategies," Adv. Mater. **16**, 791 (2004).

4. H. Shirvani-Mahdavi, E. Mohajerani, and S. T. Wu, "Circularly polarized high-efficiency cholesteric liquid crystal lasers with a tunable nematic phase retarder," Optics Express **18**, 5021-5027 (2010).

5. A. D. Ford, S. M. Morris, and H. J. Coles, "Phototonics and lasing in liquid crystals," Mater. Today **9**, 36-42 (2006).

6. L. Penninck, J. Beeckman, P. De Visschere, and K. Neyts, "Numerical simulation of stimulated emission and lasing in dye doped cholesteric liquid crystal films," J. Appl. Phys. **113** (2013).

7. Y. Inoue, H. Yoshida, K. Inoue, A. Fujii, and M. Ozaki, "Improved Lasing Threshold of Cholesteric Liquid Crystal Lasers with In-Plane Helix Alignment," Applied Physics Express **3** (2010).

8. M. Mitov, "Cholesteric Liquid Crystals with a Broad Light Reflection Band," Adv. Mater. **24**, 6260-6276 (2012).

9. D. K. Yang, J. L. West, L. C. Chien, and J. W. Doane, "Control of reflectivity and bistability in displays using cholesteric

liquid crystals," J. Appl. Phys. **76**, 1331-1333 (1994).

10. P. G. De Gennes, *The Physics of Liquid Crystals* (Clarendon Press, Oxford, 1974).

11. J. Hwang, M. H. Song, B. Park, S. Nishimura, T. Toyooka, J. W. Wu, Y. Takanishi, K. Ishikawa, and H. Takezoe, "Electro-tunable optical diode based on photonic bandgap liquid-crystal heterojunctions," Nature Materials **4**, 383-387 (2005).

12. B. C. Kim, Y. J. Lim, J. H. Song, J. H. Lee, K.-U. Jeong, J. H. Lee, G.-D. Lee, and S. H. Lee, "Wideband antireflective circular polarizer exhibiting a perfect dark state in organic light-emitting-diode display," Optics Express **22**, A1725-A1730 (2014).

13. G.-F. Tseng, C.-H. Tsai, H. Y. Lin, W.-J. Huang, K.-C. Huang, and K. Lee, "The fabrication of microretarder for in-cell stereoscopic LCD using reactive liquid crystal - art. no. 64900W," in *Stereoscopic Displays and Virtual Reality Systems XIV*, A. J. Woods, N. A. Dodgson, J. O. Merritt, M. T. Bolas, and I. E. McDowall, eds. (2007), pp. W4900-W4900.

14. V. P. Shibaev, "Liquid-Crystalline Polymers: Past, Present, and Future," Polymer Science Series A **51**, 1131-1193 (2009).

15. A. L. Efros, and A. L. Efros, "Interband absorption of light in a semiconductor sphere" Soviet Physics Semiconductors-Ussr **16**, 772-775 (1982).

16. E. R. Smith, J. M. Luther, and J. C. Johnson, "Ultrafast Electronic Delocalization in CdSe/CdS Quantum Rod Heterostructures," Nano letters **11**, 4923-4931 (2011).

17. Gittlema.Ji, B. Abeles, and S. Bozowski, "Superparamagnetism and relaxation effects in granular Ni-SiO2 and Ni-Al2O3 films" Phys. Rev. B **9**, 3891-3897 (1974).

18. J. Cao, T. Sun, and K. T. V. Grattan, "Gold nanorod-based localized surface plasmon resonance biosensors: A review," Sensors and Actuators B-Chemical **195**, 332-351 (2014).

19. S. Link, and M. A. El-Sayed, "Spectral properties and relaxation dynamics of surface plasmon electronic oscillations in gold and silver nanodots and nanorods," Journal of Physical Chemistry B **103**, 8410-8426 (1999).

20. A. Hassinen, "An NMR Study on the Surface Chemistry of Colloidal Quantum Dots, from Ligand Analysis to Optical Properties," (Ghent University. Faculty of Sciences, 2013).

21. L. Brus, "Electronic wave functions in semiconductor clusters: experiment and theory" Journal of Physical Chemistry **90**, 2555-2560 (1986).

22. M. Shim, and H. McDaniel, "Anisotropic nanocrystal heterostructures: Synthesis and lattice strain," Current Opinion in Solid State & Materials Science **14**, 83-94 (2010).

23. Z. Hens, and I. Moreels, "Light absorption by colloidal semiconductor quantum dots," Journal of Materials Chemistry **22**, 10406-10415 (2012).

24. F. Pisanello, L. Martiradonna, P. Spinicelli, A. Fiore, J. P. Hermier, L. Manna, R. Cingolani, E. Giacobino, A. Bramati, M. De Vittorio, and Ieee, *Polarized Single Photon Emission for Quantum Cryptography Based on Colloidal Nanocrystals* (Ieee, New York, 2009).

25. R. Krahne, G. Morello, A. Figuerola, C. George, S. Deka, and L. Manna, "Physical properties of elongated inorganic nanoparticles," Physics Reports-Review Section of Physics Letters **501**, 75-221 (2011).

26. K. Becker, J. M. Lupton, J. Muller, A. L. Rogach, D. V. Talapin, H. Weller, and J. Feldmann, "Electrical control of Forster energy transfer," Nature Materials **5**, 777-781 (2006).

27. W. S. Chang, J. W. Ha, L. S. Slaughter, and S. Link, "Plasmonic nanorod absorbers as orientation sensors," Proceedings of the National Academy of Sciences of the United States of America **107**, 2781-2786 (2010).

28. A. Rizzo, C. Nobile, M. Mazzeo, M. De Giorgi, A. Fiore, L. Carbone, R. Cingolani, L. Manna, and G. Gigli, "Polarized Light Emitting Diode by Long-Range Nanorod Self-Assembling on a Water Surface," Acs Nano **3**, 1506-1512 (2009).

29. M. Fisher, M. Zanella, D. J. Farrell, L. Manna, P. Stavrinou, and A. J. Chatten, "Luminescent Solar Concentrators utilising aligned CdSe/CdS nanorods," 2011 37th IEEE Photovoltaic Specialists Conference (PVSC 2011), 858-863 (2011).

30. C. Nobile, V. A. Fonoberov, S. Kudera, A. Della Torre, A. Ruffino, G. Chilla, T. Kipp, D. Heitmann, L. Manna, R. Cingolani, A. A. Balandin,

and R. Krahne, "Confined optical phonon modes in aligned nanorod arrays detected by resonant inelastic light scattering," Nano letters **7**, 476-479 (2007).

31. F. Liu, J. Wang, Z. Ge, K. Li, H. Ding, B. Zhang, D. Wang, and H. Yang, "Electro-responsive 1-D nanomaterial driven broad-band reflection in chiral nematic liquid crystals," Journal of Materials Chemistry C **1**, 216-219 (2013).

32. A. Persano, M. De Giorgi, A. Fiore, R. Cingolani, L. Manna, A. Cola, and R. Krahne, "Photoconduction Properties in Aligned Assemblies of Colloidal CdSe/CdS Nanorods," Acs Nano **4**, 1646-1652 (2010).

33. A. Sitt, I. Hadar, and U. Banin, "Band-gap engineering, optoelectronic properties and applications of colloidal heterostructured semiconductor nanorods," Nano Today **8**, 494-513 (2013).

34. J. De Smet, A. Avci, P. Joshi, D. Schaubroeck, D. Cuypers, and H. De Smet, "Progress toward a liquid crystal contact lens display," Journal of the Society for Information Display **21**, 399-406 (2013).

35. J. De Smet, A. Avci, R. Beernaert, D. Cuypers, and H. De Smet, "Design and Wrinkling Behavior of a Contact Lens With an Integrated Liquid Crystal Light Modulator," Journal of Display Technology **8**, 299-305 (2012).

36. T. Scharf, "Polarized Light in Liquid Crystals and Polymers " (John Wiley & Sons, Inc, 2007).

37. E. Peeters, J. Lub, J. A. M. Steenbakkers, and D. J. Broer, "High-contrast thin-film polarizers by photo-crosslinking of smectic guest-host systems," Adv. Mater. **18**, 2412 (2006).

38. V. My-Phung, C. C. L. Schuurmans, C. W. M. Bastiaansen, and D. J. Broer, "Polarization-selective polymerization in a photo-crosslinking monomer film," Rsc Advances **4**, 62499-62504 (2014).

39. Y. J. Bae, H. J. Yang, S. H. Shin, K. U. Jeong, and M. H. Lee, "A novel thin film polarizer from photocurable non-aqueous lyotropic chromonic liquid crystal solutions," Journal of Materials Chemistry **21**, 2074-2077 (2011).

40. O. T. Picot, M. Dai, D. J. Broer, T. Peijs, and C. W. M. Bastiaansen, "New Approach toward Reflective Films and Fibers Using Cholesteric Liquid-Crystal Coatings," Acs Applied Materials & Interfaces **5**, 7117-7121 (2013).

41. http://www.thorlabs.de/newgrouppage9.cfm?objectgroup_id=8166, "Liquid Crystal Optical Beam Shutter," (2014).

42. B.-H. Yu, J.-W. Huh, and T.-H. Yoon, "Design of a cholesteric liquid crystal cell for a high-transmittance light shutter," Emerging Liquid Crystal Technologies Ix **9004** (2014).

43. S. Kado, Y. Takeshima, Y. Nakahara, and K. Kimura, "Potassium-ion-selective sensing based on selective reflection of cholesteric liquid crystal membranes," Journal of Inclusion Phenomena and Macrocyclic Chemistry **72**, 227-232 (2012).

44. B. W. Liu, Z. G. Zheng, X. C. Chen, and D. Shen, "Low-voltage-modulated laser based on dye-doped polymer stabilized cholesteric liquid crystal," Opt. Mater. Express **3**, 519-526 (2013).

45. Y. H. Huang, Y. Zhou, C. Doyle, and S. T. Wu, "Tuning the photonic band gap in cholesteric liquid crystals by temperature-dependent dopant solubility," Optics Express **14**, 1236-1242 (2006).

46. K. Funamoto, M. Ozaki, and K. Yoshino, "Discontinuous shift of lasing wavelength with temperature in cholesteric liquid crystal," Japanese Journal of Applied Physics Part 2-Letters **42**, L1523-L1525 (2003).

47. L. V. Natarajan, J. M. Wofford, V. P. Tondiglia, R. L. Sutherland, H. Koerner, R. A. Vaia, and T. J. Bunning, "Electro-thermal tuning in a negative dielectric cholesteric liquid crystal material," J. Appl. Phys. **103** (2008).

48. S. Furumi, and N. Tamaoki, "Glass-Forming Cholesteric Liquid Crystal Oligomers for New Tunable Solid-State Laser," Adv. Mater. **22**, 886-+ (2010).

49. S. Kurihara, Y. Hatae, T. Yoshioka, M. Moritsugu, T. Ogata, and T. Nonaka, "Photo-tuning of lasing from a dye-doped cholesteric liquid crystals by photoisomerization of a sugar derivative having plural azobenzene groups," Appl. Phys. Lett. **88** (2006).

50. G. S. Chilaya, "Light-controlled change in the helical pitch and broadband tunable cholesteric liquid-crystal lasers," Crystallography Reports **51**, S108-S118 (2006).

51. T. J. White, R. L. Bricker, L. V. Natarajan, V. P. Tondiglia, C. Bailey, L. Green, Q. A. Li, and T. J. Bunning, "Electromechanical and light tunable cholesteric liquid crystals," Opt. Commun. **283**, 3434-3436 (2010).

52. H. Finkelmann, S. T. Kim, A. Munoz, P. Palffy-Muhoray, and B. Taheri, "Tunable mirrorless lasing in cholesteric liquid crystalline elastomers," Adv. Mater. **13**, 1069 (2001).

53. H. P. Yu, B. Y. Tang, J. H. Li, and L. Li, "Electrically tunable lasers made from electro-optically active photonics band gap materials," Optics Express **13**, 7243-7249 (2005).

54. Y. Inoue, Y. Matsuhisa, H. Yoshida, R. Ozaki, H. Moritake, A. Fujii, and M. Ozaki, "Electric Field Dependence of Lasing Wavelength in Cholesteric Liquid Crystal with an In-Plane Helix Alignment," Molecular Crystals and Liquid Crystals **516**, 182-189 (2010).

55. H. Yoshida, Y. Inoue, T. Isomura, Y. Matsuhisa, A. Fujii, and M. Ozaki, "Position sensitive, continuous wavelength tunable laser based on photopolymerizable cholesteric liquid crystals with an in-plane helix alignment," Appl. Phys. Lett. **94** (2009).

56. S. S. Choi, S. M. Morris, W. T. S. Huck, and H. J. Coles, "Electrically Tuneable Liquid Crystal Photonic Bandgaps," Adv. Mater. **21**, 3915-+ (2009).

57. S. S. Choi, S. M. Morris, W. T. S. Huck, and H. J. Coles, "Simultaneous red-green-blue reflection and wavelength tuning from an achiral liquid crystal and a polymer template," Adv. Mater. **22**, 53-+ (2010).

58. B. Park, M. Kim, S. W. Kim, W. Jang, H. Takezoe, Y. Kim, E. H. Choi, Y. H. Seo, G. S. Cho, and S. O. Kong, "Electrically Controllable Omnidirectional Laser Emission from a Helical-Polymer Network Composite Film," Adv. Mater. **21**, 771-+ (2009).

59. Y. Inoue, H. Yoshida, K. Inoue, Y. Shiozaki, H. Kubo, A. Fujii, and M. Ozaki, "Tunable Lasing from a Cholesteric Liquid Crystal Film Embedded with a Liquid Crystal Nanopore Network," Adv. Mater. **23**, 5498-+ (2011).

60. J. Schmidtke, G. Junnemann, S. Keuker-Baumann, and H. S. Kitzerow, "Electrical fine tuning of liquid crystal lasers," Appl. Phys. Lett. **101** (2012).

61. C. A. Bailey, V. P. Tondiglia, L. V. Natarajan, M. M. Duning, R. L. Bricker, R. L. Sutherland, T. J. White, M. F. Durstock, and T. J. Bunning, "Electromechanical tuning of cholesteric liquid crystals," J. Appl. Phys. **107**, 13105-13108 (2010).

62. S. S. Choi, S. M. Morris, W. T. S. Huck, and H. J. Coles, "The switching properties of chiral nematic liquid crystals using electrically commanded surfaces," Soft Matter **5**, 354-362 (2009).

63. S. Furumi, S. Yokoyama, A. Otomo, and S. Mashiko, "Control of photonic bandgaps in chiral liquid crystals for distributed feedback effect," Thin Solid Films **499**, 322-328 (2006).

64. M. Kawachi, and O. Kogure, "Hysteresis behavior of texture in the field-induced nematic-cholesteric relaxation" Japanese Journal of Applied Physics **16**, 1673-1678 (1977).

65. F. J. Kahn, "Electric-field-induced color changes and pitch dilation in cholesteric liquid crystals" Phys. Rev. Lett. **24**, 209-& (1970).

66. W. Helfrich, "Electrohydrodynamic and Dielectric Instabilities of Cholesteric Liquid Crystals " J. Chem. Phys. **55**, 839-& (1971).

67. W. Helfrich, "Deformation of cholesteric liquid crystals with low threshold voltage," Appl. Phys. Lett. **17**, 531-532 (1970).

68. T. H. Lin, H. C. Jau, C. H. Chen, Y. J. Chen, T. H. Wei, C. W. Chen, and A. Y. G. Fuh, "Electrically controllable laser based on cholesteric liquid crystal with negative dielectric anisotropy," Appl. Phys. Lett. **88** (2006).

69. R. A. M. Hikmet, and H. Kemperman, "Electrically switchable mirrors and optical components made from liquid-crystal gels," Nature **392**, 476-479 (1998).

70. R. A. M. Hikmet, and H. Kemperman, "Switchable mirrors of chiral liquid crystal gels," Liq. Cryst. **26**, 1645-1653 (1999).

71. A. Bobrovsky, and V. Shibaev, "Novel type of combined photopatternable and electro-switchable polymer-stabilized cholesteric materials," Journal of Materials Chemistry **19**, 366-372 (2009).

72. J. Chen, S. M. Morris, T. D. Wilkinson, and H. J. Coles, "Reversible color switching from blue to red in a polymer stabilized chiral nematic liquid crystals," Appl. Phys. Lett. **91** (2007).

73. M. Mitov, E. Nouvet, and N. Dessaud, "Polymer-stabilized cholesteric liquid crystals as switchable photonic broad bandgaps," Eur Phys J E **15**, 413-419 (2004).

74. K. G. Kang, L. C. Chien, and S. Sprunt, "Polymer-stabilized cholesteric liquid crystal micrograting: a comparison of polymer network

formation and electro-optic properties for mesogenic and non-mesogenic monomers," Liquid Crystals **29**, 9-18 (2002).

75. M. E. McConney, V. P. Tondiglia, L. V. Natarajan, K. M. Lee, T. J. White, and T. J. Bunning, "Electrically Induced Color Changes in Polymer-Stabilized Cholesteric Liquid Crystals," Advanced Optical Materials **1**, 417-421 (2013).

76. S.-Y. Lu, and L.-C. Chien, "A polymer-stabilized single-layer color cholesteric liquid crystal display with anisotropic reflection," Appl. Phys. Lett. **91** (2007).

77. X. Yi, J. Beeckman, W. Woestenborghs, K. Panajotov, and K. Neyts, "VCSEL with photo-aligned liquid crystal overlay," IEEE Photonics Technol. Lett. **24**, 1509-1512 (2012).

78. T. Kihara, "Measurement method of Stokes parameters using a quarter-wave plate with phase difference errors," Applied Optics **50**, 2582-2587 (2011).

79. T. Scharf, "Polarized light in liquid crystals and polymers," (John Wiley & Sons, Inc, 2007).

80. B. Sun, and H. Sirringhaus, "Surface tension and fluid flow driven self-assembly of ordered ZnO nanorod films for high-performance field effect transistors," Journal of the American Chemical Society **128**, 16231-16237 (2006).

81. L. S. Li, and A. P. Alivisatos, "Semiconductor nanorod liquid crystals and their assembly on a substrate," Adv. Mater. **15**, 408 (2003).

82. C. Kuemin, L. Nowack, L. Bozano, N. D. Spencer, and H. Wolf, "Oriented Assembly of Gold Nanorods on the Single-Particle Level," Advanced Functional Materials **22**, 702-708 (2012).

83. D. V. Talapin, E. V. Shevchenko, C. B. Murray, A. Kornowski, S. Forster, and H. Weller, "CdSe and CdSe/CdS nanorod solids," Journal of the American Chemical Society **126**, 12984-12988 (2004).

84. F. Kim, S. Kwan, J. Akana, and P. D. Yang, "Langmuir-Blodgett nanorod assembly," Journal of the American Chemical Society **123**, 4360-4361 (2001).

85. H. Liangtao, L. Liang-Shi, Y. Weidong, L. Manna, W. Lin-Wang, and A. P. Alivisatos, "Linearly polarized emission from colloidal semiconductor quantum rods," Science **292**, 2060-2063 (2001).

86. F. Pisanello, L. Martiradonna, G. Lemeacutenager, P. Spinicelli, A. Fiore, L. Manna, J. P. Hermier, R. Cingolani, E. Giacobino, M. De Vittorio, and A. Bramati, "Room temperature-dipolelike single photon source with a colloidal dot-in-rod," Appl. Phys. Lett. **96**, 033101-033103 (2010).

87. L. Carbone, C. Nobile, M. De Giorgi, F. D. Sala, G. Morello, P. Pompa, M. Hytch, E. Snoeck, A. Fiore, I. R. Franchini, M. Nadasan, A. F. Silvestre, L. Chiodo, S. Kudera, R. Cingolani, R. Krahne, and L. Manna, "Synthesis and micrometer-scale assembly of colloidal CdSe/CdS nanorods prepared by a seeded growth approach," Nano letters **7**, 2942-2950 (2007).

88. A. Singh, R. D. Gunning, S. Ahmed, C. A. Barrett, N. J. English, J. A. Garate, and K. M. Ryan, "Controlled semiconductor nanorod assembly from solution: influence of concentration, charge and solvent nature," Journal of Materials Chemistry **22**, 1562-1569 (2012).

89. C. Querner, M. D. Fischbein, P. A. Heiney, and M. Drndic, "Millimeter-scale assembly of CdSe nanorods into smectic superstructures by solvent drying kinetics," Adv. Mater. **20**, 2308 (2008).

90. A. Ghezelbash, B. Koo, and B. A. Korgel, "Self-assembled stripe patterns of CdS nanorods," Nano Letters **6**, 1832-1836 (2006).

91. M. Zanella, R. Gomes, M. Povia, C. Giannini, Y. Zhang, A. Riskin, M. Van Bael, Z. Hens, and L. Manna, "Self-Assembled Multilayers of Vertically Aligned Semiconductor Nanorods on Device-Scale Areas," Advanced Materials **23**, 2205 (2011).

92. J. L. Baker, A. Widmer-Cooper, M. F. Toney, P. L. Geissler, and A. P. Alivisatos, "Device-Scale Perpendicular Alignment of Colloidal Nanorods," Nano Letters **10**, 195-201 (2010).

93. Y. Amit, A. Faust, I. Lieberman, L. Yedidya, and U. Banin, "Semiconductor nanorod layers aligned through mechanical rubbing," Physica Status Solidi a-Applications and Materials Science **209**, 235-242 (2012).

94. Z. H. Hu, M. D. Fischbein, C. Querner, and M. Drndic, "Electric-field-driven accumulation and alignment of CdSe and CdTe nanorods in nanoscale devices," Nano letters **6**, 2585-2591 (2006).

95. K. M. Ryan, A. Mastroianni, K. A. Stancil, H. T. Liu, and A. P. Alivisatos, "Electric-field-assisted assembly of perpendicularly oriented nanorod superlattices," Nano Letters **6**, 1479-1482 (2006).

96. M. Mohammadimasoudi, L. Penninck, T. Aubert, R. Gomes, Z. Hens, F. Strubbe, and K. Neyts, "Fast and versatile deposition of aligned semiconductor nanorods by dip-coating on a substrate with interdigitated electrodes," Opt Mater Express **3**, 2045-2054 (2013).

97. A. Singh, N. J. English, and K. M. Ryan, "Highly Ordered Nanorod Assemblies Extending over Device Scale Areas and in Controlled Multilayers by Electrophoretic Deposition," Journal of Physical Chemistry B **117**, 1608-1615 (2013).

98. D. Baranov, A. Fiore, M. van Huis, C. Giannini, A. Falqui, U. Lafont, H. Zandbergen, M. Zanella, R. Cingolani, and L. Manna, "Assembly of Colloidal Semiconductor Nanorods in Solution by Depletion Attraction," Nano Letters **10**, 743-749 (2010).

99. N. Zhao, K. Liu, J. Greener, Z. H. Nie, and E. Kumacheva, "Close-Packed Superlattices of Side-by-Side Assembled Au-CdSe Nanorods," Nano Letters **9**, 3077-3081 (2009).

100. A. M. Hung, N. A. Konopliv, and J. N. Cha, "Solvent-Based Assembly of CdSe Nanorods in Solution," Langmuir **27**, 12322-12328 (2011).

101. A. M. Hung, T. Oh, and J. N. Cha, "Facile thermal treatment process for assembling vertically aligned semiconductor nanorods in solution," Nanoscale **4**, 1016-1020 (2012).

102. F. Pietra, F. T. Rabouw, P. G. van Rhee, J. van Rijssel, A. V. Petukhov, B. H. Erné, P. C. M. Christianen, C. de Mello Donegá, and D. Vanmaekelbergh, "Self-Assembled CdSe/CdS Nanorod Sheets Studied in the Bulk Suspension by Magnetic Alignment," Acs Nano **8**, 10486-10495 (2014).

103. L. S. Li, and A. P. Alivisatos, "Origin and scaling of the permanent dipole moment in CdSe nanorods," Physical Review Letters **90**, 097402 (2003).

104. J. S. Kamal, R. Gomes, Z. Hens, M. Karvar, K. Neyts, S. Compernolle, and F. Vanhaecke, "Direct determination of absorption anisotropy in colloidal quantum rods," Physical Review B **85**, 035126 (2012).

105. H. E. Ruda, and A. Shik, "Nanorod dynamics in ac electric fields," Nanotechnology **21** (2010).

106. R. Krishnan, M. A. Hahn, Z. H. Yu, J. Silcox, P. M. Fauchet, and T. D. Krauss, "Polarization surface-charge density of single semiconductor quantum rods," Phys. Rev. Lett. **92** (2004).

107. S. Adachi, *Optical Constants of Crystalline and Amorphous Semiconductors* (Springer US, 1999).

108. L. D. Landau, Lifshitz, Evgenii Mikhailovich, *Electrodynamics of continuous media* (Oxford, 1960).

109. A. Sihvola, "Dielectric polarization and particle shape effects," Journal of Nanomaterials (2007).

110. Y. P. K. W T Coffey, J T Waldron, *The Langevin Equation* (World Scientific Series in Contemporary Chemical Physics, 2004).

111. F. Perrin, "Brownian motion of an anisotropic particle," J. de Phys. et Rad. V (1934).

112. J. S. Kamal, R. Gomes, Z. Hens, M. Karvar, K. Neyts, S. Compernolle, and F. Vanhaecke, "Direct determination of absorption anisotropy in colloidal quantum rods," Phys. Rev. B **85** (2012).

113. M. Cirillo, F. Strubbe, K. Neyts, and Z. Hens, "Thermal Charging of Colloidal Quantum Dots in Apolar Solvents: A Current Transient Analysis," Acs Nano **5**, 1345-1352 (2011).

114. Z. Luo, Y.-W. Cheng, and S.-T. Wu, "Polarization-Preserving Light Guide Plate for a Linearly Polarized Backlight," Journal of Display Technology **10**, 208-214 (2014).

115. E. Jang, S. Jun, H. Jang, J. Llim, B. Kim, and Y. Kim, "White-Light-Emitting Diodes with Quantum Dot Color Converters for Display Backlights," Adv Mater **22**, 3076-3080 (2010).

116. C. Nobile, L. Carbone, A. Fiore, R. Cingolani, L. Manna, and R. Krahne, "Self-assembly of highly fluorescent semiconductor nanorods into large scale smectic liquid crystal structures by coffee stain evaporation dynamics," J. Phys.-Condes. Matter **21** (2009).

117. L.-s. Li, J. Walda, L. Manna, and A. P. Alivisatos, "Semiconductor Nanorod Liquid Crystals," Nano letters **2**, 557-560 (2002).

118. M. Artemyev, B. Möller, and U. Woggon, "Unidirectional Alignment of CdSe Nanorods," Nano letters **3**, 509-512 (2003).

119. B. M. I. van der Zande, G. J. M. Koper, and H. N. W. Lekkerkerker, "Alignment of rod-shaped gold particles by electric fields," Journal of Physical Chemistry B **103**, 5754-5760 (1999).

120. H. E. Ruda, and A. Shik, "Principles of nanowire alignment in an electric field," J. Appl. Phys. **109** (2011).

121. S. Blatt, F. Hennrich, H. von Loehneysen, M. M. Kappes, A. Vijayaraghavan, and R. Krupke, "Influence of structural and dielectric anisotropy on the dielectrophoresis of single-walled carbon nanotubes," Nano letters **7**, 1960-1966 (2007).

122. W. Ahmed, E. S. Kooij, A. van Silfhout, and B. Poelsema, "Quantitative Analysis of Gold Nanorod Alignment after Electric Field-Assisted Deposition," Nano letters **9**, 3786-3794 (2009).

123. O. Harnack, C. Pacholski, H. Weller, A. Yasuda, and J. M. Wessels, "Rectifying Behavior of Electrically Aligned ZnO Nanorods," Nano letters **3**, 1097-1101 (2003).

124. Z. Hu, M. D. Fischbein, C. Querner, and M. Drndic, "Electric-field-driven accumulation and alignment of CdSe and CdTe nanorods in nanoscale devices," Nano letters **6**, 2585-2591 (2006).

125. E. Rossitto, O. Lecarme, L. Latu-Romain, K. Berton, T. Pinedo-Rivera, T. Jiu, P. Reiss, and D. Peyrade, "Influence of optical excitation on the electric field assisted assembly of CdSe nanorods," Microelectron. Eng. **86**, 828-831 (2009).

126. K. M. Ryan, A. Mastroianni, K. A. Stancil, H. Liu, and A. P. Alivisatos, "Electric-Field-Assisted Assembly of Perpendicularly Oriented Nanorod Superlattices," Nano letters **6**, 1479-1482 (2006).

127. S. Gupta, Q. Zhang, T. Emrick, and T. P. Russell, "“Self-Corralling” Nanorods under an Applied Electric Field," Nano letters **6**, 2066-2069 (2006).

128. D. V. Talapin, R. Koeppe, S. Götzinger, A. Kornowski, J. M. Lupton, A. L. Rogach, O. Benson, J. Feldmann, and H. Weller, "Highly Emissive Colloidal CdSe/CdS Heterostructures of Mixed Dimensionality," Nano Lett. **3**, 1677-1681 (2003).

129. F. Pisanello, L. Martiradonna, P. Spinicelli, A. Fiore, J. P. Hermier, L. Manna, R. Cingolani, E. Giacobino, M. De Vittorio, and A. Bramati, "Dots in Rods as Polarized Single Photon Sources," Superlattice. Microst. **47**, 165-169 (2010).

130. I. Hadar, G. B. Hitin, A. Sitt, A. Faust, and U. Banin, "Polarization Properties of Semiconductor Nanorod Heterostructures: From Single Particles to the Ensemble," J. Phys. Chem. Lett. **4**, 502-507 (2013).

131. M. Mohammadimasoudi, L. Penninck, T. Aubert, R. Gomes, Z. Hens, F. Strubbe, and K. Neyts, "Polarized light emission by deposition of aligned semiconductor nanorods," Nanoengineering: Fabrication, Properties, Optics, and Devices Xi **9170** (2014).

132. I. Musevic, M. Skarabot, U. Tkalec, M. Ravnik, and S. Zumer, "Two-dimensional nematic colloidal crystals self-assembled by topological defects," Science **313**, 954-958 (2006).

133. D. C. Christophe Blanc, Emmanuelle Lacaze "Ordering nano- and microparticles assemblies with liquid crystals," Liquid Crystals Reviews **1**, 83-109 (2013).

134. D. Vijayaraghavan, "Self-assembled ordering of single-walled carbon nanotubes in a lyotropic liquid crystal system," Journal of Molecular Liquids **199**, 128-132 (2014).

135. P. S. Kumar, S. K. Pal, S. Kumar, and V. Lakshminarayanan, "Dispersion of thiol stabilized gold nanoparticles in lyotropic liquid crystalline systems," Langmuir **23**, 3445-3449 (2007).

136. Q. Liu, Y. Cui, D. Gardner, X. Li, S. He, and I. I. Smalyukh, "Self-Alignment of Plasmonic Gold Nanorods in Reconfigurable Anisotropic Fluids for Tunable Bulk Metamaterial Applications," Nano letters **10**, 1347-1353 (2010).

137. S. Zhang, G. Leem, L.-O. Srisombat, and T. R. Lee, "Rationally designed ligands that inhibit the aggregation of large gold nanoparticles in solution," Journal of the American Chemical Society **130**, 113-120 (2008).

138. M. Mohammadimasoudi, Z. Hens, and K. Neyts, "Full alignment of colloidal nanorods in solution using alternating electric fields " (2014).

139. L. Carbone, C. Nobile, M. De Giorgi, F. D. Sala, G. Morello, P. Pompa, M. Hytch, E. Snoeck, A. Fiore, I. R. Franchini, M. Nadasan, A. F. Silvestre, L. Chiodo, S. Kudera, R. Cingolani, R. Krahne, and L. Manna, "Synthesis and Micrometer-Scale Assembly of Colloidal CdSe/CdS Nanorods Prepared by a Seeded Growth Approach," Nano Lett. **7**, 2942-2950 (2007).

140. Y. Amit, A. Faust, I. Lieberman, L. Yedidya, and U. Banin, "Semiconductor Nanorod Layers Aligned Through Mechanical Rubbing," Phys. Status Solidi A **209**, 235-242 (2012).

141. A. Lutich, L. Carbone, S. Volchek, V. Yakovtseva, V. Sokol, L. Manna, and S. Gaponenko, "Macroscale Alignment of CdSe/CdS Nanorods by Porous Anodic Alumina Templates," Phys. Status Solidi RRL **3**, 151-153 (2009).

142. P. Yeh, and C. Gu, *Optics of Liquid Crystal Displays* (Wiley Publishing, 2009).

143. J. Jasieniak, L. Smith, J. v. Embden, P. Mulvaney, and M. Califano, "Re-examination of the Size-Dependent Absorption Properties of CdSe Quantum Dots," J. Phys. Chem. C **113**, 19468-19474 (2009).

144. R. Gomes, A. Hassinen, A. Szczygiel, Q. Zhao, A. Vantomme, J. C. Martins, and Z. Hens, "Binding of Phosphonic Acids to CdSe Quantum Dots: A Solution NMR Study," J. Phys. Chem. Lett. **2**, 145-152 (2011).

145. B. De Geyter, and Z. Hens, "The Absorption Coefficient of PbSe/CdSe Core/Shell Colloidal Quantum Dots," Appl. Phys. Lett. **97**, 161908 (2010).

146. F. Pietra, R. J. A. van Dijk-Moes, X. Ke, S. Bals, G. Van Tendeloo, C. de Mello Donega, and D. Vanmaekelbergh, "Synthesis of Highly Luminescent Silica-Coated CdSe/CdS Nanorods," Chem. Mater. **25**, 3427-3434 (2013).

147. L. Palangetic, N. K. Reddy, S. Srinivasan, R. E. Cohen, G. H. McKinley, and C. Clasen, "Dispersity and spinnability: Why highly polydisperse polymer solutions are desirable for electrospinning," Polymer **55**, 4920-4931 (2014).

148. N. K. Reddy, L. Palangetic, L. Stappers, J. Buitenhuis, J. Fransaer, and C. Clasen, "Metallic and bi-metallic Janus nanofibers: electrical and self-propulsion properties," J. Mater. Chem. C **1**, 3646-3650 (2013).

149. D. Li, Y. Wang, and Y. Xia, "Electrospinning Nanofibers as Uniaxially Aligned Arrays and Layer-by-Layer Stacked Films," Adv. Mater. **16**, 361-366 (2004).

---

"Verily knowledge is the life of the hearts, the light of the eyes from blindness and the strength of the bodies against weakness"

Ali ibn Abitaleb